2021

# Nanoscale Spatial Realization of Grain Boundary Defects And its Passivation In Perovskite Solar Cells

Ashraful Haider Chowdhury
*South Dakota State University*

# NANOSCALE SPATIAL REALIZATION OF GRAIN BOUNDARY DEFECTS AND ITS PASSIVATION IN PEROVSKITE SOLAR CELLS

BY

ASHRAFUL HAIDER CHOWDHURY

A dissertation submitted in partial fulfillment of the requirements for the

Doctor of Philosophy

Major in Electrical Engineering

South Dakota State University

2021

DISSERTATION ACCEPTANCE PAGE

Ashraful Haider Chowdhury

This dissertation is approved as a creditable and independent investigation by a candidate for the Doctor of Philosophy degree and is acceptable for meeting the dissertation requirements for this degree. Acceptance of this does not imply that the conclusions reached by the candidate are necessarily the conclusions of the major department.

Qiquan Qiao
Advisor Date

Sid Suryanarayanan
Department Head Date

Nicole Lounsbery, PhD
Director, Graduate School Date

# ACKNOWLEDGEMENTS

The work presented in this dissertation was supported by grants from the NSF MRI (grant no. 1428992), NASA EPSCoR (grants NNX13AD31A and NNX15AM83A), and the U.S. - Egypt Science and Technology Joint Fund EE Ph.D. program by the State of South Dakota.

I would like to express my gratitude to Dr. Qiquan Qiao for providing the opportunity to work as a graduate research assistant in the Center for Advanced Photovoltaics at South Dakota State University. Dr. Qiao's advice has been vital throughout the course of my research work and in improving the technical quality of this dissertation. I would also like to thank my thesis committee members Dr. Yue Zhou, Dr. Robert McTaggart, Dr. Huitian Lu and Dr. Febina Mathew for their time and consideration in reviewing this dissertation. Special thanks to all my group members specially Reza, Ifat, Behzad and Ashim for helping me with solar cell fabrication and characterization as well as their support during my research work at SDSU.

Finally, I would like to thank my family members in particular elder sister Taheti Akhter and friends for their love, support, motivation, and continuous encouragement. Lastly, my wife Amreen Chowdhury who supported me throughout the important phase of the entire journey.

CONTENTS

# ABBREVIATIONS

| | |
|---|---|
| AFM | atomic force microscopy |
| CAFM | conductive atomic force microscopy |
| KPFM | kelvin probe force microscopy |
| LT-AFM | light induced transient atomic force microscopy |
| SP | surface potential |
| PHI | phenylhydrazinium iodide |
| XRD | x-ray diffraction |
| SEM | scanning electron microscopy |
| PL | photoluminescence |
| UV-Vis | UV visible spectroscopy |
| EQE | external quantum efficiency |
| GB | grain boundary |
| FAMACs | $Cs_5(MA_{0.17}FA_{0.83})_{95}Pb(I_{0.83}Br_{0.17})_3$ |
| PCE | power conversion efficiency |
| FF | fill factor |
| $V_{oc}$ | open circuit voltage |
| $J_{sc}$ | short circuit current density |
| PSC | perovskite solar cell |
| PV | photovoltaic |

# LIST OF FIGURES

# LIST OF TABLES

# ABSTRACT

## NANOSCALE SPATIAL REALIZATION OF GRAIN BOUNDARY DEFECTS AND ITS PASSIVATION IN PEROVSKITE SOLAR CELLS

ASHRAFUL HAIDER CHOWDHURY

2021

Perovskite solar cells (PSCs) have seen significant improvement in photovoltaic performance in recent days. However, the performance of PSCs is limited by the defects present at grain boundaries (GB). The study adapted here discusses the nanoscale spatial realization of grain boundary defects and its passivation in perovskite solar cells. Conventional $MAPbI_3$ and state- of-the-art $Cs_5(MA_{0.17}FA_{0.83})_{95}Pb(I_{0.83}Br_{0.17})_3$-FAMACs perovskite GBs were studied in detail using atomic force microscopy. The density of trap states calculation by kelvin probe force microscopy (KPFM) shows that FAMACs perovskites have lower defects at GB compared with $MAPbI_3$ perovskites. This improvement is caused by the less activation energy of the point defects in FAMACs due to mixing of cations and anions in perovskite structure compared with $MAPbI_3$ perovskites. FAMACs perovskite GBs are less dominated by the defect ion migration evident from the negligible local dark-current hysteresis at GBs. To further passivate defects at the GB, FAMACs perovskite was post-treated by using an organic halide salt named phenylhydrazinium iodide (PHI). Defects analysis and passivation at GB of FAMACs perovskite were evaluated using atomic force microscopy technique through mapping of carrier recombination lifetime ($\tau_r$), transport time ($\tau_t$) and diffusion length ($L_D$). These spatially resolved charge carrier dynamics parameters reveal substantial variations at GB of control and passivated perovskites. Defects analysis and passivation at GB of FAMACs

perovskite through charge carrier dynamics nanoscale mapping, KPFM and CAFM demonstrate that optimized concentration of PHI can passivates the positively charged defects and significantly improves charge carrier dynamics at GB compared to control sample. This improvement in nanoscale charge transport in passivated FAMACs gives a PCE of ~20% whereas $MAPbI_3$ and non-passivated FAMACs perovskites show ~17% and ~ 18% PCE, respectively. This clearly indicates that GB passivation in FAMACs reduces the positively charged defects and gives champion PCE of ~20%.

# Chapter 1 Introduction

## 1.1 Background

Fossil fuels are one of the primary sources of the energy that is generated throughout world and hold the promise to be the next source of energy. As the demand for the energy is increasing day by day so the demand for fossil fuels is increasing at the same rate which is going to affect our livelihood due to its detrimental effect. Among many damaging effects, the most important are unusable, high risk to environment, global warming, carbon emission, and pollution. On the other hand, due to high demands of using the fossil fuels, it is expected that fossil fuels will be near to its end very soon. This adverse effects and assumptions related to the end of fossil fuels have motivated researchers across the globe to find alternate sources of energy which can be reusable, low risk to environment, less global warming, and pollution free. Also, the energy source that can last long and serve the humanity are the main objectives for the researchers in present days. Some potential renewable energy sources are wind, hydro, biomass, geothermal, and solar. Nevertheless, solar became the promising source of energy due to its cleanliness, sustainability, cost effective over others such as wind, hydro, biomass and geothermal which are yet to be effective in terms of energy usage. Therefore, the environmentally friendly and inexpensive solar energy have become the primary object of research among the scientific community and industries. Solar energy to electric power is the most effective way of utilizing the solar renewable energy that creates the pathway for Photovoltaics (PV)/ Solar cell technology. Figure 1.1 shows the global electricity generation by source from 2000 to 2050. The advantages of photovoltaics over conventional fossil fuels are reusable, low risk to environment, less global warming, pollution free, and low maintenance cost.

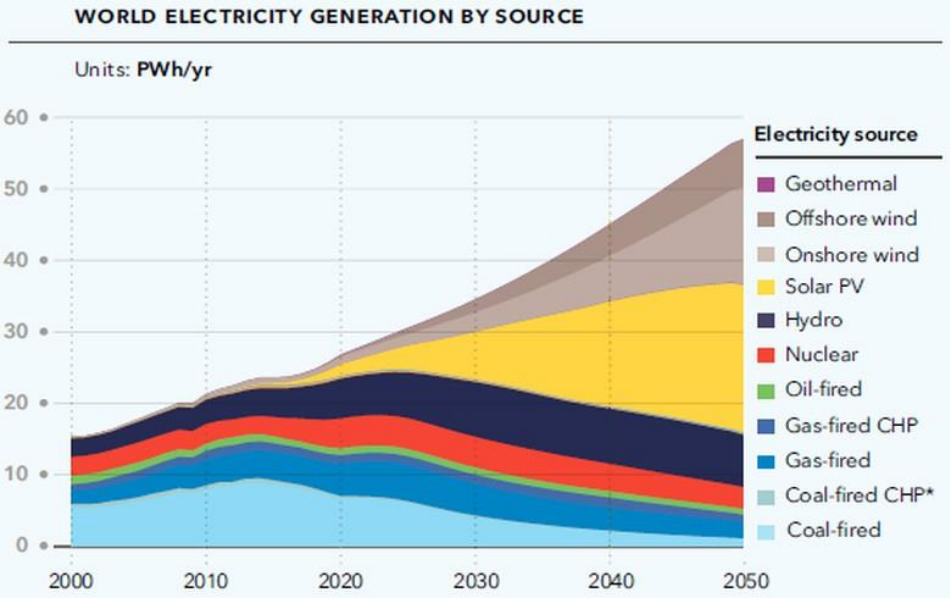


Figure 1.1 Global electricity generation by source from 2000 to 2050 [1].

Till now PV technology has seen three generations. First generation of the solar cells are mainly dominated by the crystalline silicon as the photovoltaic material. At present solar cells made of crystalline silicon materials leads the commercial market of solar cells which have a stable power conversion efficiency (PCE) of ~20% [2]. Then comes the second generation of solar cells having gallium arsenide (GaAs), cadmium telluride (CdTe), copper indium selenide (CIS) and copper indium gallium (di) selenide (CIGS) etc. as the photovoltaic material; an alternate to silicon PV. These materials also showed promising output in terms of PCE, stability and performance. However, both PV generation materials are limited be several key factors such as cost of fabrication, scarcity, complex fabrication processes and most importantly waste disposal. These limitations led the researchers to think of new kind of solar cells with cheap fabrication cost, abundance in nature, easy fabrication process and simple waste disposal which bring the third generation of solar cells. Third generation solar cells are made of cheap materials such as dye, polymers, and perovskites as the PV material. Recent days solar cells like dye-sensitized solar cell

(DSSC), polymer solar cell and Perovskite solar cells (PSCs) have gained substantial attention from the scientists, researchers, and industries because of their numerous advantages over other two generation of solar cells. Unfortunately, DSSC and polymer solar cells are far behind the first and second generation of solar cells which are made of silicon, GaAs, CIGS, and CdTe in terms of PCE, stability and performance. But one candidate from third generation of solar cells has surpassed the first and second generation of solar cells in terms of PCE, stability and performance which is the organic inorganic hybrid material known as perovskites. Figure 1.2 shows the developments in reported PCE for each generation of solar cells till date.

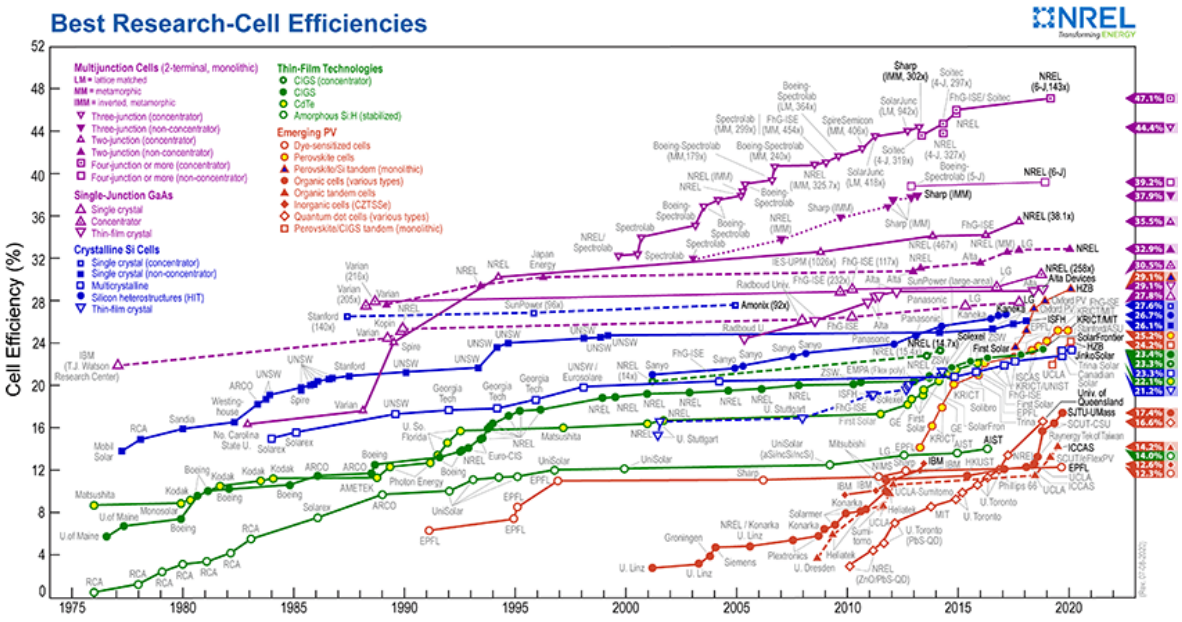


Figure 1.2 PCE evolution of first, second and third generation of solar cells from 1976 to present [3].

Figure 1.3 shows the market share of PV panels by technology type including silicon, thin film and third generation photovoltaics (2014–2030).

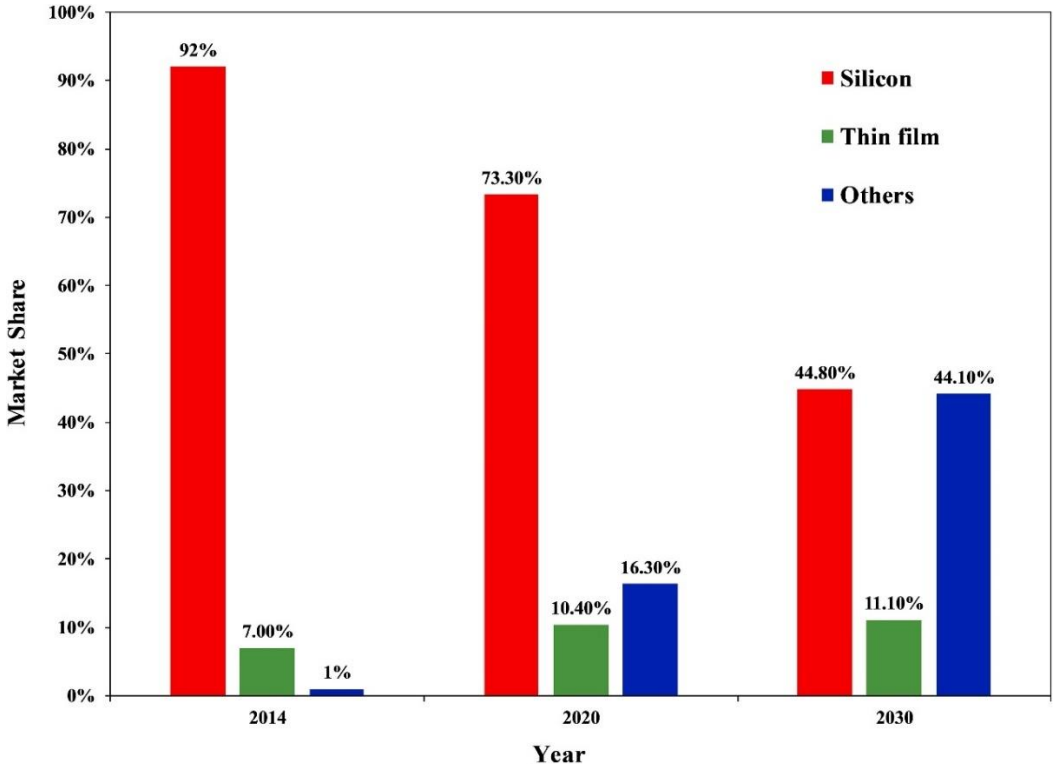


Figure 1.3 Market share of PV panels by technology type (2014–2030) [4]. Here others mean the 3rd generation PV (DSSC, organic and perovskites).

Perovskite solar cells (PSCs) have seen a significant increase in the power conversion efficiency (PCE) from 3.8% to more than 25% mainly due to the film compositional and perovskite/transport layer interfacial engineering [3, 5-7]. As a result, commercialization of the perovskite photovoltaics is currently being pursued either as single-junction or tandem structures with silicon photovoltaics [8]. Figure 1.4 shows the solar cell efficiency records for leading PV technologies until 2019. The early studied methyl ammonium lead iodide ($MAPbI_3$) perovskites have disadvantages such as low power conversion efficiency and poor stability. One key approach has been the use of mixed cations [alloying cesium (Cs), formamidinium (FA) and methylammonium (MA)] and halides to helped to achieve perovskites with higher power conversion efficiency and better stability [9].

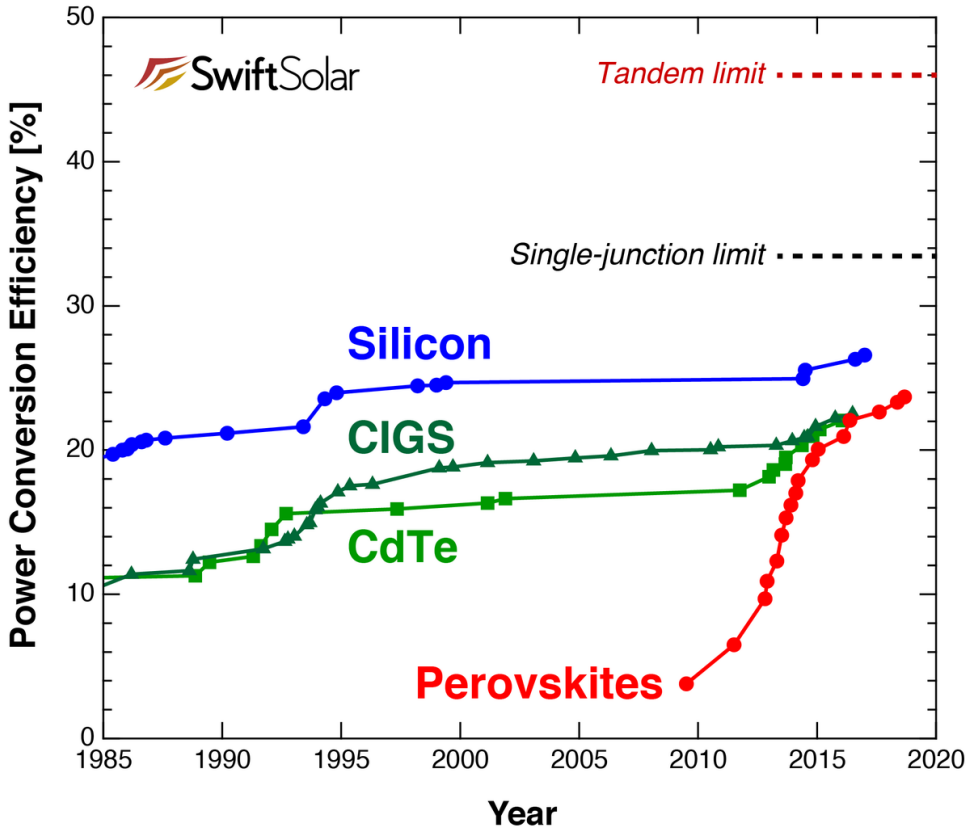


Figure 1.4 Solar cell efficiency records for leading PV technologies until 2019 [10].

However, perovskite films are usually polycrystalline in nature due to solution-processing that creates considerable structural defects, such as grain boundary (GB) and crystallographic defects [11]. Processing conditions and incompatibility of the components in perovskite thin films lead to variation in defects, crystallization and orientation of the film [12, 13]. Therefore, local properties of perovskite films that govern the solar cell performance are likely to vary that cannot be identified at micro scale characterization. For the last few years numerous investigations have been carried out to study the charge carrier dynamics by employing techniques from optical spectroscopy to electrical measurement. Still there exists lack of experimental studies in realizing the fundamental local properties of perovskites at the nanoscale. Hence tools needed to be developed that can quantify local

charge transport parameters. It is vital to address the possible ways to suppress the GB defects in solution-processed perovskite films to further increase PCE towards its thermodynamic limits. Several inherent characteristics of perovskites that include current-voltage hysteresis [14], ion migration [15], trap assisted recombination [16], as well as the material stability in ambient environment [17] arise from defects in GB. Much attention has been paid in recent days to fully realize an efficient charge carrier behavior and suppress the defects in perovskites GB.

## 1.2 Previous Work

Carrier recombination lifetime in bulk of perovskite material is measured by conventional photoluminescence (PL) method to obtain decay lifetimes [18, 19]. However, PL measurement can only do local carrier life time mapping with low spatial resolution [20, 21], not the local carrier transport time and diffusion length. Quilettes and co-workers spatially resolved the PL decay dynamics in 100 nm resolution for nonstoichiometric organic-inorganic perovskites, $CH_3NH_3PbI_3$ (Cl) by using confocal fluorescence microscopy associated with scanning electron microscopy [20]. They revealed that PL intensities are weaker in Grain boundaries (GBs) than non-GB regions suggesting that GBs act as the recombination centers which is consistent with recently reported literature [22, 23]. Yang et al. used high-resolution confocal fluorescence-lifetime imaging microscopy to probe 20 μm × 20 μm perovskite in ~40nm resolution with respect to the carrier lifetime at the regions of interest [21]. They demonstrated GBs have lower luminescence intensities than grains but lifetimes at GBs are not worse compared to single grain region that makes GBs less associated with dominant non-radiative recombination. Also, many reports have claimed that the low performance of the perovskite solar cell arises from the incomplete

coverage of the perovskite film mostly termed voids [24, 25]. Solution processed thin films have the tendency to grow void areas which can act as electron-hole recombination centers resulting in low-resistance shunting paths and absorption loss in solar cells [25]. Conductive atomic force microscopy (CAFM) is the well suited tool that can probe the micro- and nano-scale features of perovskite materials [26]. Analysis of C-AFM images and curves gives insight of charge transport dynamics and quantitative performance parameters for instance charge carrier mobility. Space charge limited current (SCLC) method is extensively used to measure the charge carrier mobility in organic and perovskite materials. The capability of C-AFM to obtain local current-voltage curves at SCLC regime makes it possible to visualize local charge carrier mobility in polymers [27, 28]. But the local out-of-plane mobility values obtained are often larger than device scale SCLC measurements by an order of magnitude [29]. Ginger et al. resolved this inconsistencies by modifying the SCLC equations by finite element simulations and introduces a new parameter i.e. diameter of probe-sample contact [30]. They measured the out-of-plane nano-scale hole mobility of conjugated polymer in accordance with device scale SCLC measurements. Wood and co-workers mapped the temperature dependent local mobility of P3HT polymer with moderate spatial resolution using modified SCLC equations [31]. Though they claimed that results were consistent with grain boundary (GB) limited transport models, no clear relation was established between structural features and carrier mobility. Since precise estimation of probe-sample contact diameter in local SCLC fitting is required, there are various models reported in literature like- Johnson-Kendall-Roberts (JKR), Derjaguin-Muller-Toporov (DMT) and Hertz model [32]. Each model has its own parameters depending the type of sample, deformation, AFM tip size and adhesion.

However there remains discrepancies in approximating the exact value of probe-sample contact diameter which might lead to erroneous estimation in mobility values. Later Button et al. demonstrated that measured charge carrier mobility for organic semiconductor is weakly dependent on probe-sample contact diameter and introduced the role of built in potential in modified SCLC model [33]. Minimum feature size was taken into account to estimate the probe-sample contact diameter rather than using DMT and JKR model. Even so question remains whether modifying SCLC equations would be a good option to correctly estimate the local charge carrier mobility. Recently another study has been reported where local mobility of graphene was measured combining both C-AFM and Kelvin probe force microscopy (KPFM) [34]. Mapping was unlikely as C-AFM and KPFM cannot operate simultaneously. Hence the measurement was confined to a single point mobility. In device scale there are few reports for perovskite mobility measurement by SCLC method. However it is worth mentioning that SCLC mobility is limited to single perovskite crystals with intrinsic charge densities less than $10^{14}$ $cm^{-3}$ [35]. Besides large perovskite crystals are not suitable for practical device applications. Thus, it is crucial to gain insights into the quality of the perovskite film from the direct nanoscale mapping of charge carrier dynamics to achieve higher efficiency. To accomplish this, transient measurement is required to spatially reveal the exact role of these regions including grains, GBs, and voids at the nanoscale regime, which will help, determine film quality and insights into the use of experimental conditions for perovskite solar cell fabrication. Currently, there is no existing equipment or capabilities that can achieve the nanoscale mapping of local transient decay dynamics of carrier lifetime and transport time spatially at nanometer range in any type of solar cells including perovskite solar cells. Several

surface and bulk passivation methods have been adopted to ease the defects that mainly present in perovskite GB. For example, phenethylammonium iodide (PEAI) salt layer on the surface of perovskite can suppress charge recombination and increase the open circuit voltage ($V_{oc}$) significantly [6]. Fluorocarbon based bifunctional molecules have demonstrated to decrease the GB defects both in surface and bulk of the perovskite by a co-passivation strategy [36]. I-type band alignment formed at the perovskite GB by excess $PbI_2$ in the perovskite layer can efficiently suppress the charge recombination [37]. More recently several passivation agents such as guanidinium cation[38], potassium halide [39], phenethylammonium cation[40] have been added into the perovskite precursor solution to passivate GB defects which leads to enhanced device performance. Although these studies have shown that GB passivation largely improved the PCE of PSCs, none of these studies were able to demonstrate the effects of the GB passivation effects at nanoscale. Especially, it is necessary to probe the charge carrier dynamics (such as lifetime, transport time and diffusion length) at nanoscale to further illustrate and understand the core effects of these passivation approaches. Conductive AFM (C-AFM) and Kelvin probe force microscopy (KPFM) are two widely used AFM techniques to study the GB passivation effects at nanoscale[41]. Results obtained from these two methods only provide information on whether GB passivates or not[41]. However, detail assessment on how the GB passivation affects the charge carrier behavior to improve the device performance is unlikely. There has been several tools/methods such as photoluminescence[20, 42], microwave impedance [17], microscopic means[43, 44], conductive AFM [26, 45-47], synchrotron infrared nanospectroscopy [48] to characterize local properties at GB. Nevertheless, these techniques are quite limited with either single charge carrier dynamics measurement

(carrier lifetime) or reveal about the inherent properties of the perovskite such as hysteresis[46], ion migration[46], nanoscale photovoltaic performance[26], local composition at grains[48]. Though some experimental studies have shown that GBs in $MAPbI_3$ perovskites act benignly by favoring charge transport [49, 50], many studies report the adverse effects that GBs can have on the perovskite performance. Further presence of local heterogeneities at GBs requires spatially resolved measurements to fully understand its impacts on device performance. Photoluminescence (PL) studies have spatially resolved the carrier decay dynamics showing weak PL intensities in GBs indicating shorter carrier lifetime in GBs. This further suggests that GBs act as the recombination centers [20, 42]. Microwave impedance microscopy is another nanoscale tool that gives insight to spatial variation at grains and GBs in perovskites by measuring local photoconductivity[17]. Home-built microscopes were used to spatially resolve lifetime, photocurrent and trap density maps to conclude dominant intrinsic electron traps in single and mixed cation perovskites, however, no correlation to microstructural features (Grain, GBs) was studied [43, 44]. No experimental studies exist that can measure charge carrier dynamics (lifetime, transport time and diffusion length) in perovskites at nanoscale that can reveal insights about the GB passivation.

## 1.3 Motivation

There is a need to the realize the grain boundary defects and its passivation in perovskite solar cells at the nanoscale to enable better understanding of the material morphology which will lead to the development of high-performance photovoltaic materials.

## 1.4 Objectives

The objective of this work is to better understand the effect of grain boundary and its passivation at nanoscale for improving the power conversion efficiency of perovskite solar cells. To accomplish this objective, following tasks are performed- (1) Atomic force microscopy based defect study at the GB of perovskite material and (2) Detail analysis through carrier dynamics, surface potential and conductive AFM mappings to fully understand the grain boundary passivation effect at nanoscale on the device performance of the perovskite solar cells.

## 1.5 Thesis Overview

Chapter 1 discusses the background, motivation, objectives of this work and previous work related to perovskite studies at nanoscale.

Chapter 2 discusses the perovskite solar cells and its challenges to high power conversion efficiency.

Chapter 3 discusses the tools, methods and materials adapted in this study to study perovskites solar cells at nano and micro scale range.

Chapter 3 discusses the tools, methods and materials adapted in this study to investiagte perovskites solar cells at nano and micro scale range.

Chapter 4 discusses the nanoscale spatial realization of grain boundary defects and its passivation in perovskite solar cells.

Chapter 5 discusses the conclusions and future scope of the work adapted in this study.

# Chapter 2 Perovskite Solar Cells and Its Challenges

## 2.1 Perovskite Solar Cells

Perovskite materials have the crystal structure $ABX_3$ where A and B are cations and X is an anion of different ionic radii. This material was named following its inventor L.A. Perovski who happened to invent it back in 1856. It has many excellent properties including semiconducting and conducting nature. The Crystal structure of perovskites is shown in Fig. 2.1. Most used perovskite for solar cell applications is methyl ammonium lead iodide ($MAPbI_3$) perovskites where A=MA ($CH_3NH_3^+$), B=$Pb^{2+}$ and X=halogen ($I^-$). With the passage of time, researchers have experimented different other materials for the perovskite formation such as A=$FA^+$, $Cs^+$; B=$Sn^{2+}$ and X=$Cl^-$, $Br^-$ either alone or with the combination of two, three or more ($Cs_5(MA_{0.17}FA_{0.83})_{95}Pb(I_{0.83}Br_{0.17})_3$) to increase the performance of the perovskites in solar cell applications.

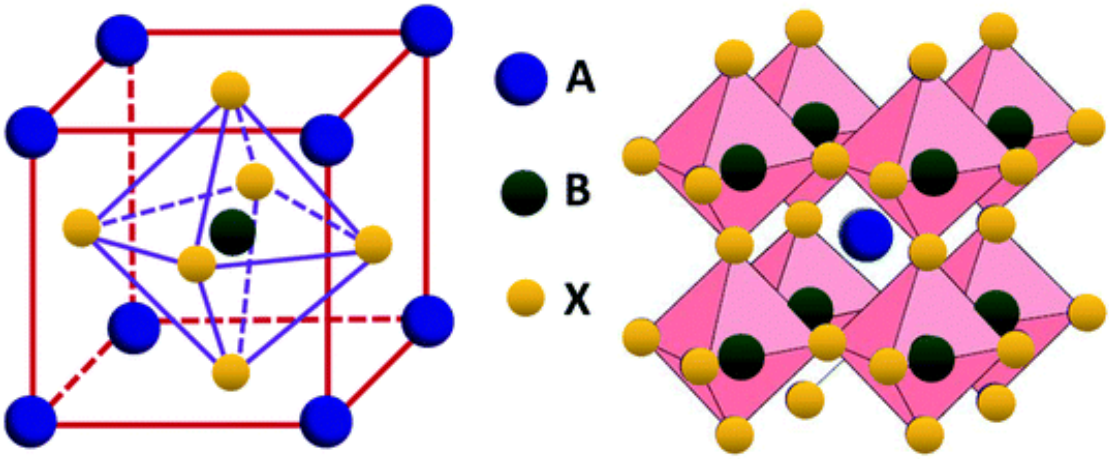


Figure 2.1 Structure of $ABX_3$ perovskite structure. [51]

Perovskite solar cells commonly have two type device structure known as “n-i-p” or an inverted “p-i-n” structure, as shown in Fig. 2.2(a) and (b), respectively. It depends on the

direction of the sunlight and named accordingly either n-i-p or p-i-n. If sunlight goes through the electrode and faces electron transport layer (PCBM/$SNO_2$) then it is the n-i-p structure. Oppositely, if sunlight goes through the electrode and faces hole transport layer (PEDOT: PSS) then it is the p-i-n or the inverted structure.

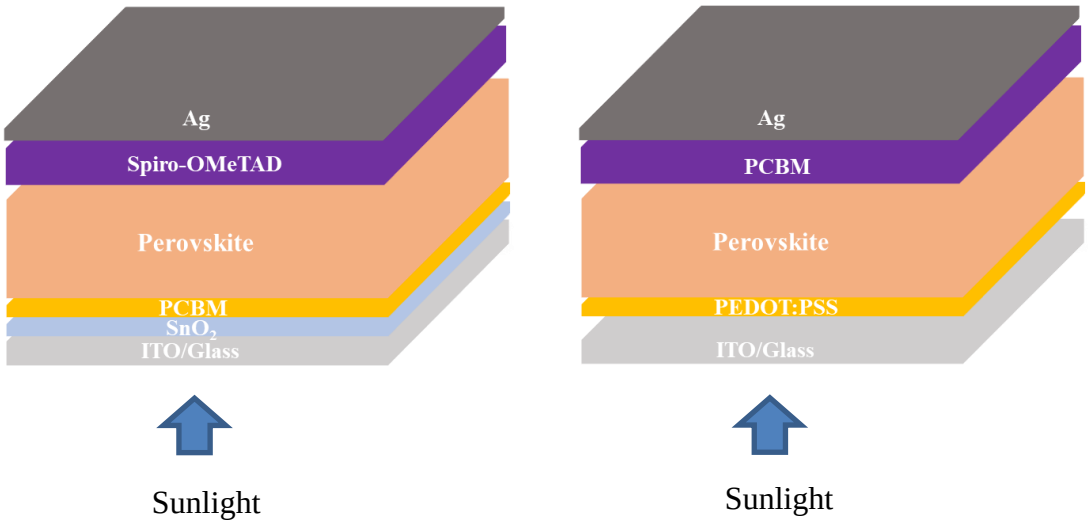


Figure 2.2 Device structure of perovskite solar cells (a) n-i-p and (b) p-i-n.

Inverted devices (p-i-n type) have shown potential in overcoming limitations of the conventional design, however the PCE of the former one is still lower than the later. The energy band diagram of a typical n-i-p perovskite solar cell shows that when the sunlight is absorbed electron-hole pairs are generated. Then those electron hole pairs are separated at the interface where electrons are being moved and holes are blocked by ETL. Similarly, holes are being moved and electrons are blocked by HTL (Figure 2.3). Eventually the flow of electrons and holes create electricity in an external circuit. Thus it uses the perovskite as the absorber material to absorb light and generate electricity in the outside circuit through the separation of electron and hole pair.

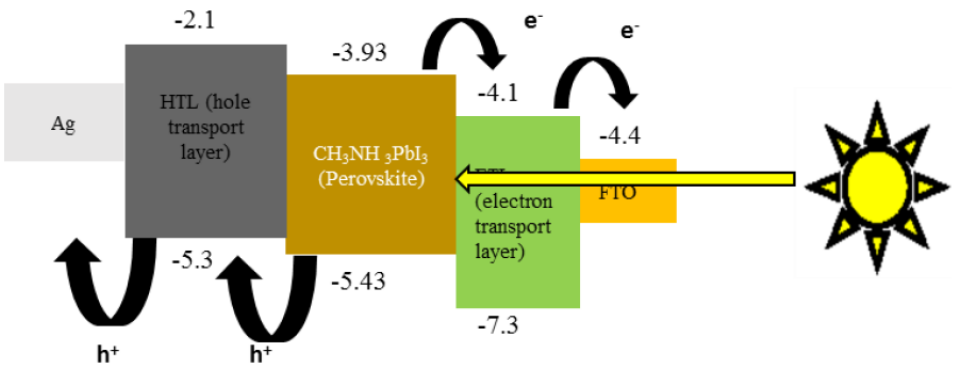


Figure 2.3 Energy band diagram of a typical n-i-p perovskite solar cell and charge carrier flow direction [52].

## 2.2 Challenges in Perovskite Solar Cells

In recent times perovskite solar cells have seen enormous success in terms of power conversion efficiency near to its counterpart silicon photovoltaics. However, there are several challenges are present towards its path for commercialization. Several key challenges are environmental stability, toxicity, and internal instabilities etc. Among all the challenges, the important one which need to be addressed is related to its stability including environmental and internal structure. Perovskites material instability arises from several key phenomenon including defect ion migration [15] and trap assisted recombination [16]. These issues result in current-voltage hysteresis [14], , as well as the material stability in ambient environment [17]. More in-depth research into these challenges put forward a key term known as the grain boundary. Figure 2.4 shows the atomic force microscopy image of a polycrystalline perovskite material showing grains and associated grain boundaries. These GB defects are largely responsible for electron hole recombination at the perovskite solar cells.

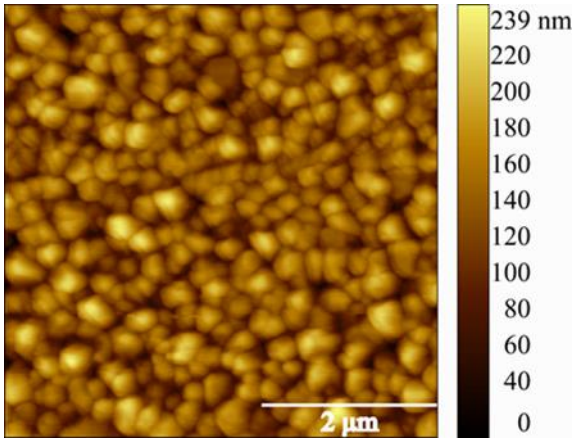


Figure 2.4 Atomic force microscopy image of a polycrystalline perovskite material showing grains and associated grain boundaries.

As perovskites are polycrystalline materials, the processing and manufacturing conditions are responsible for creating the grain boundaries between two perovskite crystalline structures. There are several defects in perovskites which are happened to be concentrated at near and/or grain boundaries.

### 2.2.1 Point Defects in Perovskites

There are basically three types of point defects are present in any crystalline materials such as interstitials, vacancies, and anti-site defects. Figure 2.5 shows the different types of point defects in a crystalline material. The point defect so called vacancies are unoccupied sites in which an atom would be present in a perfect crystal lattice structure. Anti-sites are the point defects which usually replace the original atom and sit in its place where it is not supposed to be present. On the other hand, interstitials are the point defects which usually sit in a place where it is not supposed to be present and takes up an extra place which is not included in the lattice structure. Thus, these cause the point defects in the perovskite materials.

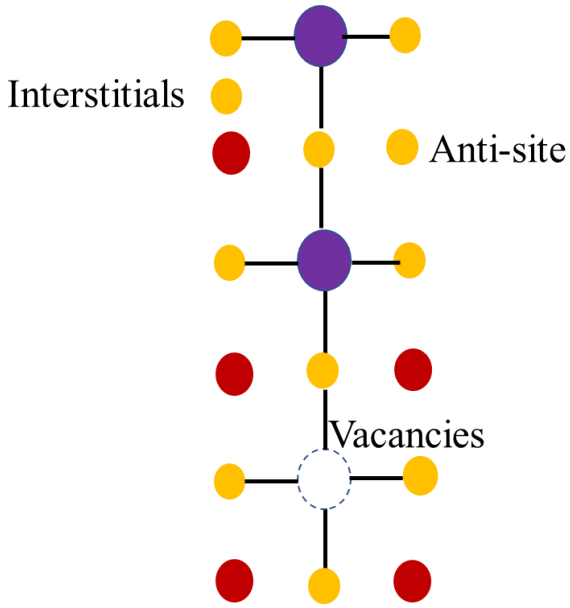


Figure 2.5 Different types of point defects in a crystalline material.

Energy is required to form and migrate the point defects which is known as the defect formation and migration energy, respectively. Usually, the point defects are linked to energy level that defines the energy the charge carrier that sits in that defect. The defect energy levels which are near to conduction band minimum and valence band maximum are termed as the shallow defect energy levels. Whereas the defect energy levels which are far away from conduction band minimum and valence band maximum are termed as the deep defect energy levels. These shallow and deep trap levels form the sites where charge carrier recombines and eventually lost by recombination. In perovskites, the point defects are mobile and migrate throughout the lattice which makes perovskites very much vulnerable to recombination and thus poor device performance. $V_A$ represents vacancies, $A_i$ presents interstitial and $A_B$ and $B_A$ are the anti-sites for perovskite with atom A and B, respectively. Yin et.al. performed theoretical calculations of the point defects formation energy of in $CH_3NH_3PbI_3$ perovskite material (Figure 2.6) and identified types of defects that are can

be present in a perovskite structure [53]. These defects in $MAPbI_3$ perovskites are charged either positively ($MA_i$, $Pb_{MA}$, $V_I$, $Pb_i$, $MA_I$, $Pb_I$) or negatively ($V_{MA}$, $V_{Pb}$, $I_{MA}$, $I_{Pb}$, $I_i$) depending on the respective energy levels.

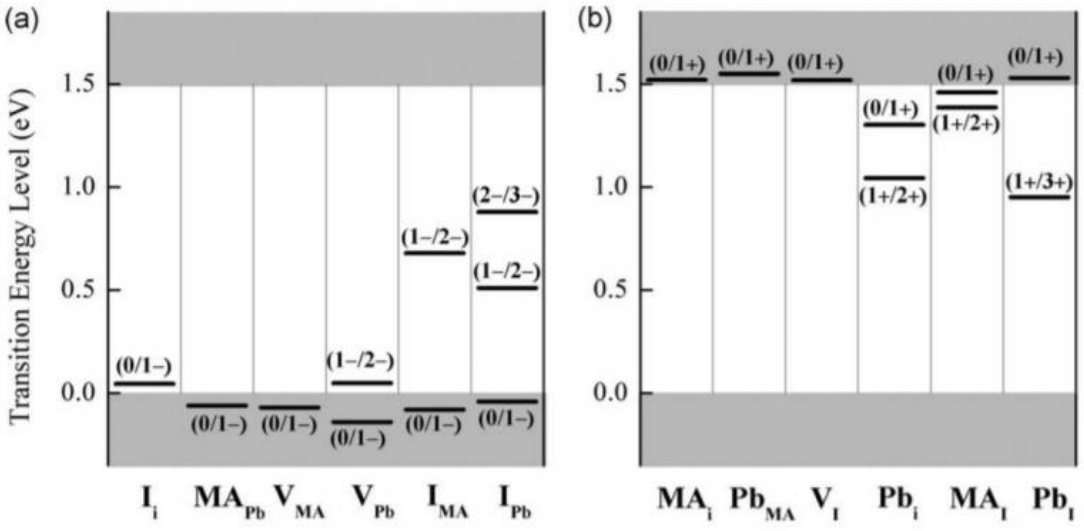


Figure 2.6 Theoretically calculated energy levels of different point defects present in perovskite structure ($CH_3NH_3PbI_3$) [53].

### 2.2.2 Defect Ion Migration Channel in Perovskites

Defect ions can move inside the bulk of the material and gather at the interfaces of the perovskite solar cells with the influence of external electric field. As shown in the Fig. 2.7, accumulated ions can create an internal electric field which directly affect the input voltage and introduce hysteresis. Both positive poling and negative poling are created depending on the direction of the electric filed and movement of the defect ions (Figure 2.7a and b). All the movements of the ions are based on hopping or jumping of each individual defect ions to the specific perovskite lattice structure.

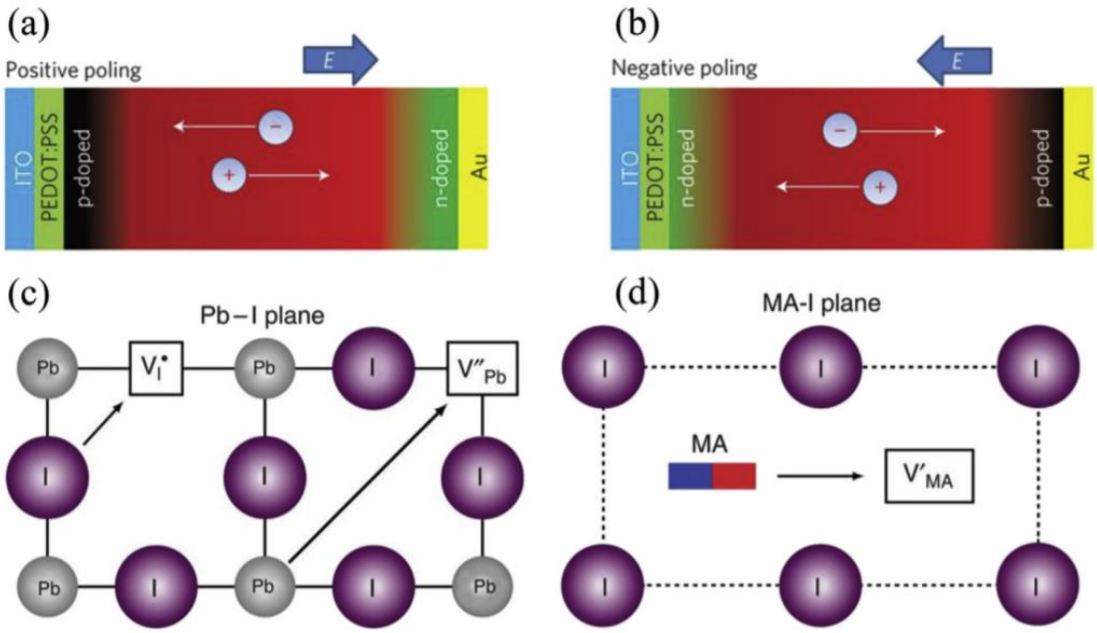


Figure 2.7 Defect ion migration in perovskite device by (a) positive and (b) negative poling. (c, d) Three ionic transport mechanisms in $MAPbI_3$ perovskites. (c) Pb and I vacancies. (d) MA vacancies [54].

As shown in the Fig. 2.7c and d, $MA^+$, $Pb^{2+}$ and $I^-$ ions have their own migrating direction. For the $Pb^{2+}$ ions to migrate and take a place of vacant Pb, it has to be moved in a diagonal direction as shown in the figure while iodide ion also has to follow the same path in Pb-I plane. $MA^+$ jumps into the empty cage near to its position. All the movements of the ions are based on hopping or jumping of each individual defect ions. All the movement of these commonly defect ions depend on a term known as the activation energy of the ion. Ions with less activation energy are easily moved and form the defect states while ions with high activation energy cannot move easily and thus possibility of forming defect is less likely. $MA^+$, $Pb^{2+}$ and $I^-$ defect ions have less activation energy which makes these ions more vulnerable to defect creation and results in ion migration.

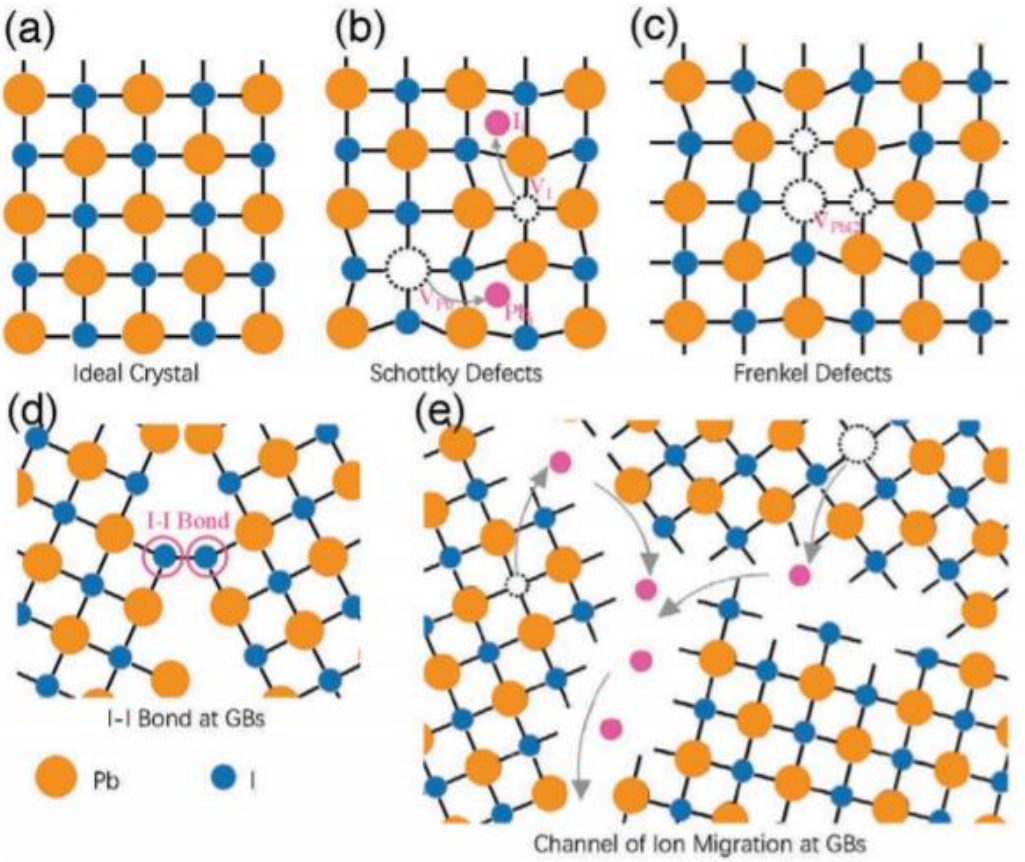


Figure 2.8 Structure showing a) ideal crystal, b) Schottky defects of vacancies ($V_{Pb}$, $V_I$) and interstitials ($Pb_i$ , $I_i$ ), c) Frenkel defects of vacancies ($V_{PbI2}$), d) I-I Bond at GBs. e) The channel of ion migration facilitated by open space and dangling bonds at GBs [55].

The point defects in perovskite can be also be called as Schottky defect and Frenkel defect depending on their functionality. When the cation and anion move from their corresponding lattice sites and create vacancies then they are called Schottky defect (Figure 2.8b). As both cation and anion leave, therefore overall neutrality remains. Frenkel defect is where an atom leaves its initial lattice site and occupies an interstitial position on the same

crystal (Figure 2.8c). Figure 2.8a shows the ideal perovskite crystal without any defects, Schottky defects (Figure 2.8b) and Frenkel defects (Figure 2.8c) in perovskites. Generally, Schottky defects ($PbI_2$ and MAI vacancy) reduce the carrier lifetime but they do not create any trap states in the perovskites. However, trap states are created by the Frenkel defects (Pb, I, and MA vacancies) in $MAPbI_3$ perovskites. Other than the point defects, dangling bond at the GB create trap states which act as the recombination center for electrons and holes. Figure 2.8d shows the I-I dangling bond at the GB of the perovskites. Defect ion migration is facilitated by the path created due to the GB as shown in Fig. 2.8e. This defect ion migration across GB results in hysteresis for perovskites current voltage curves.

### 2.2.3 Accumulation of Defects in Perovskites GB

The point defects in perovskites including interstitials, vacancies, and anti-site defects are most likely to be present in the GB. Bahrami et al. worked with the two common perovskites such as $MAPbI_3$ and mix cation-halide where point defects are mostly concentrated in GB of the perovskites [56]. Figure 2.9 shows the accumulation of point defects across the GB in perovskites $ABX_3$ where $B=Pb^{2+}$. In $MAPbI_3$, two major point defects are interstitial ($I_i$, $MA_i$) and vacancies ($V_I$, $V_{MA}$) [53]. Figure 2.10 shows the electronic band structure at GBs for MAPbI3 and FAMACs mix cation perovskites. $MA^+$ and $I^-$ are more exposed to ambient environment and create vacancies $V_{MA}$ and $V_I$, respectively [57]. These mobile point defects facilitates ion migration that take place via GBs rather than bulk of the grain [46]. Interstitial ($I_i$, $MA_i$) and vacancies ($V_I$, $V_{MA}$) are more likely to be present at GBs that act as recombination centers for photogenerated charge carriers in perovskite solar cells [58].

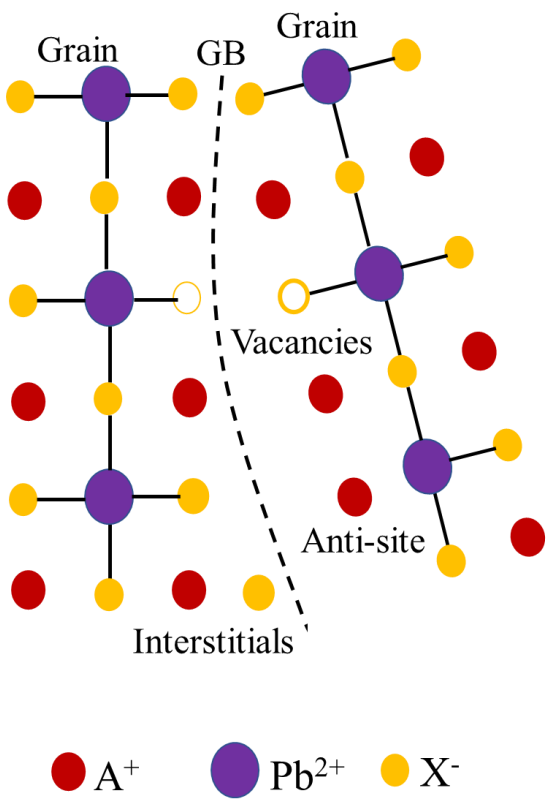


Figure 2.9 Accumulation of point defects across the GB in perovskites $ABX_3$ where $B=Pb^{2+}$.

FAMACs $[Cs_5(MA_{0.17}FA_{0.83})_{95}Pb(I_{0.83}Br_{0.17})_3]$ perovskites have mixed cations ($Cs^+/FA^+/MA^+$) and halide ions ($I^-/Br^-$) in structure instead of single cation in $MAPbI_3$ structure can ease the formation of point defects. Inorganic Cs is likely to contribute to a closed packed perovskite crystal structure (less interstitial space) where point defect formation is quite difficult with increase of formation energies upon cation mixing [59, 60]. Bromide ions migrate with sufficient difficulty compared to iodide ions which helps to reduce the formation of point defects [14]. Lower density of trap states results in reduced ion migration. Whereas in $MAPbI_3$ has higher density of trap states that results in significant defect ion migration.

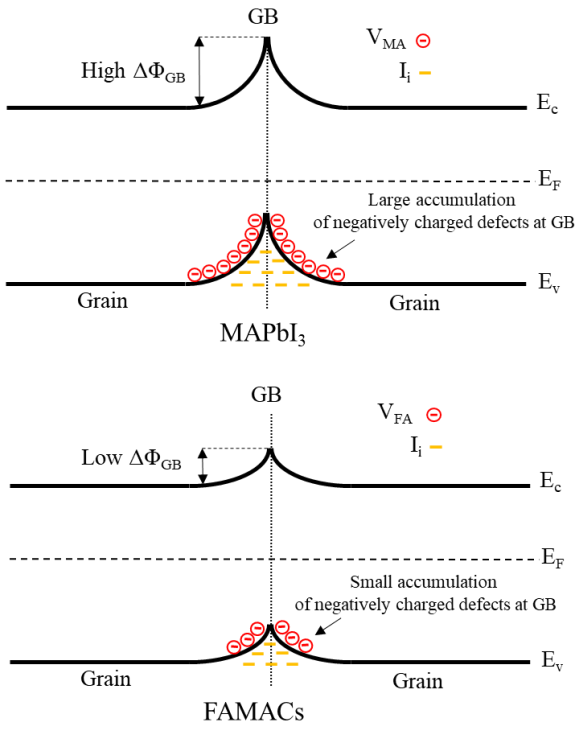


Figure 2.10 Electronic band structure at GBs for $MAPbI_3$ and FAMACs perovskites [56].

### 2.2.4 GB Dominated Defect Ion Migration in Perovskites

As defect ions tend to accumulate at the GB of the perovskite material, there is a possibility that GBs are dominated by defect ion migration and results in current voltage hysteresis. Shao et al. have studied the grain boundary of $MAPbI_3$ perovskite solar cells using atomic force microscopy (Figure 2.11) [46]. They measured dark current hysteresis in nanoscale using atomic force microscopy [46]. Figure 2.11 shows the atomic force microscopy topography of a $MAPbI_3$ perovskite containing grain and GB. Dark current was measured at grain and GB both in forward and reverse scan direction. At GB, current voltage curve in both in forward and reverse scan direction shows clear hysteresis.

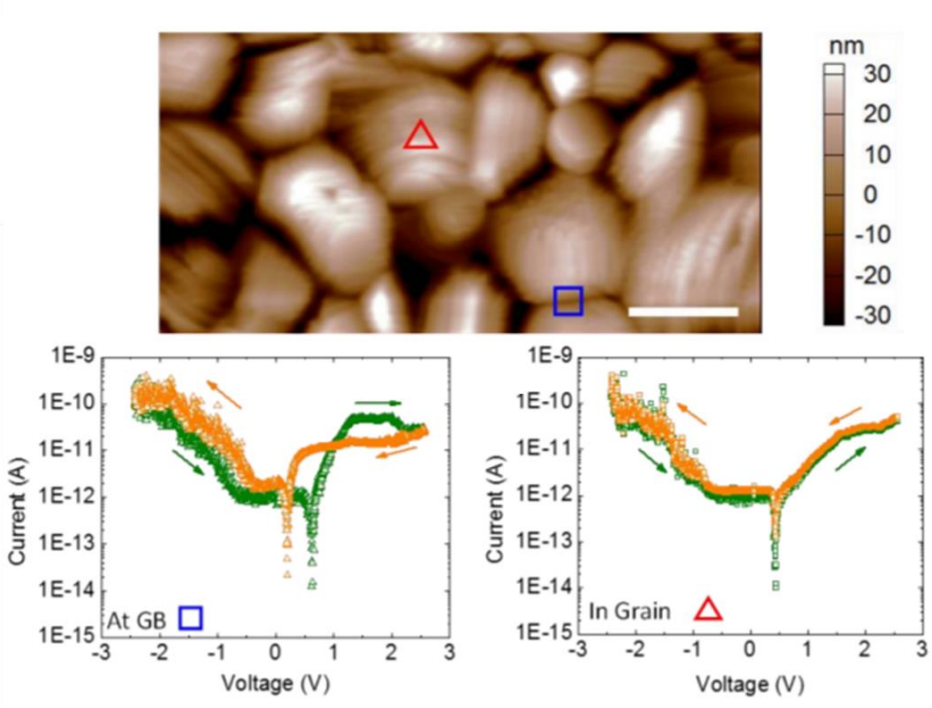


Figure 2.11 GB dominated ion migration in $MAPbI_3$ perovskites [46].

However, current voltage curve in both in forward and reverse scan direction at grain does not show hysteresis. This clearly proves that all the defect ions present in perovskites accumulate at the GB and migrate surrounding the GB area.

## 2.3 Summary

This chapter discussed about the point defects present in perovskite and their higher concentration present at the GB. These defects largely responsible for electron hole recombination at the perovskite, transport layer interface and contacts which prevent perovskite to reach higher PCE at large area of the cells. With increasing cell area, these defects become more significant. Bigger cell area is a prerequisite for perovskite solar cells to be commercialized. Therefore, nanoscale study of perovskite GB defects and its passivation are vital for perovskite solar cell to be available in the PV market.

# Chapter 3 Experimental Methods Adapted in This Study

## 3.1 Nanoscale Measurements

To realize the grain boundary defects and its passivation at nanoscale in perovskite solar cells, the following setups have been adapted in this study mainly atomic force microscopy-based measurements.

### 3.1.1 Atomic Force Microscopy Based Measurements

PSCs was mounted in a light-induced transient atomic force microscopy (LT-AFM) configuration (Figure 3.1) for measuring the apparent charge carrier recombination lifetime ($\tau_r$) and transport time ($\tau_t$). Then, diffusion length ($L_D$) was calculated based on these transient parameters ($\tau_r$ and $\tau_t$). Agilent 5500 AFM was used for the LT-AFM setup. A silicon conductive tip coated with platinum/chromium from Budget Sensors was used for transient photovoltage (TPV) and transient photocurrent (TPC) scans. The AFM was connected with mixed signal oscilloscope (Agilent MSOX4154A). Charge carriers were generated at 532 nm wavelength using a green laser (model: MGL-I-532 DPSS). Device equivalent circuit for TPV and TPC measurements in perovskite solar cells is shown in Fig. 3.5. Channel impedance of 1 MΩ was used to keep the device open circuited for collecting TPV decays, while 50 Ω channel impedance was used to keep in short circuited for acquiring TPC decays. The 1 MΩ , 50 Ω resistance are also called sampling resistance for signal acquisition [61]. TPV decays with $R_o$ =1 MΩ were fitted to obtain the charge recombination lifetime [61] while TPC decays with $R_o$=50 Ω were fitted to obtain the charge transport time [61, 62]. Figure 3.1 shows the schematic diagram of light-induced transient atomic force microscopy (LT-AFM) based instrumentation based on CAFM.

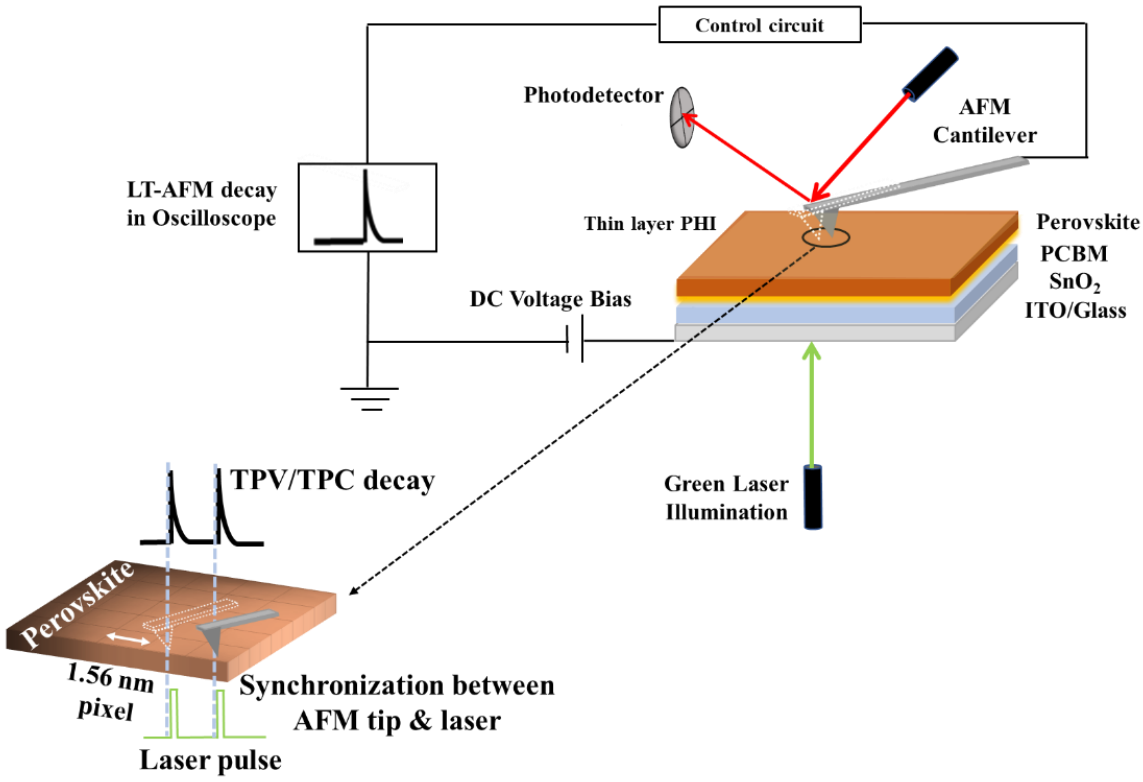


Figure 3.1 Schematic diagram of light-induced transient atomic force microscopy (LT-AFM) based instrumentation based on a conductive-AFM.

### 3.1.2 Custom Design Sample Holder for AFM Measurements

To perform the LT-AFM measurements, a house custom AFM sample holder was designed and made as shown in Fig. 3.2. The schematic diagram shows the parts that were incorporated into the design such as prism, colemaric lens, beam splitter and a housing area for optical fiber cable. It was designed and built by specialist specifically to perform the measurements at nanoscale to fully understand the charge carrier dynamics and its relation to the GB passivation effect. This sample holder can also be used to measure the surface potential and conductive AFM images.

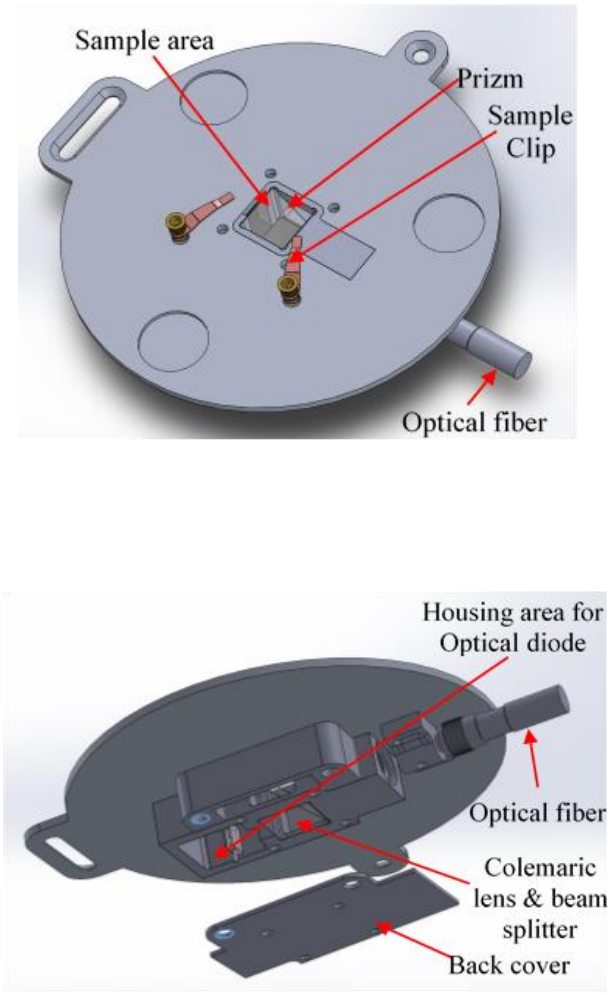


Figure 3.2 Schematic diagram of the customized sample holder used in atomic force microscopy measurement (a) front end and (b) backend.

Figure 3.3 shows the sample holder that was used to perform the LT-AFM measurements. On the front side, there is a connector which is used to hold any wire from the AFM nose cone to have connection externally. On the rear side, there is BNC connector which can be used to connect the AFM nose cone externally to an amplifier. Amplifier can be used externally to get high resolution in time scale.

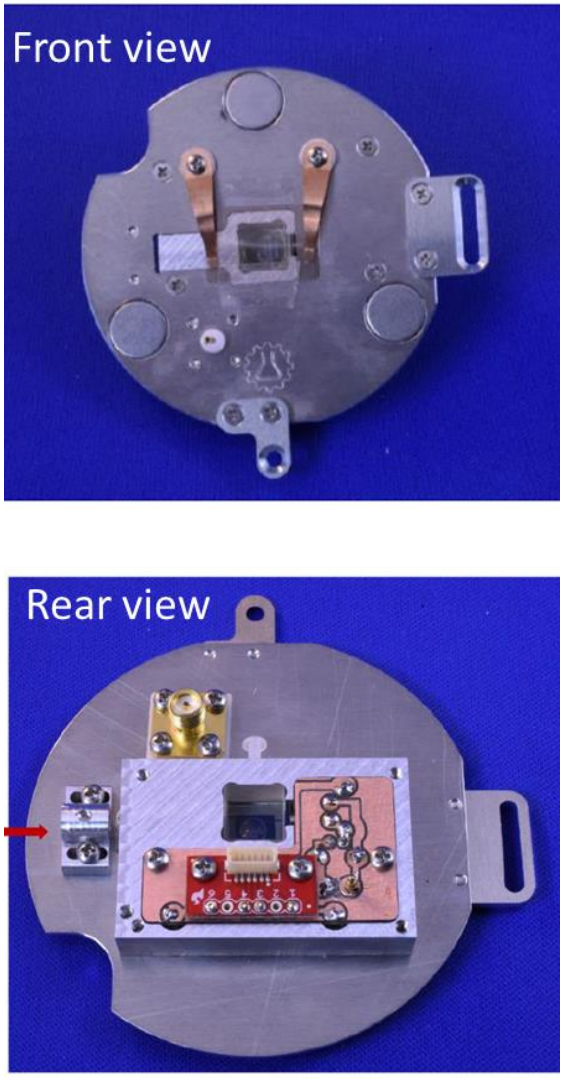


Figure 3.3 Custom design sample holder used in atomic force microscopy measurement (a) front end and (b) backend.

Figure 3.4 shows the electrical circuit diagram of the photodetector circuit used in the sample holder. There is photodiode which is used to detect the light and electrical signal is received from the connector in response to light. It uses a battery to get power from and thus perform the light to electricity conversion. Also, it contains connection for sample holder clips.

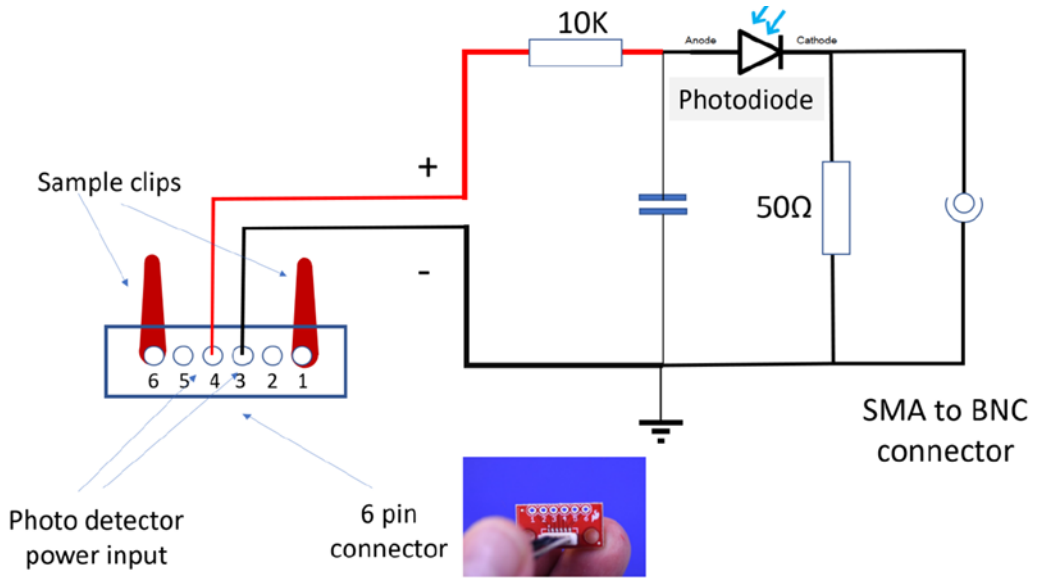


Figure 3.4 Electrical circuit diagram of the photodetector circuit used in the sample holder.

### 3.1.3 TPV, TPC and Diffusion Length Calculation

TPV decays were fitted using equation 3.1 to obtain charge recombination lifetime that has been reported in different types of solar cells [61].

$$Y(t) = Y_0 \exp\left(-\frac{t}{\tau_r}\right) \qquad 3.1$$

where, $Y_0$ is steady state photovoltage, and $\tau_r$ is time constant representing charge carrier recombination lifetime. Photogenerated charges are recombined within the device when the device is kept open circuited by an oscilloscope channel impedance of 1 MΩ. Equation 3.1 was used to fit a typical TPV decay (Figure 4.9) which resulted in a $\tau_r$ of 11.86 µs. Similarly, nanoscale $\tau_r$ mappings were obtained by fitting the 4096 TPV data with equation 3.1. TPV decay were well fitted mono exponential decay function instead of a double exponential function which suggests that only a single recombination mechanism contributes to the time constants and governs the entire recombination processes. This

single recombination process can be ascribed to non-radiative recombination lifetime [63-65]. TPC decays using equation 3.2 were fitted to obtain charge transport time [61, 62].

$$X(t) = X_0 \exp\left(-\frac{t}{\tau_t}\right) \quad 3.2$$

where, $X_0$ is steady state photocurrent, and $\tau_t$ is time constant representing charge carrier transport time. Photogenerated charges are collected from the device when the device is kept short circuited using an oscilloscope channel impedance of 50 Ω. A characteristic TPC decay curve (Figure 4.9) for FAMACs perovskite acquired through our LT-AFM. Equation 3.2 was used to fit the TPC decay which lead to a $\tau_t$ of 6.50 μs. Likewise, nanoscale $\tau_t$ mappings were acquired by fitting the 4096 TPC data with equation 3.2.

Carrier diffusion coefficient ($D_n$) can be obtained by the following equation [66-69]

$$D_n = \frac{L^2}{2.35 \times \tau_t} \quad 3.3$$

where, $\tau_t$ is the carrier transport time and L is the active layer thickness.

The charge carrier diffusion length ($L_D$) can be obtained from carrier diffusion coefficient ($D_n$) and charge carrier recombination lifetime ($\tau_r$) using equation 3.4 [68-71]

$$L_D = (D_n \times \tau_r)^{0.5} \quad 3.4$$

Control and post treated FAMACs perovskite samples of 100 nm × 100 nm size area were scanned using our LT-AFM. The actual resolution of the measurement was found to be ~ 9.57 nm. Detail calculations of AFM resolution have been provided in Fig. 3.6. The high spatial resolution was achieved by the raster scanning of small size 100 nm × 100 nm area by our LT-AFM. A Labview program was used to synchronize the laser illumination with the movement of AFM tip. During the AFM tip scanning at a point/pixel, the laser illuminates precisely at that time and then the signal was taken out from the tip via breakout box connected to the oscilloscope. Transient TPV and TPC data were read automatically

from the oscilloscope by a Labview program. Our measurement is on perovskite samples of 100 nm × 100 nm area with 64×64 pixels. Increasing to the pixel size such as 128×128 pixels will take several hours for the measurement which most likely can cause the degradation of the AFM tip. Consequently, measurement artifacts will appear, and mapping images become more susceptible to inaccuracy. As the measurement is stable for data acquisition in 64×64 pixels, we selected 100 nm × 100 nm small area that covers the grain boundary and grain which is the focus of our study. Each pixel size in our measurement is 1.56 nm (100nm/64 pixel). Large size image of the lifetime and transport time mapping with 64×64 pixels will increase each pixel size which will decrease the quality of the mappings. Furthermore, large size image in 64×64 pixels can bring inaccuracies in data acquisition as the effective width of grain boundary is of several nanometers. large-size image of the lifetime mapping might result in inaccuracy and quality of the images will decrease.

We think that our LT-AFM setup is a representation of the TPV/TPC setup used to measure lifetime/transport time in actual device configuration [56]. Hence, the scientific analysis/ model tailored to define the TPV/TPC in real device would be comparable for the local TPV/TPC analysis. In TPV, miniature light perturbation raises extra carrier density in the sample. The time constants are related with the recombination rate of these extra charge carriers within the sample. The decay of the voltage transient due to the miniature perturbation is given by [72]

$$\frac{d\Delta V}{dt} \propto \frac{d\Delta n}{dt} = -\frac{\Delta n}{\tau} \qquad 3.5$$

Where ΔV is the photovoltage, Δn is the change in the density of photogenerated carriers due to the light pulse and τ is the resultant recombination lifetime. This equation 3.5 indicates to first-order kinetics of $\Delta V \propto \exp\left(-\frac{t}{\tau}\right)$ [73] which actually means recombination of additional charge carriers due to light perturbation supports the exponential decay fitting. TPV/TPC time constants and PL lifetime generally varies in the same material as the charge processes and measurement conditions for both are different [74, 75]. TPV/TPC decay are primarily dominated by the recombination due to the charge buildup at the interfaces while PL lifetime is defined by the bulk recombination [76]. In the TPV/TPC experiment, interface between metal tip and perovskite influences the recombination processes and thus time constants are larger compared with the PL lifetime. It is more suitable to clearly state that this is the apparent recombination lifetime and transport time measured with metal (AFM tip)-perovskite interface. Furthermore, in this experiment, recombination lifetime range is greater than transport time which indicates that charges can be collected before they recombine. Another commonly used term as dielectric relaxation time depends on the series resistance. Dielectric relaxation time for perovskite is not identical with time measured by TPV/TPC [77]. The time obtained in this experiment by TPV/TPC could not be interpreted by dielectric relaxation time.

Device equivalent circuit for TPV and TPC measurements in perovskite solar cells is shown in Fig. 3.5. Channel impedance of 1 MΩ was used to keep the device open circuited for collecting TPV decays, while 50 Ω channel impedance was used to keep in short circuited for acquiring TPC decays. The 1 MΩ , 50 Ω resistance are also called sampling resistance for signal acquisition [61].

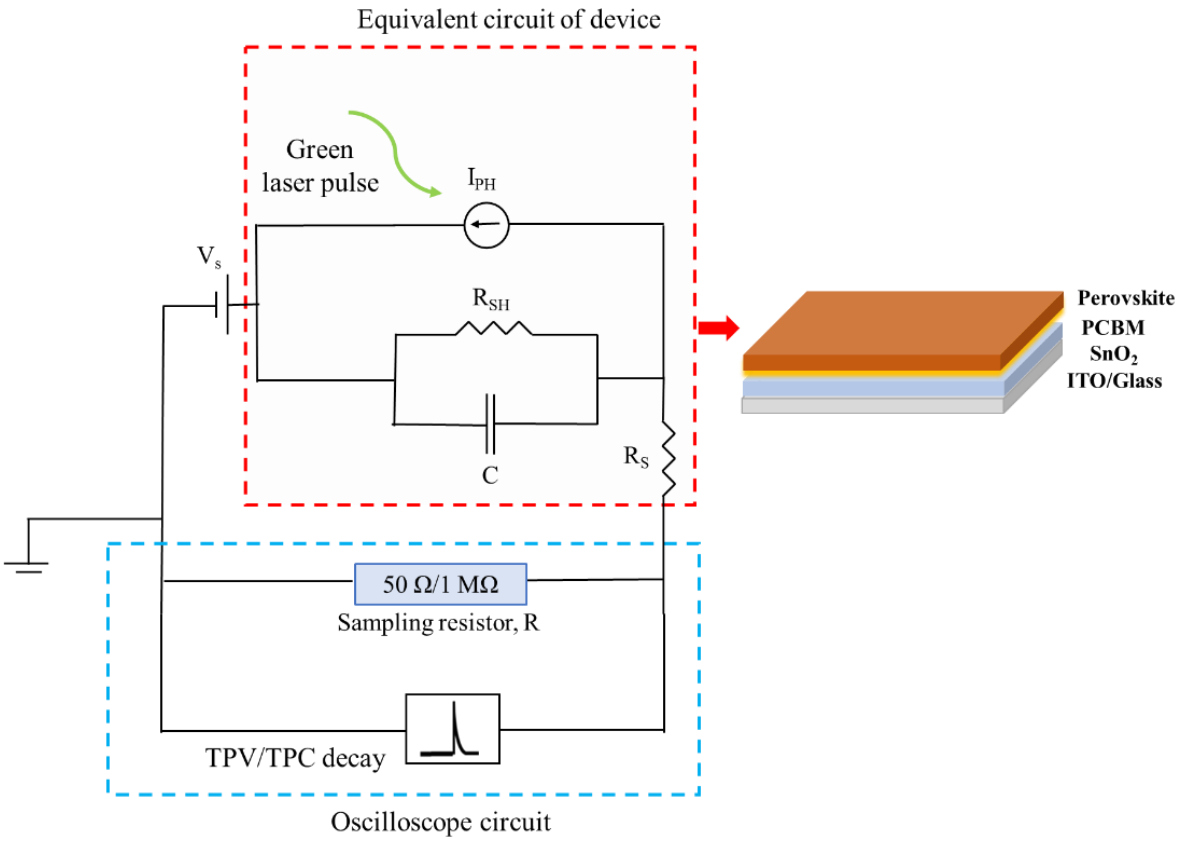


Figure 3.5 Device equivalent circuit for TPV and TPC measurements in perovskite solar cells.

Figure 3.5 shows equivalent circuit of transient photocurrent (TPC) and photovoltage (TPV) measurements. $R_{SH}$ is the charge recombination resistance, $R_s$ is the series resistance of the film, C is the capacitance and R is the channel impedance of the oscilloscope [61, 62]. The device was short circuit using R=50Ω to record TPC decays and kept in open circuited using R=1 MΩ channel impedance of the oscilloscope to acquire TPV decays. Photogenerated charges flow outside of the device at R= 50 Ω (short circuit condition) [61]. On the contrary, photogenerated charges do not flow outside of the device at R= 1 MΩ i.e. acts as open circuit condition and charges recombine within the perovskite [61]. This equivalent circuit model has been used for TPV and TPC measurements [61, 62].

3.1.4 Actual Resolution of The Measurement

In general, the geometry of the SPM tip can be determined using blind tip estimation algorithm from sample surface [56]. Figure 3.6a shows AFM tip geometry obtained from blind estimation algorithm of Gwyddion software [78]. Figure 3.6b is the line profile of the AFM tip from Fig. 3.6a, which was used to estimate the tip diameter [79]. The AFM tip radius (R) is around 11 nm.

The AFM vertical resolution ($\Delta Z$) = $\sqrt{\frac{4K_BT}{3k}}$ where $K_B$, T and k are Boltzman constant, absolute temperature (298 $^{o}$K) and spring constant of cantilever (k=0.2 N/m). The AFM lateral resolution = $\sqrt{8(R+r)\Delta Z}$ where R, r, $\Delta Z$ are estimated tip radius, sample feature size radius, AFM vertical resolution, respectively [79-81]. Figure 3.6c and d show the topography and line profile of FAMACs perovskite film, respectively to estimate the perovskite feature size radius, r = 20 nm. AFM vertical and lateral resolution were found at 0.37 nm and 9.57 nm, respectively. LT-AFM vertical and lateral resolution were found to be 0.37 nm and 9.57 nm, respectively (Figure S8). Due to sharpness (tip radius~10nm) of the conductive AFM tip, both vertical and lateral resolution were high. We believe that charge carriers will spread into a large area, especially at ITO side due to its large conductivity. However, high vertical resolution of the tip (0.37 nm) will allow most of the charge carriers to flow directly through tip apex. Although there will be some charges flowing across the lateral position of the AFM tip caused by the edge effect, charge carriers from larger area could not affect the measurement owing to high lateral resolution (9.57 nm). We believe that high spatial resolution could be achieved due to low tip radius including negligible dependence on edge effect.

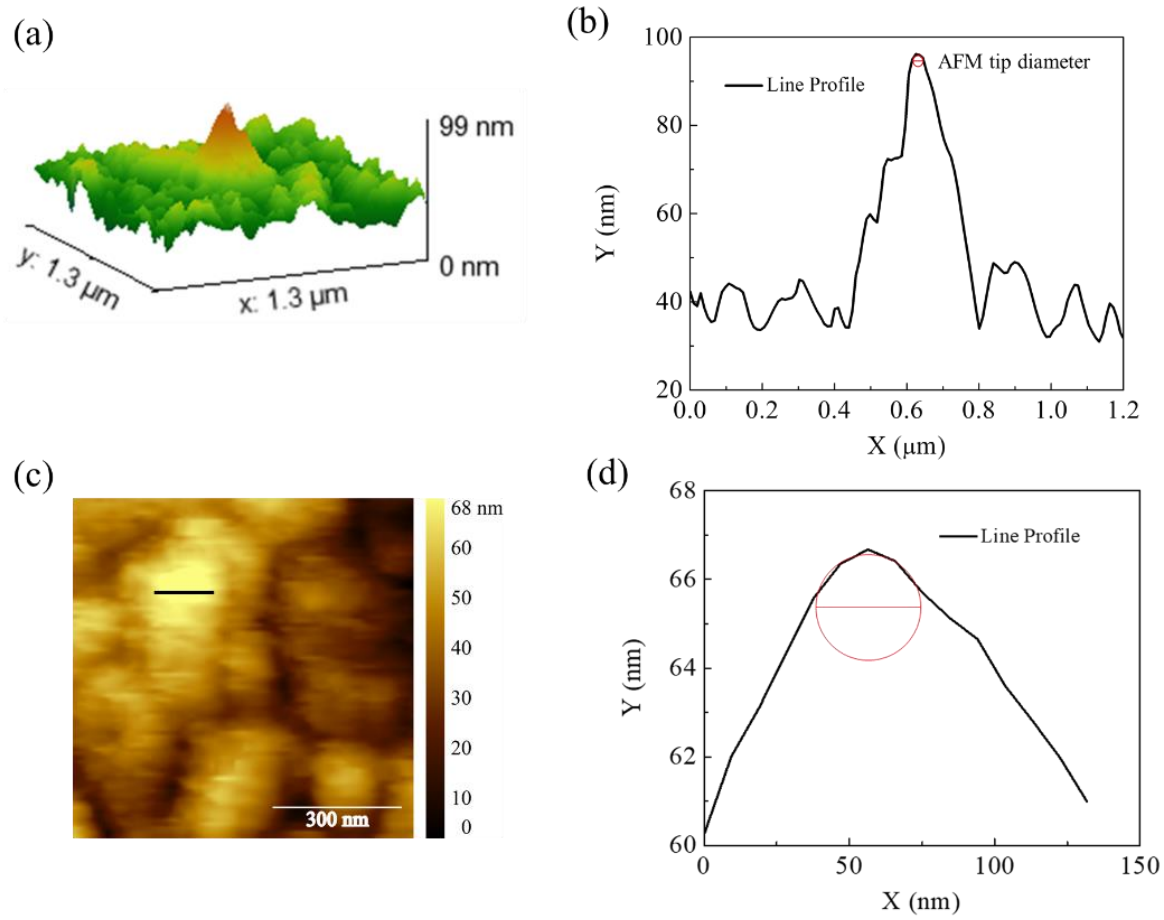


Figure 3.6 (a) AFM tip geometry obtained from blind estimation algorithm, (b) Line profile of the AFM tip from Fig. 3.6a. (c) AFM topography of control perovskite, (d) line profile (black line) in Fig. 3.6c of perovskite feature.

### 3.1.5 Kelvin Probe Force Microscopy: GB Defects from Surface Potential Images

Kelvin probe force microscopy (KPFM) measurements were done on perovskite samples with amplitude modulation by Agilent 5500 AFM in non-contact mode. A Cr/Pt coating tip (Multi75E-G from budget sensor) was used for this measurement. Tip resonance frequency and force constant were 75 kHz and 3N/m, respectively. Electrostatic force

between the tip and sample was induced by the electrical oscillation of the tip. This electrostatic force was annulled by a DC offset voltage to the scanning tip. The KPFM measures contact potential difference ($V_{CPD}$) between the tip and sample with topography, simultaneously. An electrostatic force is generated between the tip and sample because of the difference in their Fermi energy levels, when the scanning tip approaches the sample surface. Applying a DC voltage offset on the scanning tip on the sample nullifies this electrostatic force. $V_{CPD}$ between the AFM tip and the sample is defined as [82]:

$$V_{CPD} = \frac{\varphi_t - \varphi_s}{-e} \tag{3.6}$$

where $\phi_t$ and $\phi_s$ are the work-functions of the tip and sample respectively and e is the elementary charge. The work function of the tip is constant since we have used the same tip for all the samples. Therefore, the difference between the grain interior and the GBs gives the GB potential barrier. These type of measurements have also been implemented by other groups[83].

The average SP related to position of $x_i$ [as shown in Fig. 4e (i-vi)] was calculated by using equation 3.7. The average surface potential at $x_i$ place with all j pixels can be described as [56]

$$SP_{x_i} = \frac{\sum_{j=1}^{k} SP_{(i,j)}}{k}, 1 \le i \le l \tag{3.7}$$

where, $SP_{x_i}$ is surface potential of pixels at (i, j) position. k and l are the pixels counts identical to x-axis and y-axis, respectively. The charge carrier concentration at GBs can be calculated from the SP images acquired using KPFM [58, 84]. The net doping density of perovskite can be calculated from the barrier height of band bending and the width of the

GBs [58] because the GBs of perovskite are electrically charged. The net doping ($P_{net}$) and density of trap states at GB ($P_{GB\text{-}trap}$) are calculated from the following equations [56, 84-86]

$$P_{net} = \frac{2\varepsilon_0\varepsilon_r\Delta\varphi_{GB}}{e^2 W_{GB}^{\ 2}} \quad 3.8$$

$$P_{GB\text{-}trap} = \frac{1}{e}\sqrt{8\varepsilon_0\varepsilon_r P_{net}\Delta\varphi_{GB}} \quad 3.9$$

where $\varepsilon_0$, $\varepsilon_r$ are the permittivity of free space and dielectric constant respectively, $\Delta\varphi_{GB}$ and $W_{GB}$ are the average GB potential and SCR width respectively (obtained from the average SP profiles) and e is the elementary charge.

## 3.2 Microscale Measurements

To realize the grain boundary defects and its passivation at microscale level in perovskite solar cells, the following setups have been adapted in this study mainly materials and device fabrication and characterization.

### 3.2.1 Materials and Device Fabrication

Indium doped tin dioxide (ITO) coated glasses (1.5 cm × 1.5 cm) were used as substrates for the fabrication of perovskite solar cells. Substrates were cleaned with Soap water, DI-water, acetone, and isopropanol (IPA) for 30 minutes each in ultra-sonication bath. Then oxygen plasma treatment was done for 30 minutes.

Tin oxide ($SnO_2$) was diluted with water to 2.67%. $SnO_2$ thin layer was deposited via spin coating at 3000 rpm for 30 sec and put into the hotplate for annealing at 150$^{o}$C for 30

minutes. 10 mg PCBM in 1 mL of Chlorobenzene was used to prepare the solution and then spin coated in two steps. Firstly. spin coating parameter was 3000 rpm for 30 sec and then followed by 4000 rpm for 5 sec. After that samples were annealed at 80° C for 10 minutes.

462 mg $PbI_2$/ml DMF was used to prepare the solution of $PbI_2$. $PbI_2$ was purchased from Acros Organics. The solution was prepared by stirring for 2 hr on a hot plate inside the glovebox. The temperature of the hot plate was 70 $^oC$. $PbI_2$ solutions were deposited via spin coating at 4000 rpm for 45 sec. Annealing at 70 $^oC$ for 30 min was done for crystallization. 10mg MAI /ml Isopropanol solution was prepared. Then $PbI_2$ was dip coated into this solution for 1.0 min followed by instant spin coating of $MAPbI_3$ perovskite films at 6000 rpm for 10 sec. Then annealing at 100$^oC$ for 15 min was used for film formation.

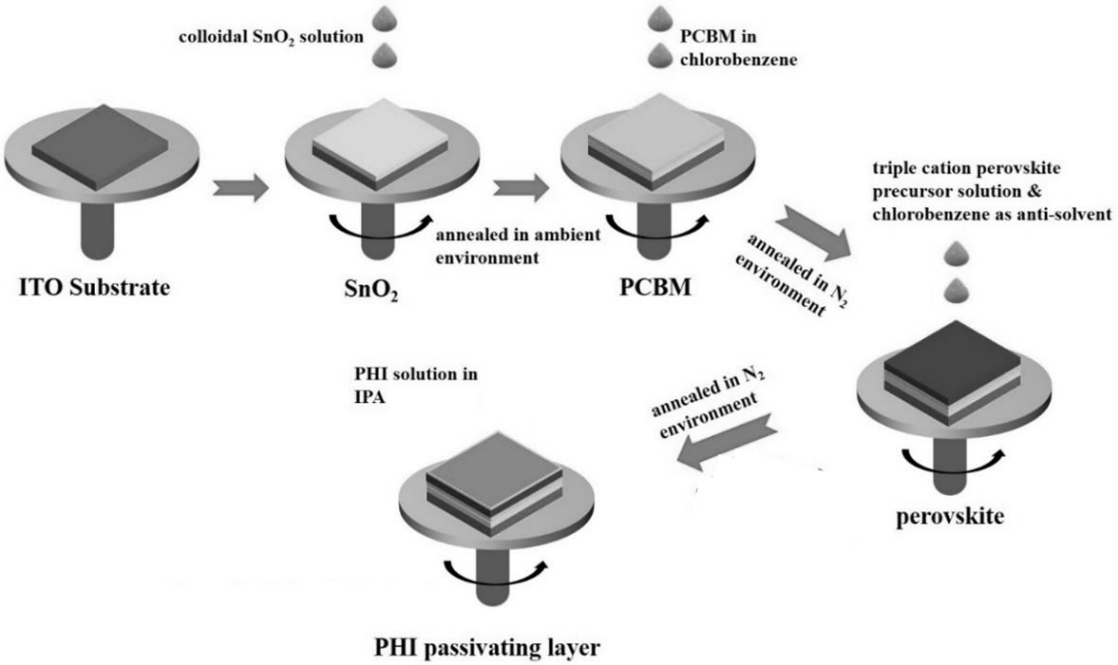


Figure 3.7 Spin coating deposition steps in fabricating PHI based perovskite solar cells.

The procedure adapted by Saliba et al. [87] was followed in detail to prepare the perovskite precursor solution. The mixed perovskite precursor solutions contain FAI, $PbI_2$, MABr, and $PbBr_2$ with mole ratio is 1:1.1:0.2:0.2 respectively in anhydrous DMF/. Then 1.5M CsI was added to the stock solution. The volume ratio of FAI, $PbI_2$, MABr, and $PbBr_2$ and CsI is 95:5. Two step spin coating steps of 1000 rpm for 10 sec and followed by 6000 rpm for 20 sec were adapted to deposit the perovskite layer. Then PCBM layer was deposited on perovskite. Chlorobenzene was used as an anti-solvent and dripped during the spin coating (Figure 3.7). Then perovskite films were annealed at 100°C for 45 minutes. Different concentration of PHI as passivating layer was spin coated on top of perovskite layer at 6000 rpm for 20s (Figure 3.7).

Phenyl hydrazine with hydriodic acid (HI) (57wt% in water) was made to be mixed at 0°C for synthesizing the phenylhydrazinium iodide (PHI). 10 mL of $C_6H_5NH_2NH_2$ and 25 mL methanol were mixed to prepare the solution. After that drop by drop 10 mL of HI (57 wt%) was added into the above solution with stirring. Then mixture was constantly stirred at room temperature for 3 hours. With the help of a rotary evaporator, the solvent was removed at 60°C. Diethyl ether was used for washing the obtained crude powder. Lastly, recrystallization was done with the help of a mixed solvent of ethanol and diethyl ether. Then white solid obtained was dried in vacuum at 60°C for 14 hours and was ready to be used. The hole transport layer Spiro-OMeTAD was prepared by mixing 43mg Spiro-OMeTAD, 17 µL of TBP, 0.5 ml of chlorobenzene, , 9.5 µL solution from 78 mg Li-TFSI and 180 µL of Acetonitrile mixture and 6.28 µL solution from 50 mg cobalt salt and 200 µL of acetonitrile mixture. Spiro-MeOTAD was then deposited on the PHI layer via spin

coating at 4000 rpm for 20 sec (Figure 3.7). Then the substrate was kept in dark and dry condition for 12 hours. Lastly, silver (80 nm) was thermally evaporated as top electrode.

### 3.2.2 Film Characterization: UV-Vis, XRD, Photoluminescence, SEM

Agilent 8453 UV−Vis spectrophotometer was used to acquire UV-Vis absorbance spectra of perovskite samples (Figure 3.). High resolution FE-SEM (model: Hitachi S-4700) was used to obtain the cross-sectional SEM images.

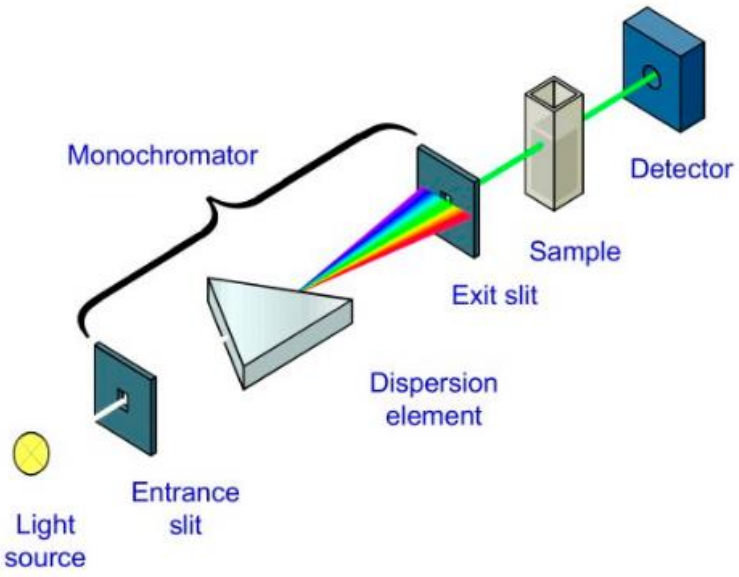


Figure 3.8 Schematic diagram for UV−Vis spectrophotometer setup.

For steady-state photoluminescence (PL) measurement of perovskite samples, FLS 920 fluorescence spectrophotometer was used. An excitation wavelength applied at 395 nm wavelength to do the photoluminescence (PL) measurement of perovskite samples. For the XRD measurements, Rigaku smartlab XRD was being used to see the diffraction of the perovskite and PHI crystals formed.

### 3.2.3 Current Density vs Voltage (J-V) Measurements

Semiconductor parameter analyzer (Agilent 4155C) was used to measure the current density−voltage (J−V) characteristics of the perovskite solar cells under one sun illumination from a Newport solar simulator with an intensity of ~100 mW/cm$^2$ (AM 1.5). Light intensity was calibrated using a standard reference solar cell (S1133 14-01) from National Renewable Energy Laboratory (NREL). Active area of all the solar cells were 0.08 cm$^2$. Forward and reverse scan were from 0 V to 1.20 V and 1.20 V to 0 V respectively with a scan rate 0.5 V/s. Figure 3.9 shows the schematic diagram for the current density vs voltage (J-V) measurements setup containing power supply, Newport xenon lamp, monochromator, and semiconductor parameter analyzer. This setup was adapted from Adhikary et al. which is commonly used to measure the current voltage characteristics of a solar cell [88]. This current voltage characteristics gives the power conversion efficiency and fill factor of the solar cells adapted in this study.

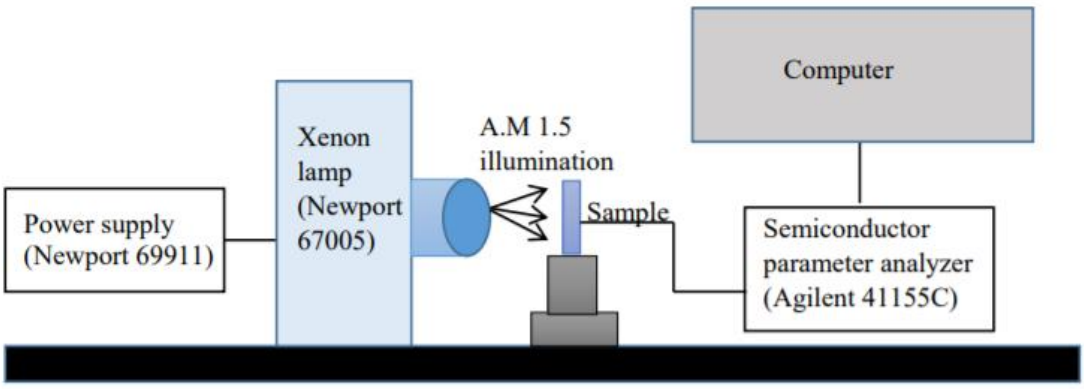


Figure 3.9 Schematic diagram for current density vs voltage (J-V) measurements setup [88].

### 3.2.4 External Quantum Efficiency (EQE) Measurements

Xenon lamp and monochromator (Newport) were used for measuring the external quantum efficiency (EQE). Two lenses were used to focus the monochromatic light on active area of solar cells. For EQE measurements, the same NREL calibrated solar cells were used as reference. A standard reference solar cell (S1133 14-01) from National Renewable Energy Laboratory (NREL) was used to calibrate the setup for EQE measurements. Figure 3.10 shows the schematic diagram for the EQE measurements containing power supply, Newport xenon lamp, monochromator, semiconductor parameter analyzer, focusing lens and trans-impedance amplifier. This setup was adapted from Adhikary et al. which is commonly used to measure the external quantum efficiency of a solar cell [88]. This external quantum efficiency gives the integrated current density of the solar cells which is similar to current density measured from J-V curves adapted in this study.

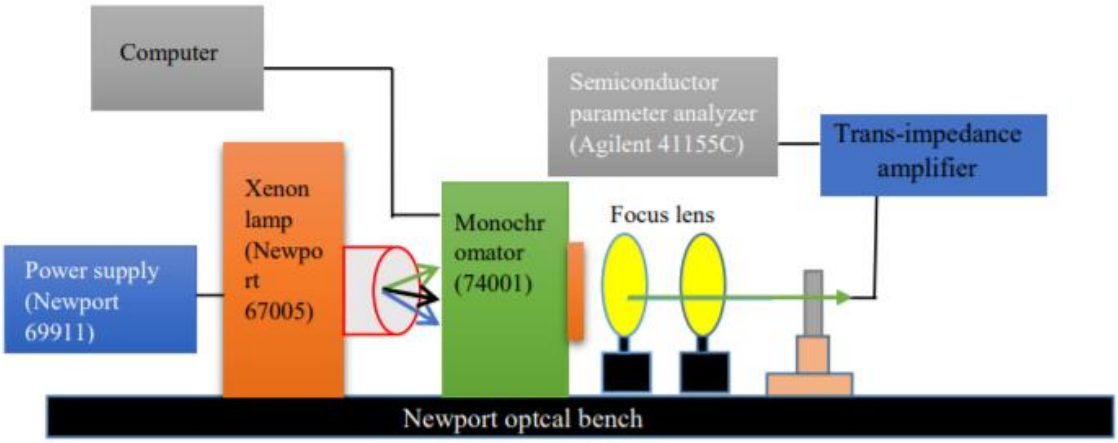


Figure 3.10 Schematic diagram for external quantum efficiency (EQE) measurement setup [88].

# Chapter 4: Results and Discussion

## 4.1 Nanoscale Study of Defects at GB of $MAPbI_3$ and FAMACs Perovskites

Two extensively studied perovskites were implemented to understand defects present at GB of perovskites namely single-cation/halide ($MAPbI_3$) and mixed-cation/halide FAMACs [$Cs_5(MA_{0.17}FA_{0.83})_{95}Pb(I_{0.83}Br_{0.17})_3$] perovskite. At first, KPFM is used to identify the density of defects at each of above-mentioned perovskites, analyze the presence of the defects and then role of individual ions on the point defects. Secondly, conductive AFM is used to measure the dark current hysteresis which reveals the presence of defect ion migration on microstructures such as grain and GB. Study reveals that decreased density of trap states and recombination indicates less ion migration at GBs and hence insignificant hysteresis in FAMACs perovskites. However, regions surrounding GBs in $MAPbI_3$ are more vulnerable to higher density of trap states, which causes ion to migrate and thus produces hysteresis.

### 4.1.1 GB Defect Analysis in Perovskites Using KPFM

To validate presence of point defects at GB region, average density of trap states was calculated from surface potential (SP) obtained by using KPFM [56]. KPFM is a non-destructive approach which is largely used in perovskite solar cells to study carrier transport dynamics, and trap states [89]. Contact potential difference (CPD) between the tip and sample with topography, simultaneously is measured by KPFM. Due to the difference in their fermi energy levels when the scanning tip approaches the sample surface, an electrostatic force is created between the tip and sample. A DC voltage offset on the AFM tip on the sample annuls this electrostatic force. The work function of the tip

should not be changed i.e. error is less since the same tip has been used for all the samples. Hence, GB potential barrier is obtained from the difference between the grain interior and the GBs. These type of measurements have also been implemented widely [56, 83].

A size of ~100 nm × ~100 nm with three different GB areas were selected marked as white squares in the topography (Fig. 4.1a & 4.1c) and the SP images (Fig. 4.1b & 4.1d) for $MAPbI_3$ and FAMACs perovskites, respectively for calculations of density of trap states at GB ($P_{GB\text{-}trap}$). Defect ion migration greatly impacts the electrical properties of GBs. The number of the accumulated defects limits the barrier height in the GBs [90]. Figure e (i-iii) and e (iv-vi)] of 3 different areas for $MAPbI_3$ and FAMACs perovskites, respectively. Potential at GB is greater compared to the grain interior. Highly oriented pyrolytic graphite (HOPG) is used as a reference sample to validate the less difference in work-function of the AFM tip before and after measurements. AFM topography (Figure 4.1 h, j) before and after KPFM measurement for perovskite samples, respectively and their corresponding surface potential images (i, k).The SP deviation was found to be fewer for FAMACs perovskite film (Fig. 4.1d) compared to $MAPbI_3$ perovskite film (Fig. 4.1b). Less deviation in SP between GBs and GI is suggestive of lower GB potential barrier. The average SP values related to position of $x_i$ [as shown in Fig. 4.1e (i-vi)] was determined by using equation 3.7. The $SP_{x_i}$ profiles for three different areas (areas 1-3 shown in Fig. 4.1b) of $MAPbI_3$ have been shown in Fig. 4e (i-iii). A Gaussian function was used for fitting the $SP_{x_i}$ distribution data to find the maximum average value. GB potential barrier ($\Delta\varphi_{GB}$) is defined as the largest $SP_{x_i}$ at the GB without the $SP_{x_i}$ at the edges of GIs [shown in Fig. 4.1e (i)].

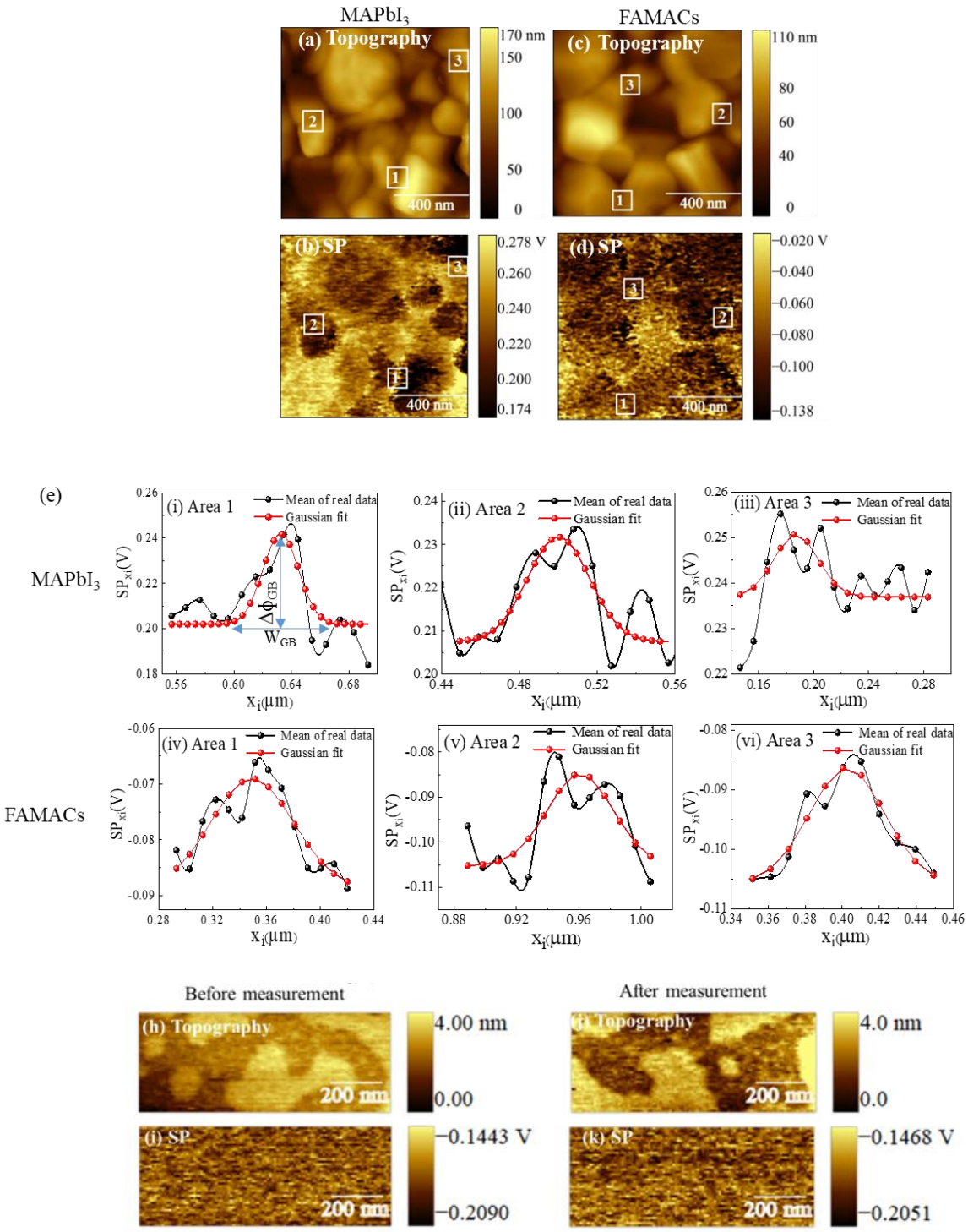


Figure 4.1 AFM topography (a, c) for $MAPbI_3$ and FAMACs perovskite, respectively and their corresponding surface potential images (b, d). Average surface potential profiles at xi

[e (i-iii) and e (iv-vi)] of 3 different areas (marked in topography and SP images) for $MAPbI_3$ and FAMACs perovskites, respectively. Potential at GB is higher compared to the grain interior. AFM topography (h, j) for reference sample as highly oriented pyrolytic graphite (HOPG) before and after KPFM measurement for perovskite samples, respectively and their corresponding surface potential images (i, k) [52].

Space charge layer (SCL) width ($W_{GB}$) is estimated as the distance between the left and right edges [shown in Fig. 4.1e (i)]. Likewise, Fig. 4.1e (iv-vi) show the $SP_{x_i}$ profiles of three different areas of the FAMACs perovskite film. Table 4.1 shows the estimated $\Delta\varphi_{GB}$ at three different GB areas for $MAPbI_3$ and FAMACs perovskite films, respectively. The average of GB potential barrier decreased from ~28.30 meV for $MAPbI_3$ perovskite (Table 4.1) to ~13.30 meV for FAMACs perovskite (Table 4.1).

Table 4.1 Density of defects and trap states for $MAPbI_3$ and FAMACs perovskite with grain and grain boundary parameters

| $MAPbI_3$ | | | | FAMACs | | | |
|---|---|---|---|---|---|---|---|
| Three Random GB Areas | GB potential barrier, $\Delta\varphi_{GB}$ (meV) | Net doping, $P_{net}$ ($cm^{-3}$) | Density of trap states at GB, $P_{GB\text{-}trap}$ ($cm^{-2}$) | Three Random GB Areas | GB potential barrier, $\Delta\varphi_{GB}$ (meV) | Net doping , $P_{net}$ ($cm^{-3}$) | Density of trap states at GB, $P_{GB\text{-}trap}$ ($cm^{-2}$) |
| 1 | 27 | $7.81\times10^{15}$ | $15.0\times10^{10}$ | 1 | 15 | $3.99\times10^{15}$ | $7.99\times10^{10}$ |
| 2 | 30 | $1.31\times10^{16}$ | $20.5\times10^{10}$ | 2 | 13 | $4.28\times10^{15}$ | $3.85\times10^{10}$ |
| 3 | 28 | $6.17\times10^{15}$ | $13.6\times10^{10}$ | 3 | 12 | $3.61\times10^{15}$ | $7.07\times10^{10}$ |
| Statistical Calculation | 28.33±1.57 | (9.03±3.62) $\times10^{15}$ | (16.4±0.36) $\times10^{10}$ | Statistical Calculation | 13.33±1.53 | (3.96±0.34) $\times10^{15}$ | (6.30±2.17) $\times10^{10}$ |

The reduced average GB potential barrier suggests a more efficient charge transport between the grains in the FAMACs perovskite film. Charge carrier trapping at GBs significantly affects the electrical transport properties of perovskite films. Large number of

defects at GBs creates immobilized trap states. These trap states trap free carriers and become electrically charged. Motion of the charge carriers is impeded at the GBs due to the potential energy barrier created by these electrically charged defect states. The charge carrier concentration at GBs can be calculated from the SP images acquired using KPFM [58, 84]. As the GBs of perovskite can be electrically charged, therefore the net doping density of perovskite can be calculated from the barrier height of band bending and the width of the GBs [58]. The net doping ($P_{net}$) and density of trap states at GB ($P_{GB\text{-}trap}$) are calculated from the following equations [84-86]

The calculated values of $P_{net}$ and $P_{GB\text{-}trap}$ at three different GB areas for $MAPbI_3$ and FAMACs perovskite film were are summarized in Table 4.1. $MAPbI_3$ exhibited $P_{net}$ and $P_{GB\text{-}trap}$ of $9.03\times10^{15}/cm^3$ and $16.4\times10^{10}/cm^2$, respectively versus FAMACs with $3.96\times10^{15}/cm^3$ and $6.30\times10^{10}/cm^2$. These values from our experiment are in good agreement with reported literatures [91-97]. In the literature of Perovskite solar cells, there are many reports showing the differences of surface potential between the control and treated samples are ~10 meV by comparing their profile lines [41, 98, 99]. Such surface potential difference is small but did cause difference in device performance. Our measurements were based on the average surface potential for various locations with many profile lines on the perovskite films.

The density of trap states at grain boundaries ($P_{GB\text{-}trap}$) can be calculated from the SP images acquired using KPFM [84]. Density of trap states at grain boundaries in $MAPbI_3$ and FAMACs perovskites calculated are in the order of $10^{11}$ per $cm^2$ which are in the similar order calculated for polycrystalline material at the grain boundaries [84, 100]. Therefore, extracted density of trap states at GB is not low but similar to other polycrystalline

materials [84, 100]. For this type of density trap states calculation at grain boundaries by KPFM, it is assumed that grain boundary corresponds to surface with a surface charge [84]. This assumption also led to calculate the net doping/ defect density in the bulk of the active material. The net doping ($P_{net}$) calculated in our work are in the order of $10^{15}$ per $cm^3$ which is like the values calculated in other reports for polycrystalline perovskites. The approach followed in this work (KPFM) allows to calculate the trap density at grain boundaries only. The occurrence of potential change at grain boundaries compared with grain interiors in surface potential images (Figure 4.1e) is what enables us to calculate the trap density values at grain boundaries and not at the grain interiors. The work function of the tip was measured before and after KPFM measurements on $MAPbI_3$ and FAMACs perovskites using the standard highly oriented pyrolytic graphite (HOPG) reference samples. It validates that whether KPFM measurements are consistent or whether the tip properties alter during KPFM measurements for $MAPbI_3$ and FAMACs perovskites. The HOPG work function is ~4.60 eV [101]. Fig. 4.1 h and j show the topography of standard HOPG reference sample via the same tip that was used before and after the measurements on both $MAPbI_3$ and FAMACs perovskites, respectively. The average CPD of HOPG sample before (Figure 4.1i) and after (Figure 4.1k) KPFM measurements of perovskites was around ~-0.174 V and -0.175 V, respectively. Therefore, the work function of the tip was ~4.774 eV and ~4.775 eV for beforehand and later KPFM measurements, respectively. The variation of tip work function before and after KPFM measurements on perovskites is only 1 meV. This suggested that the tip properties may not alter much for the duration of the measurements when changing samples or sample locations in between. The lower $\Delta\varphi_{GB}$, $P_{net}$, and $P_{GB\text{-}trap}$ perovskite suggests efficient charge transport between the grains in FAMACs perovskite

film. Figure 4.1.1 shows another set of SP image for $MAPbI_3$ and FAMACs perovskites and their respective line profile at GB. The reduced average GB potential barrier suggests a efficient charge transport between the grains in the FAMACs perovskite film compared to $MAPbI_3$.

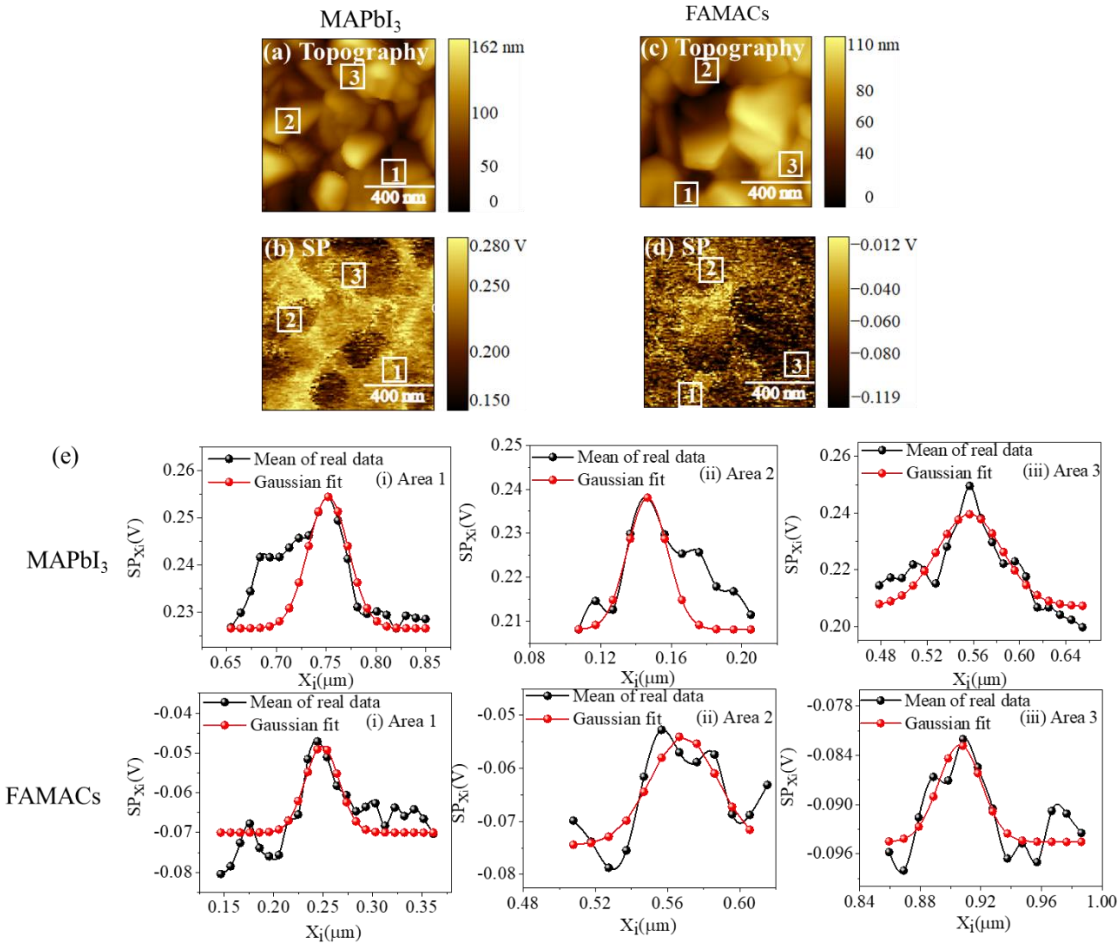


Figure 4.1.1 AFM topography images for (a) $MAPbI_3$ and (c) FAMACs perovskite, respectively and their corresponding surface potential images (b, d). Average surface potential profiles at $x_i$ [e (i-iii) and e (iv-vi)] of 3 different areas (marked in topography and SP images) for $MAPbI_3$ and FAMACs perovskites, respectively. Potential at GB is greater compared to the grain interior.

KPFM studies show that potential at GBs is higher compared to grain in both $MAPbI_3$ and FAMACs perovskites. The increase in potential barrier for electrons (upward band bending) is due to the accumulation of negatively charged defects at GBs [58, 102, 103]. The negatively charged defects in $MAPbI_3$ are mostly $V_{MA}$ and $I_i$ because of a smaller amount of ion formation energy [53]. Hence, $V_{MA}$ and $I_i$ have the bias to gather at GBs and therefore large accumulation of these defects enhance the GB potential barrier ($\Delta\varphi_{GB}$). Figure 4.1f and 4.1g show the electronic band structures at GBs of both perovskites. It makes barrier for electrons and accumulate the holes which eventually get lost by recombination. In contrast, $I_i$ defects are reduced in FAMACs as bromide ion faces difficulty in movement due to high formation energy [60]. In supplement, $V_{FA}$ defects formation can be inhibited in mixed cation structure (FAMACs) as formation energies enhanced upon mixing of anions and cations [60]. As a result, fewer defects are accumulated at GBs and lowered $\Delta\varphi_{GB}$ is seen for FAMACs perovskites.

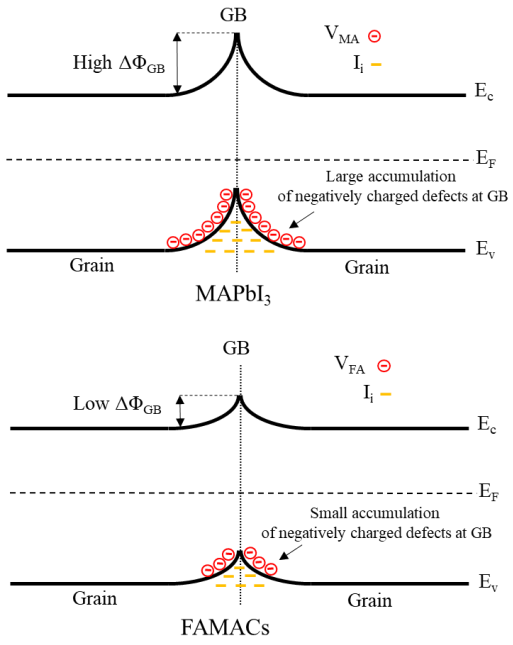


Figure 4.2 Electronic band structure at GBs for (f) $MAPbI_3$ and (g) FAMACs perovskites.

### 4.1.2 Defect Ion Migration in Perovskites: Hysteresis Effects

Presence of the point defects across perovskite GB are very much vulnerable to defect ion migration which results in hysteresis in the current voltage curves. For more detailed analysis of the movement of the point defects at GB region of $MAPbI_3$ and FAMACs perovskite, local dark current hysteresis was measured using conductive atomic force microscopy (c-AFM). A significant current hysteresis would indicate a faster ion migration while opposite would say slower ion migration [46]. Figure 4.3a and b show 400 nm × 400 nm AFM surface pictures of $MAPbI_3$ and FAMACs perovskite films, respectively. The places where C-AFM tip was positioned to determine dark current hysteresis are categorized with blue color (at GB), green color (in 15 nm of GB), and orange color (in 15 nm of GB) plus (+) marks. The AFM tip voltage bias was in the range between 1.0 V and -1.0 V in forward and reverse scan with a scan rate of 0.14 $Vs^{-1}$. As shown in Fig. 4.3c, e and g, the dark-current at GB of $MAPbI_3$ and in 15 nm area surrounding of GB demonstrate significant hysteresis. Oppositely, the assessed dark current for FAMACs perovskite shows minor hysteresis (Figure 4.3d, e and f). This inspection indicates that the defects ions are more spontaneously roaming at GB region of $MAPbI_3$ than FAMACs which leads to improved performance of the latter one. As point defect ions have a tendency to gather at the GB of the perovskite material, there is a likelihood that GBs are dictated by defect ion migration and outcomes in significant current voltage hysteresis. At GB, current voltage curve in both in forward and reverse scan direction shows clear hysteresis. However, FAMACs does not show hysteresis in current voltage curve in both in forward and reverse scan direction. This undoubtedly demonstrates that all the defect ions present in $MAPbI_3$ perovskites gather at the GB and travel nearby the GB area.

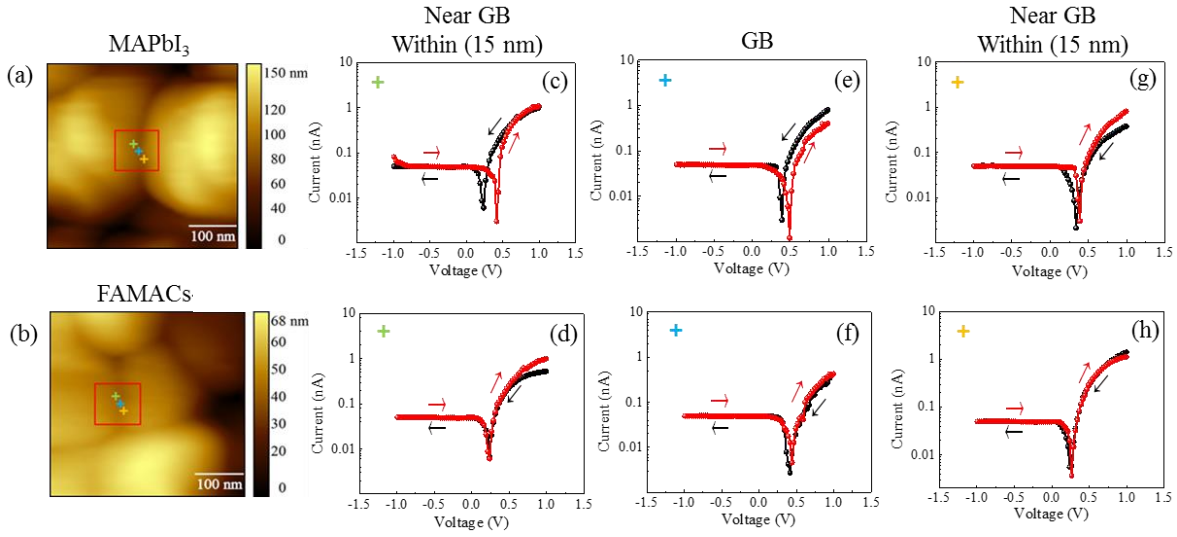


Figure 4.3 Contact mode AFM images of (a) $MAPbI_3$ and (b) FAMACs perovskite films, respectively. The places where C-AFM tip was positioned to assess dark current are categorized with blue, green, and yellow color signs. Local forward and reverse dark current measured at left side of GB in 15 nm (c, d), at GB (e, f) and right side of GB in 15 nm (g, h), showing insignificant hysteresis at GB region for FAMACs over $MAPbI_3$.

## 4.2 Nanoscale Investigation of GB Passivation in FAMACs Perovskites

GB defects passivation has been investigated through nanoscale mapping of charge carrier dynamics, KPFM and CAFM in FAMACs perovskite post-treated by PHI salt (phenylhydrazinium iodide-$C_6H_5NHNH_3I$). Optimal amount of PHI was seen to passivate the defects at the grain boundaries and suppress charge recombination which results in better recombination lifetime, transport time and diffusion length in post treated FAMACs perovskites compared to untreated perovskite. The visual mappings can basically help to

distinguish the physical areas on the perovskite films which has better charge carrier dynamics from that which do not. Defects analysis and passivation at GB of FAMACs perovskite by nanoscale mapping, KPFM and CAFM demonstrate that optimized concentration of PHI can passivates the positively charged defects and significantly improves charge carrier dynamics at GB compared to control sample.

### 4.2.1 GB Passivation of FAMACs Perovskites Using Phenylhydrazinium Iodide (PHI)

Perovskites GB often contains different types of point defects that can cause the charges to be trapped and results in recombination via those defects. Due to low defect formation energy, charged defects are expected to form in perovskites, including under-coordinated $Pb^{2+}$ defects [18, 104, 105] and iodide vacancies [57, 106]. These defects are more likely to be present at GB that act as recombination centers for photogenerated charge carriers [18, 107, 108]. Cross-sectional scanning electron microscopy (SEM) image (Figure 4.4a) of the perovskite device shows that thickness of perovskite active layer is ~ 0.50 µm. Different PHI concentrations were used to fabricate a thin passivation layer on the top of FAMACs (control) perovskite to study the GB passivation. The studied concentrations of PHI are 1mg/mL PHI (PHI-1), 2mg/mL PHI (PHI-2) and 3mg/mL PHI (PHI-3). Figure 4.4 shows the (a) Cross sectional SEM image of the complete device, PHI used for the post-treatment of the perovskite samples, (b) Molecular structure of PHI and (c) 3D structure of PHI. PHI contains amines rich with lone pair electrons which can be donated to the under-coordinated $Pb^{2+}$ to form a coordination bond. Thus, PHI effectively passivates the GB defects in perovskites solar cells.

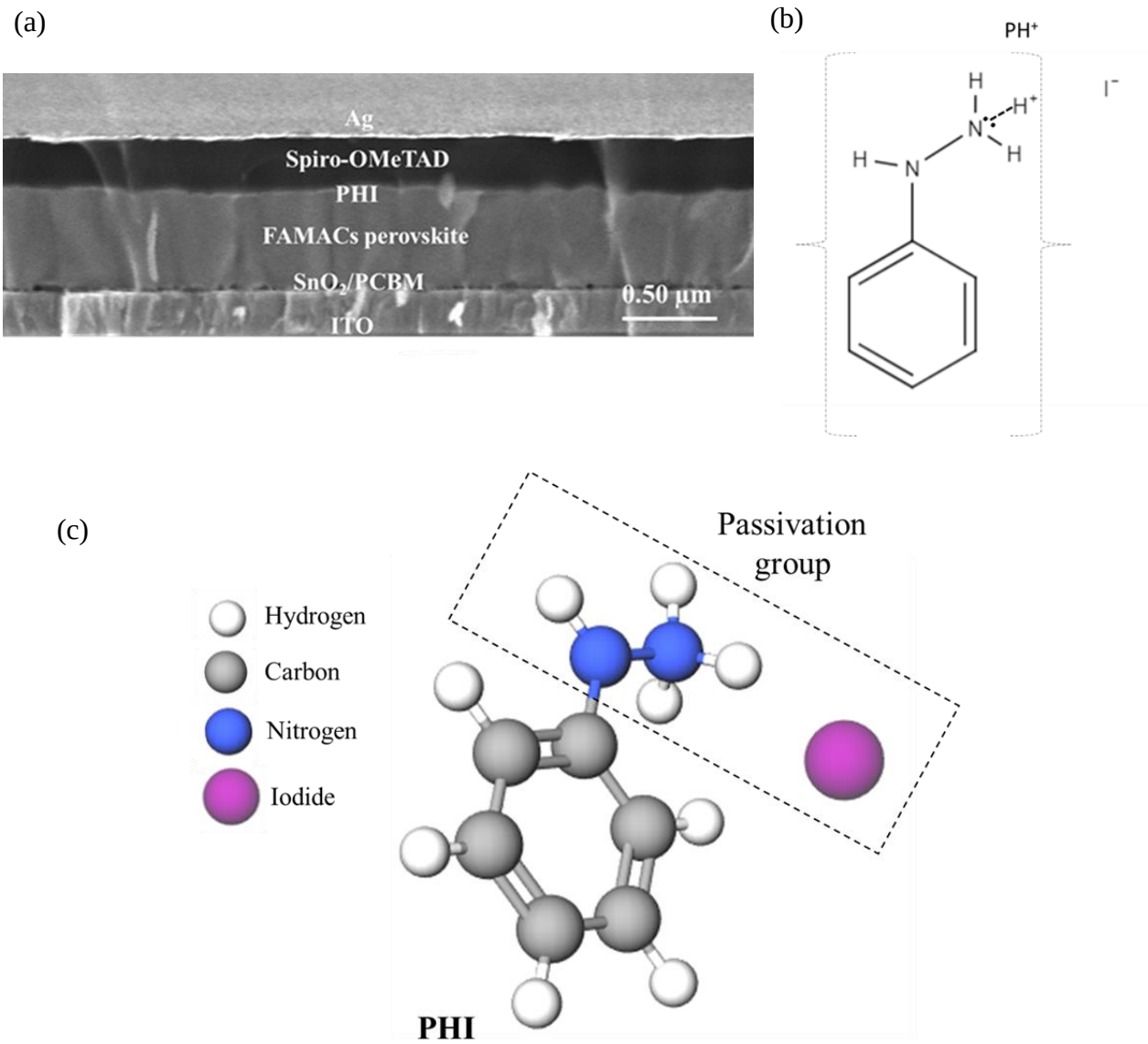


Figure 4.4 (a) Cross sectional SEM image of the complete device. PHI used for the post-treatment of the perovskite samples, (b) Molecular structure and (c) 3D structure.

The cross-sectional scanning electron microscopy (SEM) images (Figure 4.4a) show that GBs mostly exist along the vertical direction. Therefore, movement of the charge carrier inside the GI would not come across GB and vice versa. During the annealing process,

$A^+$([FAMACs]$^+$) cations and $X^-$($I^-$, $Br^-$) anions from perovskite molecule can be lost and thus resulting under-coordinated $Pb^{2+}$ defects [18]. PHI contains amines rich with lone pair electrons (Figure 4.4b and c) which can be donated to the under-coordinated $Pb^{2+}$ to form a coordination bond [109, 110].

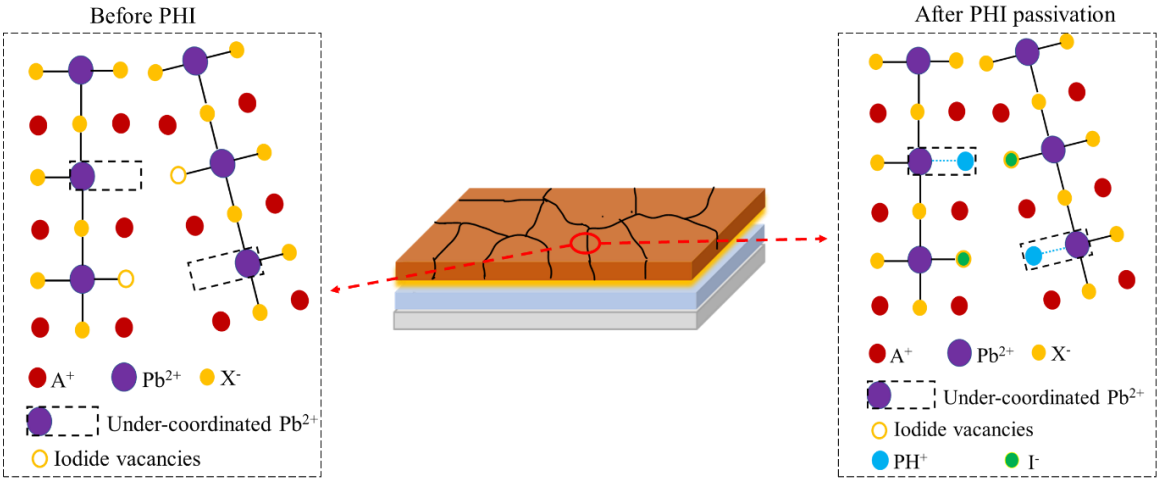


Figure 4.5 Schematic of the GB passivation process by PHI illustrating the passivation of charged defects: where $A^+$=(FAMACs)$^+$ and $X^-$=$I^-$, $Br^-$.

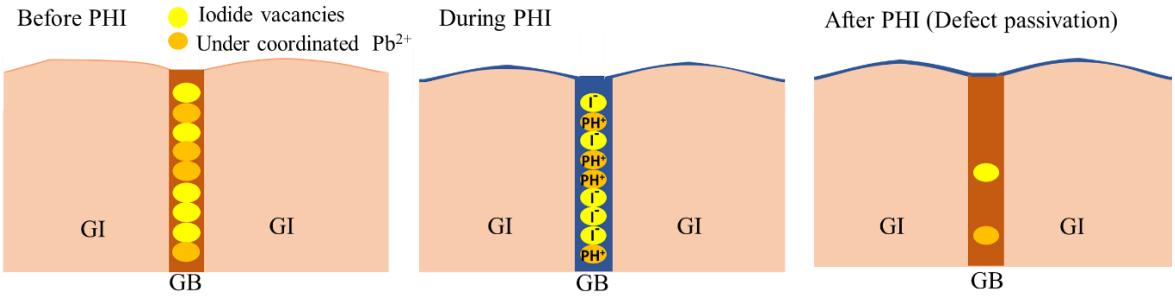


Figure 4.6 Schematic of the GB passivation process by PHI illustrating the reduction of charged defects.

Furthermore, iodide ions from the PHI coating can fill the iodide vacancies at GB [6]. Thus, the PHI can effectively passivate two major point defects (under-coordinated $Pb^{2+}$ defects

and iodide vacancies) of perovskites. A schematic of this GB passivation process by PHI has been presented in Fig. 4.5 and Fig. 4.6.

Figure 4.7a shows the ultraviolet-visible (UV-Vis) absorption spectra of FAMACs perovskite with and without PHI. The perovskite films have the characteristic broad absorption across visible and near-infrared region with the optical bandgap of ~1.58 eV. Figure 4.7a shows the photoluminescence (PL) spectrum of FAMACs perovskite with and without PHI. All the peaks are obtained at around 781 nm emission wavelength with excitation wavelength applied at 395 nm. PL intensities increased after PHI treatment which indicates that the recombination in the perovskite has been greatly suppressed.

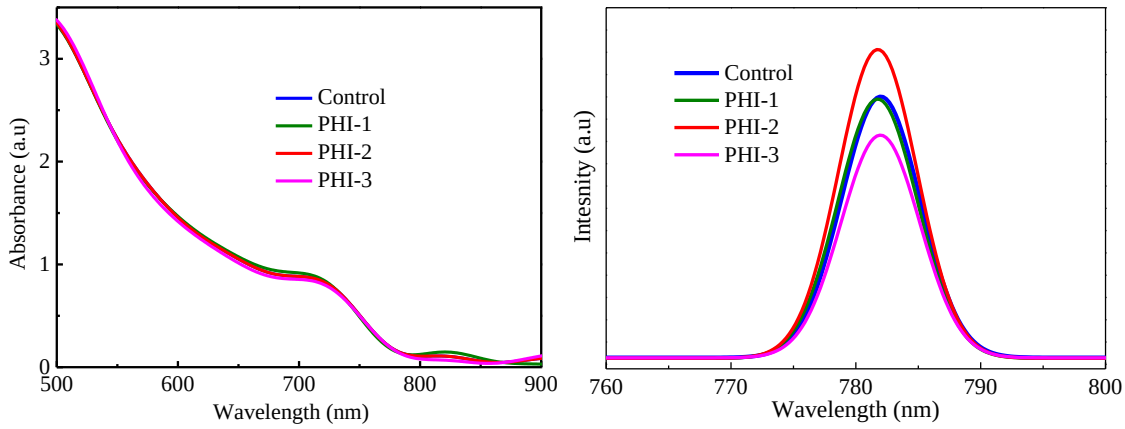


Figure 4.7 Perovskite film characterization (a) UV-Vis and (b) Photoluminescence (PL) spectrum.

Figure 4.7.1 shows the Xray diffraction (XRD) of PHI powder, FAMACs perovskite with and without PHI. A small PHI peak can be observed as marker with asterisk (*) in the respective XRD images of PHI-1, PHI-2 and PHI-3 perovskites. It is corresponding to PHI

powder peak as shown in the Fig. 4.7.1. The dominant perovskite (PVK) has also been shown at ~14.8 degree. The presence of the peak at different concentration of PHI in perovskite corresponding to PHI powder peak prove that there is PHI in all the studied perovskites.

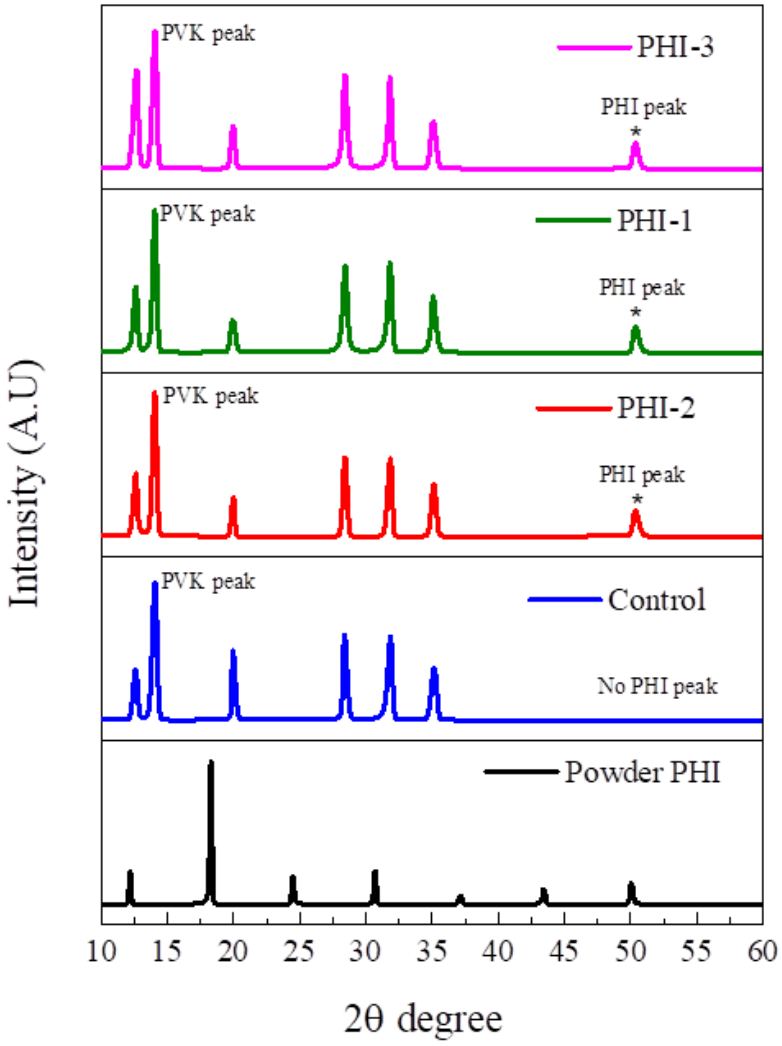


Figure 4.7.1 Xray diffraction (XRD) of PHI powder, perovskite film with different concentration of PHI solution.

4.2.2 Grain Boundary Passivation Analysis by AFM Instrumentation

Different PHI concentrations were used to fabricate a thin passivation layer on the top of FAMACs (control) perovskite to study the GB passivation. The studied concentrations of PHI are 1mg/mL PHI (PHI-1), 2mg/mL PHI (PHI-2) and 3mg/mL PHI (PHI-3). Figure 4.8 shows 800 nm × 800 nm contact mode AFM topography images of control, PHI-2, PHI-1 and PHI-3 perovskites. A 100 nm × 100 nm area (indicated by the red square) on the topography image that includes GB was selected randomly for the nanoscale charge dynamics mapping. A longer $\tau_r$ is indicative of improved local charge carrier recombination lifetime.

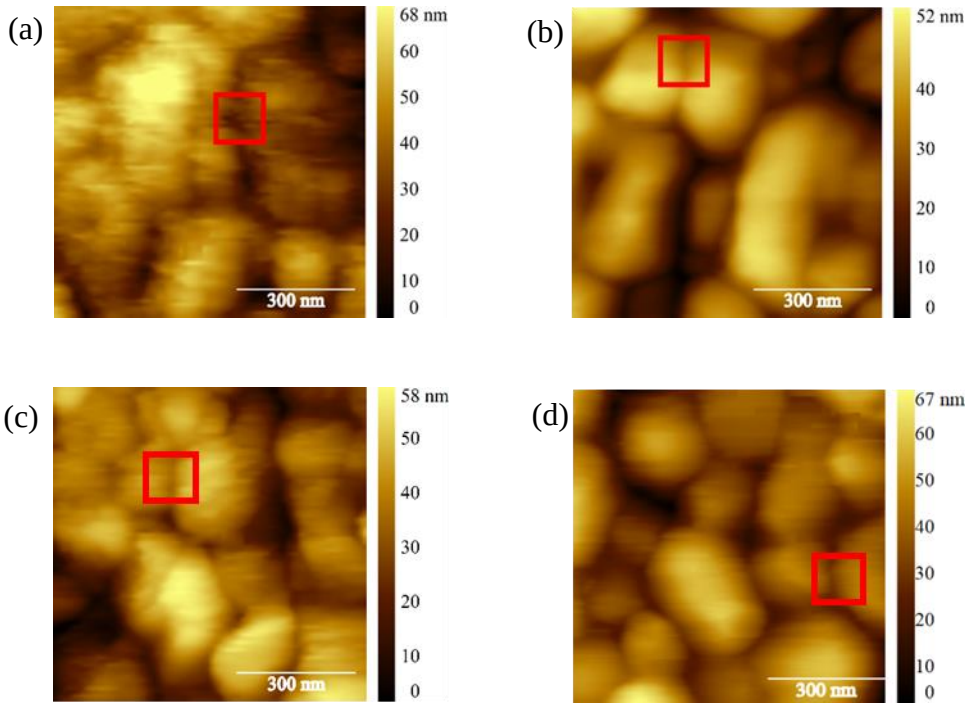


Figure 4.8 Contact mode AFM topography of (a) control, (b) PHI-2, (c) PHI-1 and (d) PHI-3 perovskite films. Red square (100 nm × 100 nm) indicates the area where LT-AFM resolved mapping was conducted on the perovskites.

Figure 4.9a shows a typical TPV decay curve for FAMACs perovskite obtained through our LT-AFM. Eq. (1) was used to fit the TPV decay which resulted in a $\tau_r$ of 11.86 µs. Similarly, nanoscale $\tau_r$ mappings were obtained by fitting the 4096 TPV data with Eq. (1). TPV decay were well fitted mono exponential decay function instead of a double exponential function which suggests that only a single recombination mechanism contributes to the time constants and governs the entire recombination processes. This single recombination process can be ascribed to non-radiative recombination lifetime [63-65]. Figure 4.9b shows a characteristic TPC decay curve for FAMACs perovskite acquired through our LT-AFM. Eq. (2) was used to fit the TPC decay which lead to a $\tau_t$ of 6.50 µs. Likewise, nanoscale $\tau_t$ mappings were acquired by fitting the 4096 TPC data with Eq. (2). Similarly, in our experiment, recombination of excess charge carriers due to light perturbation follows the exponential decay (Figure 4.9) which gives the corresponding recombination lifetime. Similarly, TPC analysis follows the above concept of fitting with exponential decay. However, TPV/TPC in our experiment were measured directly from perovskite with metal AFM tip (ITO /ETL / Perovskite / tip metal electrode) as the electrode (half-cell configuration). It could convolve extrinsic effects such as charge transfer at the tip-sample junction that might cause to higher value of the time constant (Figure 4.9) [56]. It is more appropriate to explicitly state that this is the apparent recombination lifetime and transport time measured with metal (AFM tip)-perovskite interface, which is relevant to the actual device configuration [56].

AFM artifacts related to surface topography can be caused due to the coarse tip (large tip radius), fast scanning of the sample, rough material surface etc. and our measurements were focused on minimization of its effect to the lowest. For this, in our setup, we used a

sophisticated AFM tip that facilitates a high spatial resolution of ~10 nm. Such resolution could effectively mitigate the topographic artifacts. Further, we scanned the samples slowly (.25 lines/sec) while measuring the topography so that topographic artifacts could be minimized. After the topography measurement, we selected a 100nm × 100nm area for the nanoscale mapping. We optimized different measurement parameters like bias voltage, position of the illumination source and time of scan at each pixel so that the TPV and TPC signals obtained have negligible dependence on AFM-measurement artifacts such as grain-boundary grooving. TPV signals (Figure 4.9) of both the perovskites are well-shaped and suitably fitted with mono-exponential decay function that gives the carrier recombination lifetime. Therefore, we believe, AFM-measurement artifacts are reasonably mitigated in our setup.

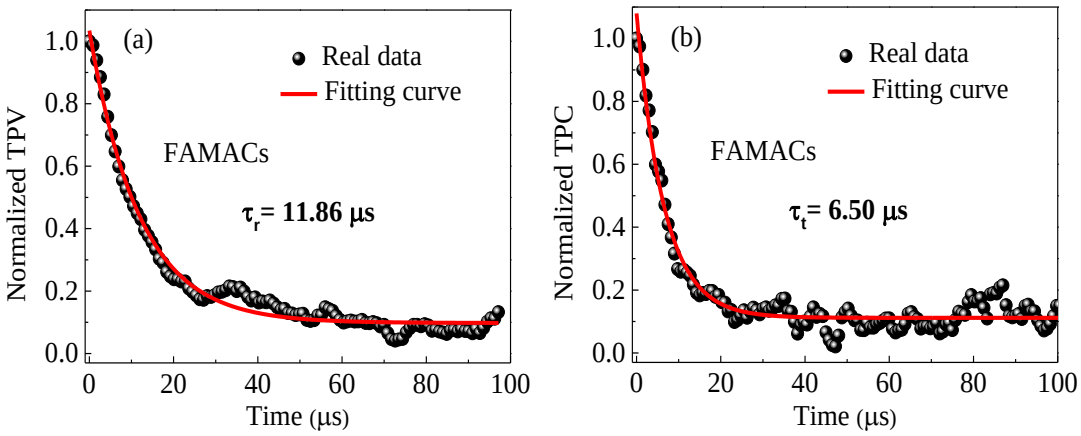


Figure 4.9 Transient decay of control FAMACs perovskite (a) TPV and (b) TPC with the corresponding fitted curves using mono exponential decay function.

Figure 4.9 shows a typical TPV and TPC decay curve for FAMACs perovskite obtained through our LT-AFM. Equation 3.1 and 3.2 were used to fit the TPV and TPC decay, respectively. Thus, obtained TPV and TPC decays are used to obtain the apparent recombination lifetime and transport time of the perovskites.

### 4.2.3 Visualization of Grain Boundary Passivation Via Mapping of Apparent Recombination Lifetime

Figure 4.10, a to d show the nanoscale $\tau_r$ mapping of control, PHI-2, PHI-1 and PHI-3 perovskites respectively at similar regions indicated by red squares. Red square indicated in the topography images was selected for the mapping. White dashed lines in the mapping show the GB. The recombination lifetime was improved in both GI and GB for PHI-2 perovskites compared with the control sample. The average of $\tau_r$ at GB is 11.89 µs for PHI-2 perovskites which is longer than the control sample (10.71 µs). Pie chart of the lifetime (Figure 4.11) at GB reveals that ~39% of $\tau_r$ occurs in shorter lifetime (<11.5 µs) in PHI-2 perovskite, which is ~71% for the control. Figure 4.10e shows the average line profile of $\tau_r$ along GI-GB-GI obtained from the mapping images (Figure 4.10a-d). The recombination lifetime in PHI-2 perovskites within GI was ~13.90 µs, whereas it reduces to ~13.30 µs in the control sample (Figure 4.10e). Figure 4.10f shows the $\tau_r$ difference between GI and GB of control and all studied PHI concentration perovskites obtained from the average line profile (Figure 4.10e). Lower difference between GI and GB implies enhanced recombination lifetime. The control resulted in a large difference of ~3.70 µs between GI and GB. This difference was reduced to ~3.10 µs and ~3 µs for PHI-1 and PHI-3 perovskites, respectively. While PHI-2 perovskites resulted in the least difference of ~2.40 µs. This further suggests passivation of the grain boundaries. The decay curves of the transients are well described by a single exponential function instead of a double exponential function (Figure 4.9). GB passivation by PHI also improves the charge carrier dynamics at GI (Table 4.2). The mean of charge carrier lifetime is longer at GI ($\tau_r$ = 13.69 µs) in the PHI-2 sample than that at control sample ($\tau_r$ = 13.19 µs). The mean of charge

carrier lifetimes at GI for PHI-1 and PHI-3 perovskites are 13.51 and 13.12 μs, respectively. We infer that, PHI coating on the perovskite layer improves the charge carrier recombination lifetime at GI by passivating both surface and GB defects.

Recombination lifetime in perovskite solar cells typically are of wide ranging and could be similar of ~10 us or longer [6, 75, 111-113]. Usually the recombination lifetime in perovskite solar cell is measured in a full cell/ device configuration (ITO /ETL / Perovskite / HTL /metal electrode). However, in our experiment, it was measured directly from perovskite with metal AFM tip (ITO /ETL / Perovskite / tip metal electrode) as the electrode (half-cell configuration). It could convolve extrinsic effects such as charge transfer at the tip-sample junction that might cause to higher value of the recombination time. It is more appropriate to explicitly state that this is the apparent recombination lifetime measured with metal (AFM tip)-perovskite interface, which is relevant to the actual device configuration [56]. Measured values of apparent charge recombination lifetime are consistent with other reports on the perovskite films [56, 75, 111-114]. This suggests only one recombination mechanism contributing to the time constants and dominates the entire recombination processes. We attribute this single recombination process to non-radiative recombination lifetime [63, 64]. The observed longer charge carrier lifetime in the treated perovskite indicates that the trap assisted recombination is less at GB of PHI-2 perovskite compared with the control sample. Also, the observed longer charge carrier lifetime in the treated perovskite indicates that the trap assisted recombination is less at GB of PHI-1 and PHI-3 perovskites compared with the control sample. Thus, the PHI can effectively passivate two major point defects (under-coordinated $Pb^{2+}$ defects and iodide vacancies) of perovskites.

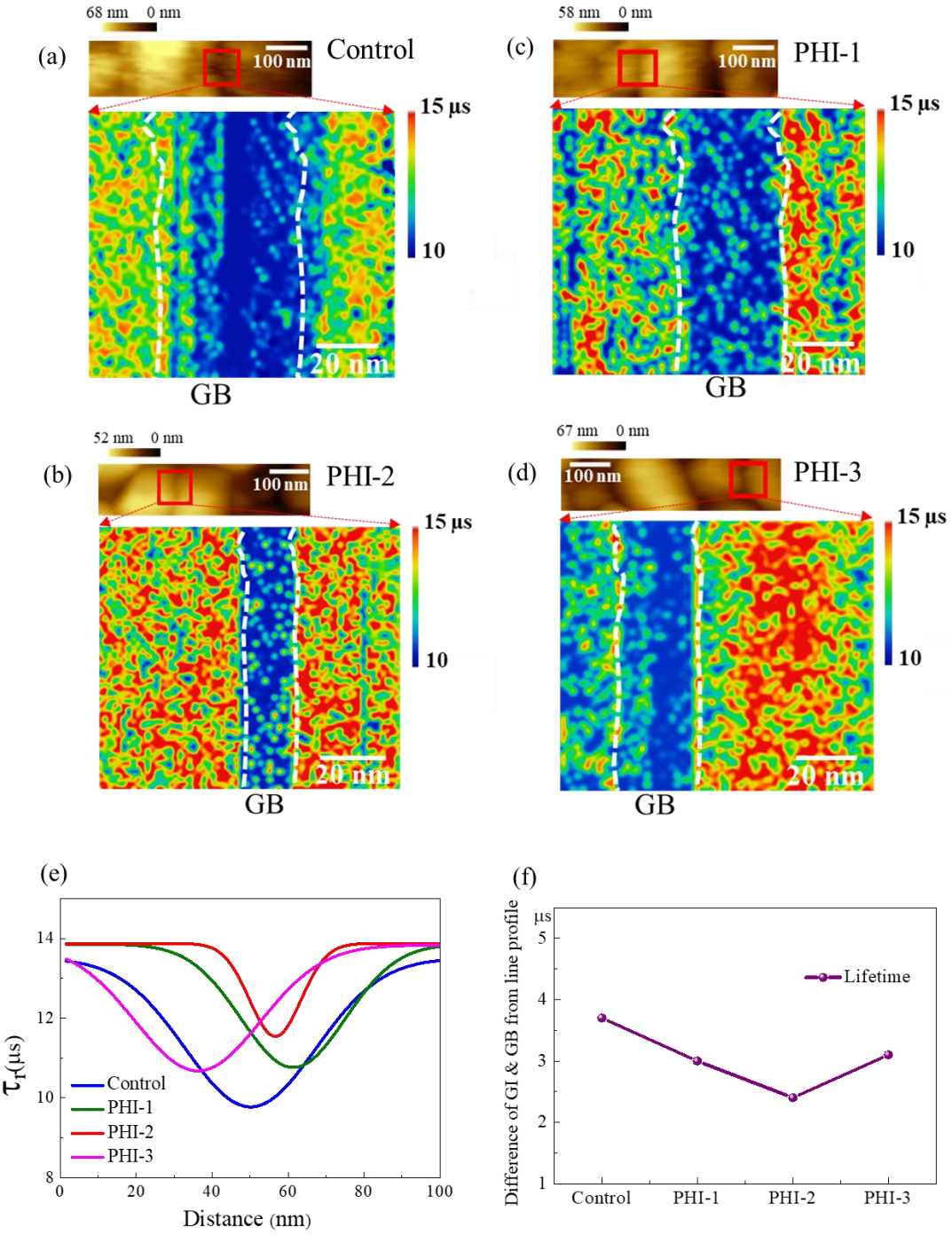


Figure 4.10 LT-AFM resolved mapping (100 nm × 100 nm) of $\tau_r$ (charge carrier lifetime) for (a) control, (b) PHI-2, (c) PHI-1 and (d) PHI-3 perovskites, respectively. (e) Average line profile of $\tau_r$ along GI-GB-GI obtained from Fig. a-d. (f) Difference of GI and GB from line profile vs concentration of PHI solution.

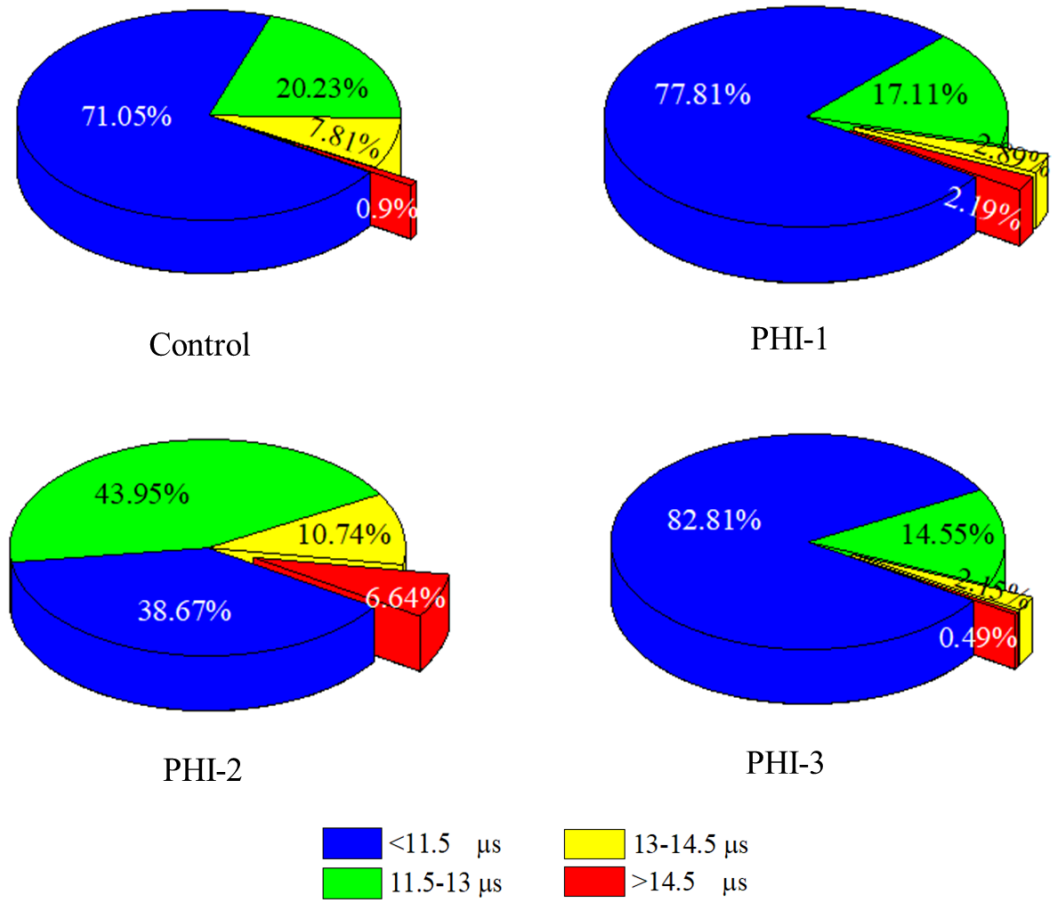


Figure 4.11 Pie chart distribution of apparent recombination lifetime at GB.

4.2.2.2 Visualization of Grain Boundary Passivation Via Mapping of Apparent Transport Time

Figure 4.12, a to d show the nanoscale $\tau_t$ mapping of control, PHI-2, PHI-1 and PHI-3 perovskites respectively at similar regions indicated by red squares. A shorter $\tau_t$ would indicate improved local charge carrier transport time. GI and GB show better transport time for PHI-2 perovskites compared with control sample. The average of $\tau_t$ at GB for PHI-2 perovskites (7.64 μs) is shorter than control sample (8.95 μs). At GB, only ~6% of τt falls in longer transport time (> 9.5 μs) in PHI-2 perovskite, while ~45% of $\tau_t$

was found to be longer than 9.5 μs for the control sample (Figure 4.13). From the average line profile of $\tau_t$ along GI-GB-GI, transport time in PHI-2 perovskites within GI was ~6.10 μs, whereas it increases to ~6.35 μs in control sample (Figure 4.12e). The control resulted in a difference of ~3μs between GI and GB (Figure 4.12f) which is higher than PHI-2 perovskites with ~1.80 μs. PHI-1 and PHI-3 perovskites show ~2.40 μs and ~2.35 μs, respectively. The least change between GI and GB for PHI-2 perovskites is indicative of an effective passivation of the defects at grain boundaries. In the GI, the mean of charge carrier transport time ($\tau_t$) for PHI-2 sample is 6.16 μs which is also shorter than that (6.86 μs) in the control sample. In the GI, the mean of charge carrier transport time ($\tau_t$) for PHI-1 is 6.95 μs whereas for PHI-3 is 6.36 μs. We infer that, PHI coating on the perovskite layer improves the charge carrier transport time at GI by passivating both surface and GB defects. Measured values of apparent charge transport time are consistent with other reports on the perovskite films [75, 111-114]. As our setup is measuring time constants at metal AFM tip and perovskite interface, it is more appropriate to explicitly state that this is the apparent recombination lifetime and transport time measured with metal (AFM tip)-perovskite interface, which is relevant to the actual device configuration. [56].

Measured values of apparent charge transport time are consistent with other reports on the perovskite films [56, 75, 111-114]. This suggests only one recombination mechanism contributing to the time constants and dominates the entire recombination processes. We attribute this single recombination process to non-radiative recombination [63, 64].

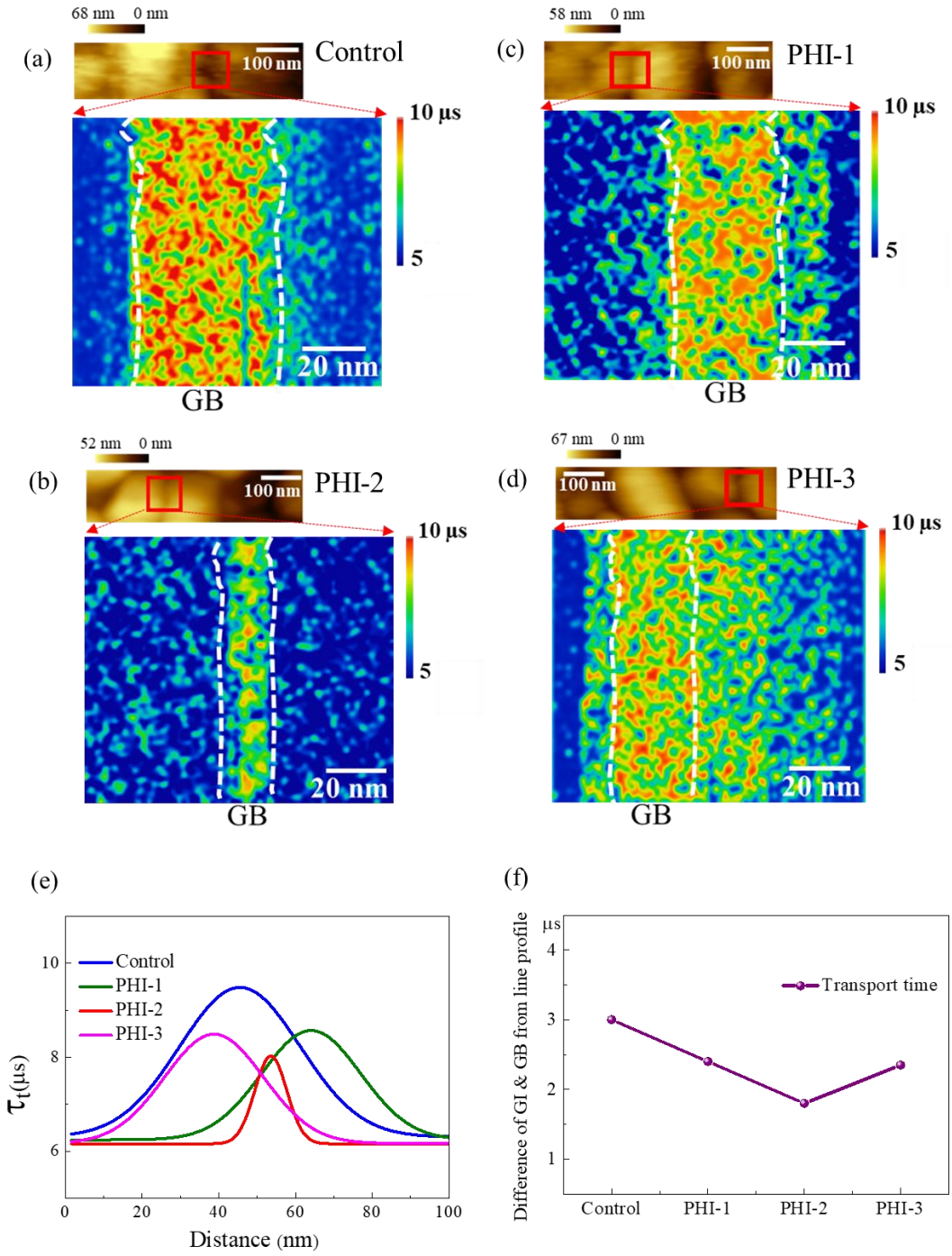


Figure 4.12 LT-AFM resolved mapping (100 nm × 100 nm) of $\tau_t$ (charge carrier transport time) for (a) control, (b) PHI-2, (c) PHI-1 and (d) PHI-3 perovskites, respectively. (e) Average line profile of $\tau_t$ along GI-GB-GI obtained from Fig. a-d. (f) Difference of GI and GB from line profile vs concentration of PHI solution.

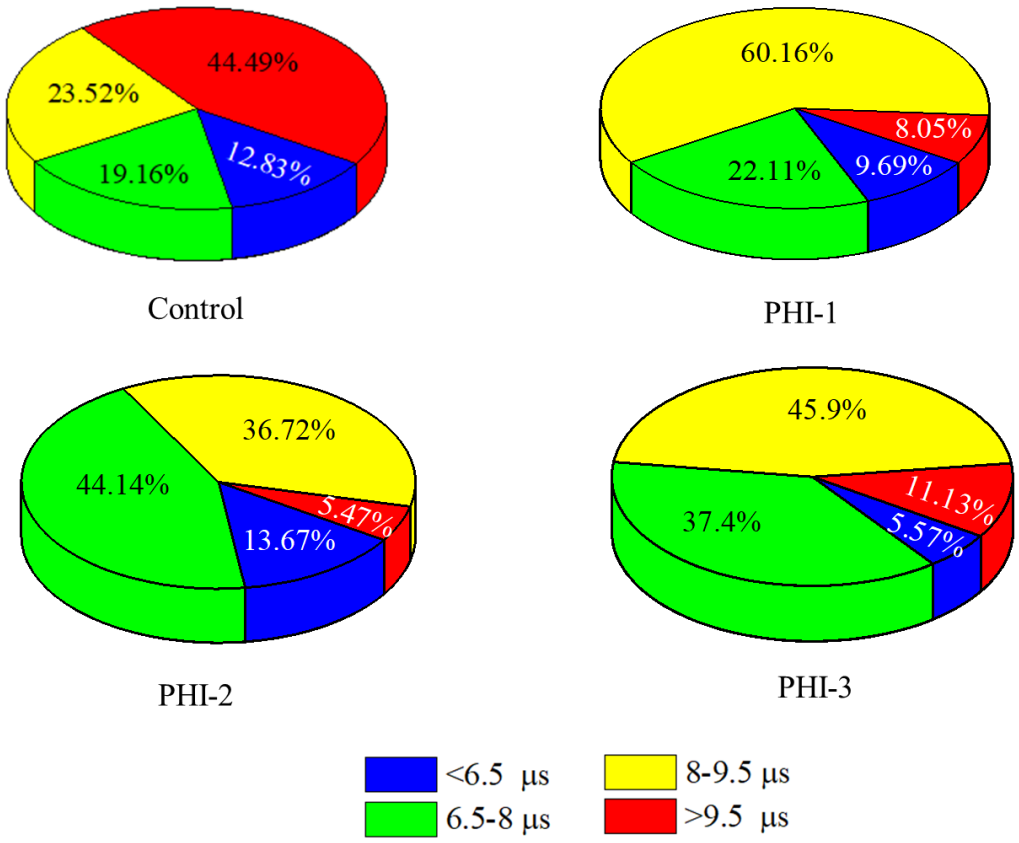


Figure 4.13 Pie chart distribution of apparent transport time at GB

4.2.2.3 Visualization of Grain Boundary Passivation Via Mapping of Apparent Diffusion Length

Figure 4.14, a to d show the nanoscale $L_D$ mapping of control, PHI-2, PHI-1 and PHI-3 perovskites respectively at similar regions (indicated by red squares). A longer $L_D$ is indicative of enhanced local charge carrier diffusion length. The diffusion length shows the best improvement in GI and GB for PHI-2 perovskites compared with the control sample. The average of $L_D$ at GB is 0.40 µm for PHI-2 perovskites which is longer than control sample with 0.36 µm. Average line profile of $L_D$ (Figure 4.14e) along GI-GB-GI was obtained from the diffusion length mappings (Figure 4.14 a-d). The diffusion length

in PHI-2 perovskites within GI was ~0.50 µm, while decreases to ~0.46 µm in the control (Figure 4.14e). Figure 4.14f shows the diffusion length difference between GI and GB of the control and treated perovskites with different PHI concentration obtained from the average line profile (Figure 4.14e). Lower difference between GI and GB implies enhanced diffusion length. The PHI-2 perovskites show the least difference of ~0.11 µm while ~0.125 µm and ~0.13 µm for PHI-1 and PHI-3 perovskites, respectively. Similarly, the pie chart (Figure 4.15) at GB shows ~17% of $L_D$ falls in shorter diffusion length (<0.35 µm) in PHI-2 perovskite, whereas only ~74% of $L_D$ was shorter than 0.35 µm for the control. The control resulted in the highest difference of ~0.15 µm. This increased diffusion length with PHI suggests effectual passivation of the grain boundaries in the perovskite. Furthermore, the overall mean of diffusion length at GI ($L_D$=0.50 µm) for the PHI-2 perovskite is also longer than that ($L_D$=0.46 µm) in the control sample. The overall mean of diffusion length at GI for the PHI-1($L_D$=0.47 µm) is alike to that of PHI-3 perovskite ($L_D$=0.475 µm). We infer that, PHI coating on the perovskite layer improves the diffusion length at GI by passivating both surface and GB defects, The values of diffusion length observed in our study are well within the range of the reported works [83, 115-121]. The observed longer charge carrier diffusion length in the treated perovskite indicates that the trap assisted recombination is less at GB of PHI-2 perovskite compared with the control sample. PHI contains amines rich with lone pair electrons which can be donated to the under-coordinated $Pb^{2+}$ to form a coordination bond. Furthermore, iodide ions from the PHI coating can fill the iodide vacancies at GB. Thus, the PHI can effectively passivate two major point defects (under-coordinated $Pb^{2+}$ defects and iodide vacancies) of perovskites and improve the diffusion length.

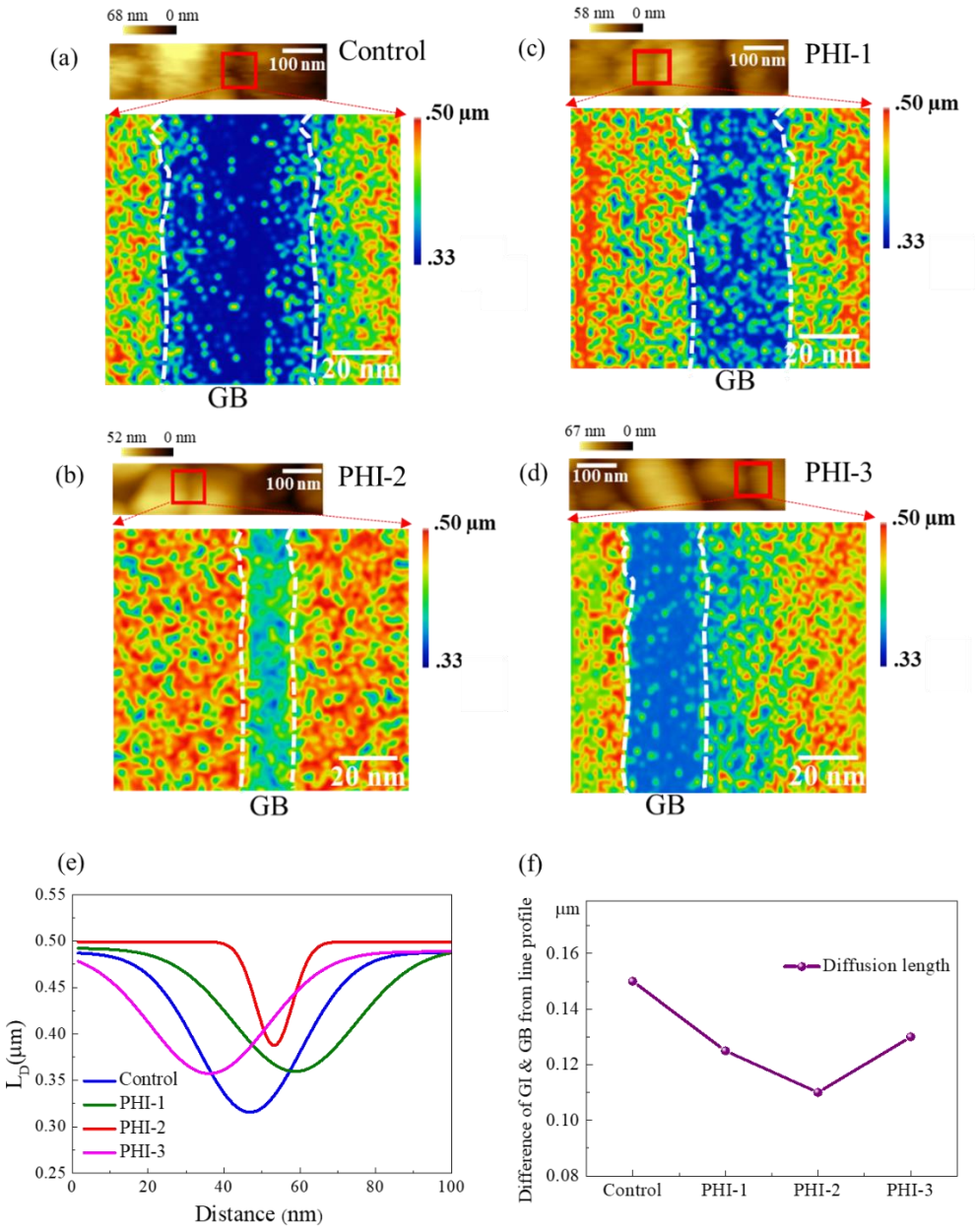


Figure 4.14 LT-AFM resolved mapping (100 nm × 100 nm) of $L_D$ (charge carrier diffusion length) for (a) control, (b) PHI-2, (c) PHI-1 and (d) PHI-3 perovskites, respectively. Red square indicated in the topography images was selected for the mapping. White dashed lines in the mapping show the GB. (e) Average line profile of $L_D$ along GI-GB-GI obtained from Fig. a-d. (f) Difference of GI and GB from line profile vs concentration of PHI solution.

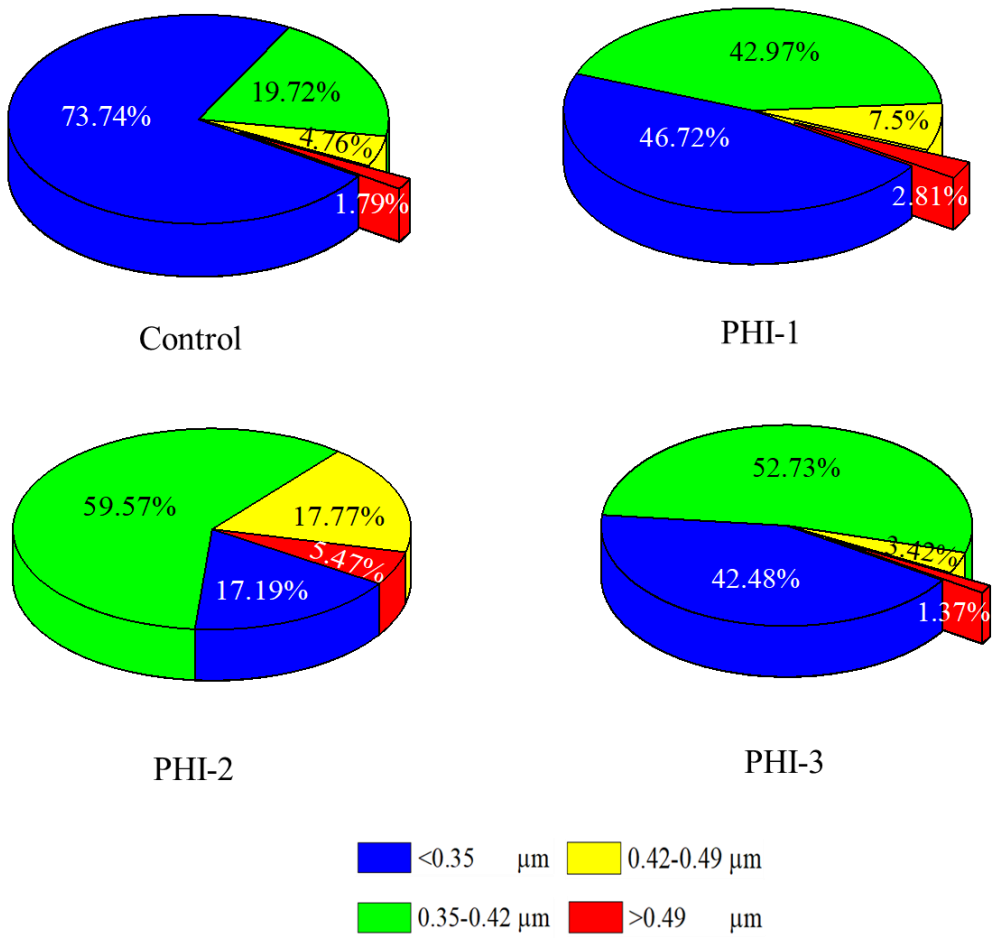


Figure 4.15 Pie chart distribution of apparent diffusion length at GB

4.2.2.4 Repeatability of the Nanoscale Mapping Measurement

To show the repeatability of data by LT-AFM, we measured TPV and TPC again at the same position for the control perovskite. Figure 4.16 shows the mappings of apparent (a) charge carrier recombination lifetime, (b) transport time, and (c) diffusion length at the same position in the control perovskite. Average difference between the mappings shown in Fig. 4.10a, 4.12a, 4.14a and Fig. 4.16 of carrier recombination lifetime, transport time and diffusion length at the same position are all less than ~2%. These small changes demonstrate that the measurements are repeatable at the same position.

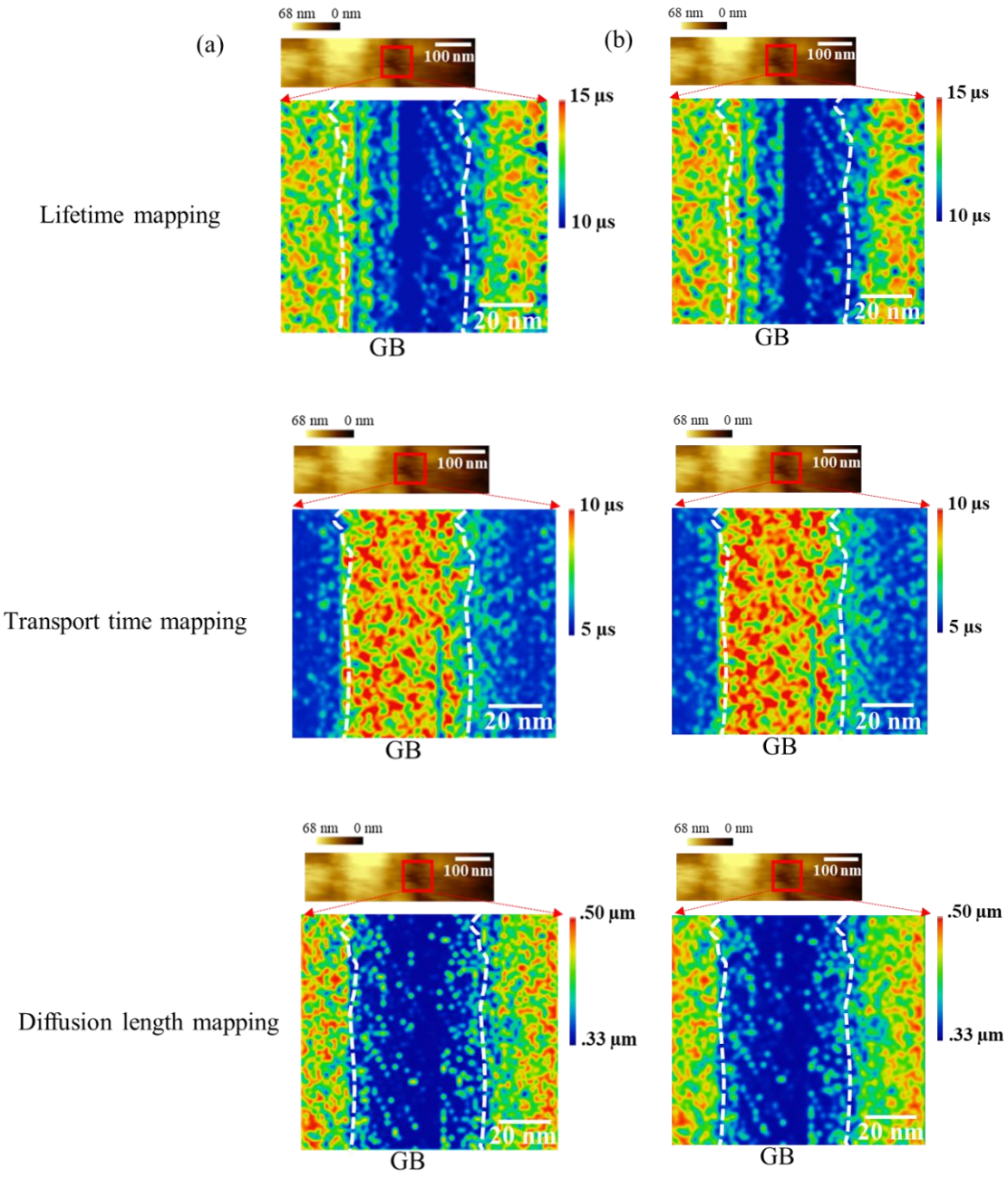


Figure 4.16 LT-AFM mappings (100 nm × 100 nm) of charge carrier lifetime, charge carrier transport time, and diffusion length of control perovskite repeated at the same position (a) first and (b) second, showing high repeatability of measurements. White dashed lines show the GB region.

### 4.2.3 GB passivation: Kelvin Probe Force Microscopy of Control and Passivated Perovskites

To further elucidate the effect of PHI passivation at GB, surface potential maps were obtained by using KPFM. The KPFM measures surface potential ($V_{SP}$) between the tip and sample with topography, simultaneously. An electrostatic force is generated between the tip and sample because of the difference in their Fermi energy levels, when the scanning tip approaches the sample surface. The work function of the tip is constant since we have used the same tip for all the samples.

Five different GB areas were selected for line profile measurements marked as white lines in the topography (Figure 4.17a) and surface potential image (Figure 4.17c) for control perovskites with a size of ~1 μm × ~1 μm. Figure 4.17e shows the $V_{SP}$ obtained from the line profiles across five different GBs and their adjacent grain surfaces. Interestingly in all the GBs, $V_{SP}$ at GB ($SP_{GB}$) show less values compared with the $V_{SP}$ at grain interiors ($SP_{GI}$). The difference between GB and GI ($\Delta SP_{GB}=SP_{GB}-SP_{GI}$) for the five different areas was calculated and the average was -38 mV. The average $\Delta SP_{GB}$ shows that the potential at the GB is lower than that of GIs. A lower potential at the GB compared with the GI corresponds to a hole barrier [122]. Therefore, it can be deduced that the GB of control perovskites act as a barrier for the holes.

Similarly, five different GB areas were selected for line profile measurements marked as white lines in the topography (Figure 4.17b) and the surface potential image (Figure 4.17d) for PHI-2 perovskite with a size of ~1 μm × ~1 μm. Figure 4.17f shows the $V_{SP}$ variation obtained from the line profiles across five different GBs and their adjacent grain surfaces. Interestingly, unlike the control perovskites, all the GBs show high $V_{SP}$ compared with the

adjacent GI. The $\Delta SP_{GB}$ between GB and adjacent GI for the five different areas was calculated and the average was +113 mV. The average $\Delta SP_{GB}$ shows that the potential at the GB is higher than that of GIs. This higher potential at the GB compared with the grain interior corresponds to an electron barrier[122]. Therefore, it can be estimated that the GBs of PHI-2 perovskites act as a barrier for the electrons. Nicoara et al. studied in detail about the GB passivation in polycrystalline $Cu(In,Ga)Se_2$ solar cells by alkali-fluoride post-deposition treatments through KPFM [122]. They reported that positively charged GB (GB with a downward band bending, corresponding to a hole barrier) severely affect the material performance. Hole barrier repels the holes and accumulates electrons which leads to increased electron density at GB. This forms a shunting path which is not desired for solar cell performance. However negatively charged GB (GB with an upward band bending, corresponding to an electron barrier) have negligible impacts on the performance and hence do not form any shunting paths. Therefore GBs corresponding to a hole barrier have significant impact on the material performance compared to electron barrier [122]. The study concluded that positively charged GBs have significant impact on the material performance due to undesired leakage paths. However, negatively charged GBs do not form such leakage paths and hence do not affect material performance [122]. Similarly, for polycrystalline perovskites, GB of control perovskites act as a barrier for the holes which repels holes and accumulates electrons. Thus, increased electron density forms an electron channel and creates shunting paths. On the other hand, GB of PHI-2 perovskites act as a barrier for the electrons which repels electrons and accumulates holes. GBs with electron barrier do not form any shunting paths. PHI helps to transform the hole barrier into an electron barrier so that no shunting paths are formed and hence passivates the GB.

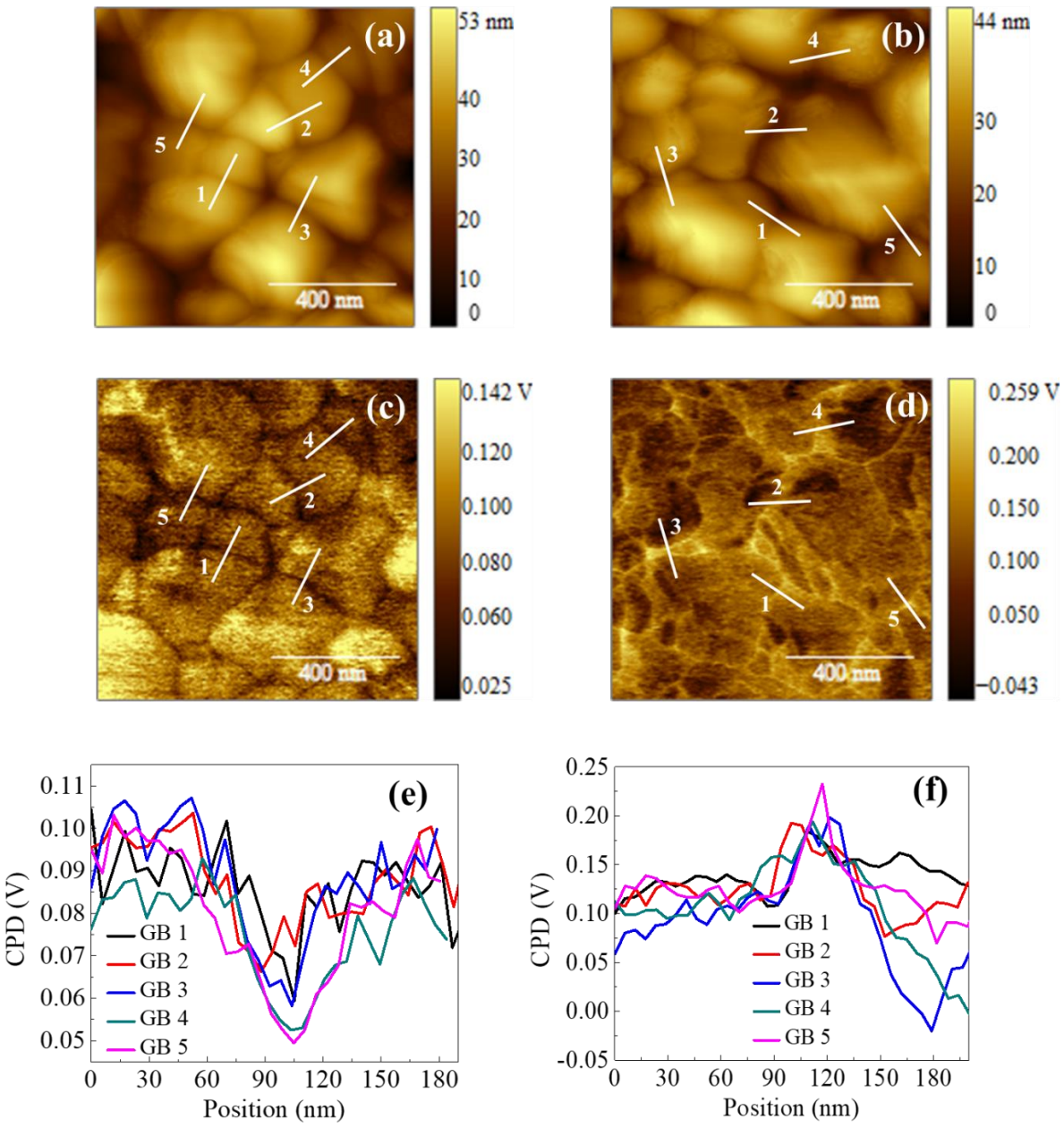


Figure 4.17 Topography of (a) control & (b) PHI-2 perovskites and their corresponding KPFM measurements (c) control and (d) PHI-2 perovskites, respectively. The GBs analyzed in this study are marked by white lines across GBs. Line profiles (e) control and (f) PHI-2 perovskites extracted from the KPFM images at five different GBs.

These conclusions support our observations on GB barrier of polycrystalline perovskites following the KPFM measurements. GBs of control perovskites due to positively charged defects such as under-coordinated $Pb^{2+}$ defects [104, 105] and iodide vacancies [57, 106] are susceptible to recombination and severely affect the material performance by forming leakage paths. PHI passivates these positively charged GB defects i.e. suppresses the leakage paths associated with hole barrier and thus improves the material performance.

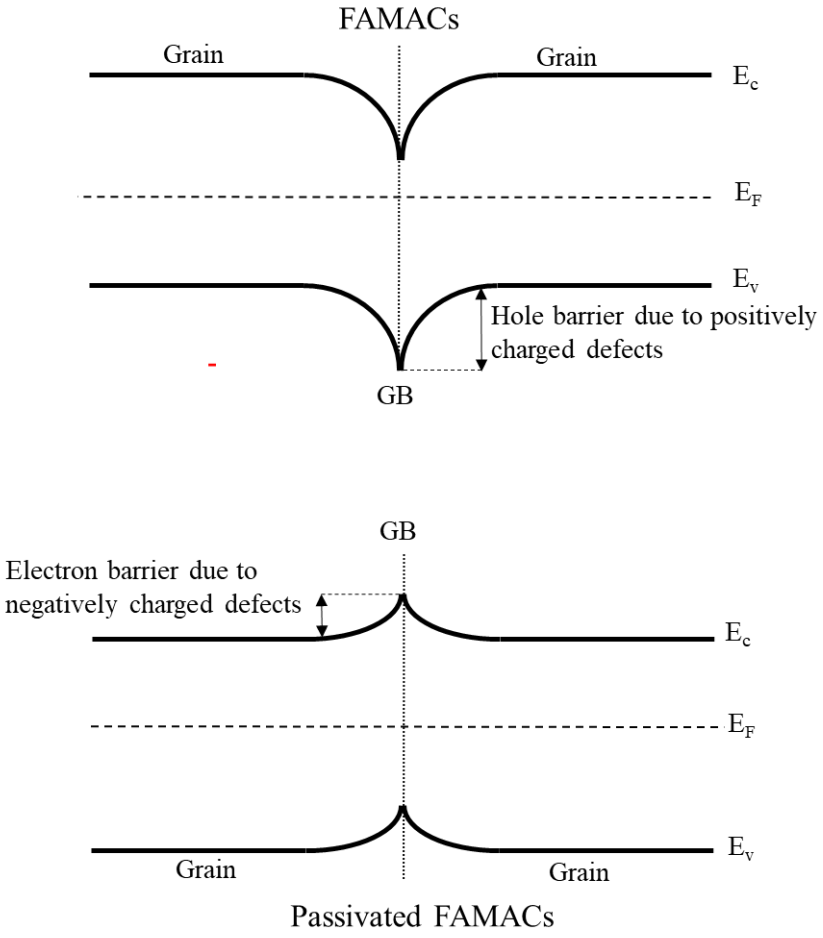


Figure 4.17.1 Electronic band structure at GBs for (a) FAMACs and (b) passivated FAMACs perovskites.

Figure 4.17.1 shows the electronic band structure at GBs for (a) FAMACs and (b) passivated FAMACs perovskites, respectively. Similarly, for polycrystalline perovskites, GB of control FAMACs perovskites act as a barrier for the holes which repels holes and accumulates electrons. On the other hand, GB of PHI-2 perovskites act as a barrier for the electrons which repels electrons and accumulates holes. GBs with electron barrier do not form any shunting paths. PHI helps to transform the hole barrier into an electron barrier so that no shunting paths are formed and hence passivates the GB.

### 4.2.4 GB passivation: Conductive Atomic Force Microscopy of Control and Passivated Perovskites

To better understand the effect of GB passivation, C-AFM was performed on the perovskite samples. Figure 4.18a and b show the C-AFM image of control and PHI-2 perovskites, respectively. A bias of 0.20 V was applied for the C-AFM measurements. The brighter contrast indicates a higher local current. The C-AFM images and corresponding line profile (Figure 4.18c and d) reveal that the control perovskite has higher current at the GB compared with the GI whereas current is lower at GB for the PHI-2 perovskite. Average current in GB obtained from line profile for the control is 1.46 nA, which decreases to 1.34 nA for the PHI-2 perovskite. Furthermore, average current at GI in PHI-2 perovskite (1.45 nA) is higher than control sample (1.35 nA). This suggests the passivation effect of the GB in PHI-2 perovskite, which is also consistent with other C-AFM studies on GI and GB [123]. PHI contains amines rich with lone pair electrons which can be donated to the under-coordinated $Pb^{2+}$ to form a coordination bond. Furthermore, iodide ions from the PHI coating can fill the iodide vacancies at GB. Thus, GB is passivated by PHI.

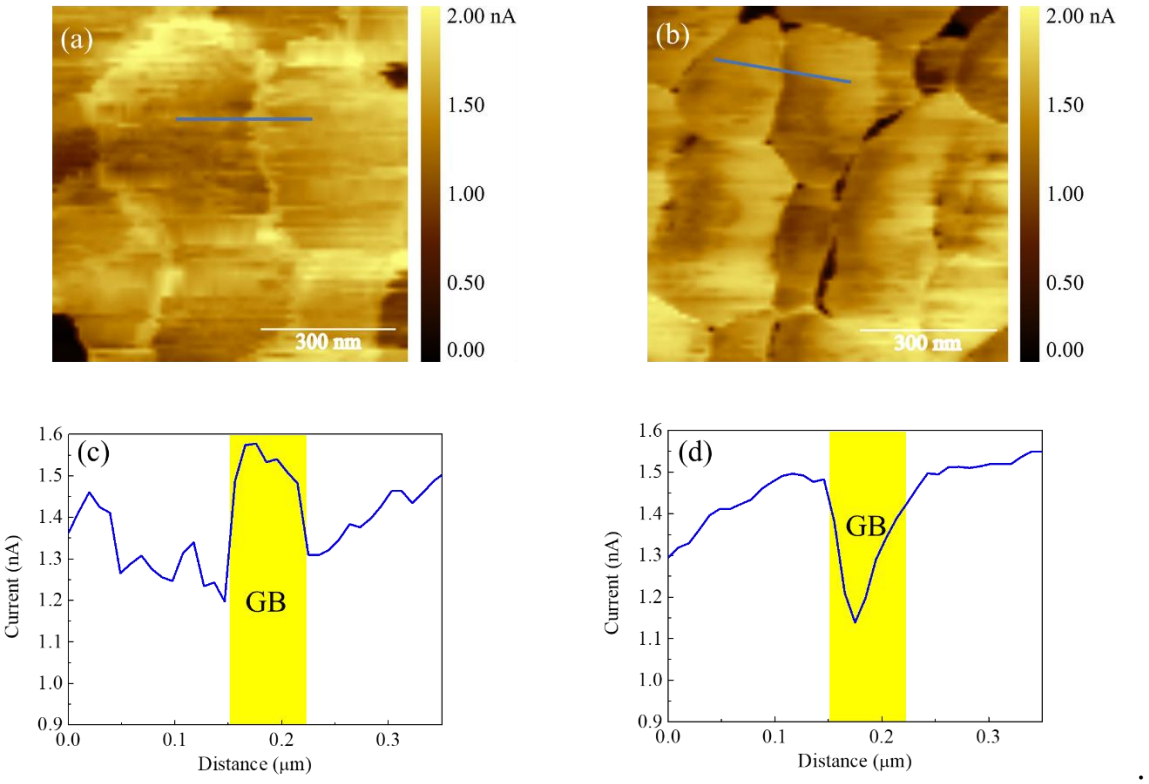


Figure 4.18 C-AFM images (a, b) and line profile of current (c, d) of control and PHI-2 perovskite films, respectively. Yellow rectangle (c, d) indicates the GB area.

## 4.3 Device Performance of $MAPbI_3$ and FAMACs Perovskite Solar Cell

A perovskite solar cell using a standard cell architecture (FTO/c-$TiO_2$/meso-$TiO_2$/ Perovskite/spiro-OMeTAD/Ag) was fabricated. Figure 4.19a shows the cross-sectional SEM images of the $MAPbI_3$ and FAMACs perovskite solar cells. The device obtained power conversion efficiency of 17.81% (Figure 4.19b) for $MAPbI_3$ and 18.15% for FAMACs (Figure 4.19c). Figure 4.20a shows the external quantum efficiency (EQE) spectra for both PSCs. Therefore, the PCE of the FAMACs devices are higher compared with the PCE of $MAPbI_3$ devices.

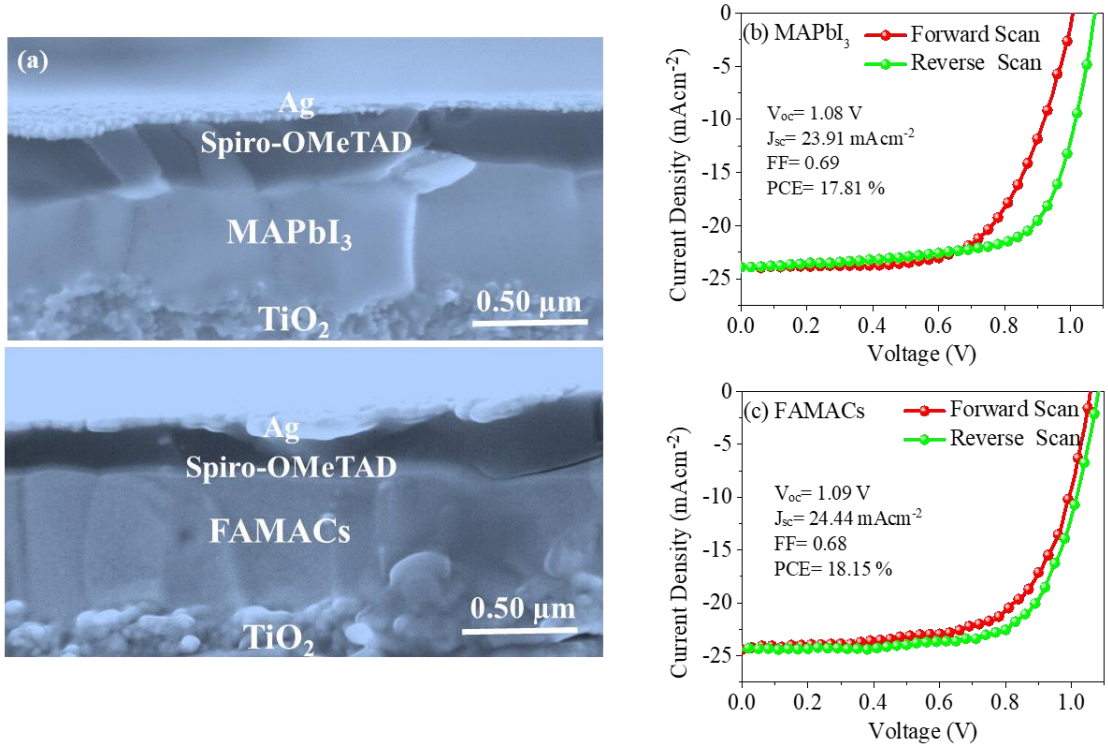


Figure 4.19 (a) Device structure adopted in this study via cross sectional SEM images. (b) The typical *J–V* curve of the (b) $MAPbI_3$ and (c) FAMACs perovskite devices under one-sun (100 mW $cm^{-2}$) conditions.

This integrated $J_{sc}$ from the EQE spectrum was found to be consistent with the $J_{sc}$ values obtained from the illuminated J-V curves under a solar simulator. Photovoltaic parameters under forward and reverse scan J-V curves are listed in Table 4.2. PSCs was fabricated without a hole transport layer (HTL) and their performance was evaluated in the Fig. 4.21 and Table 4.3. Perovskite films fabricated using the same conditions were used for nanoscale mapping of charge carrier dynamics. The detailed fabrication processes of the perovskite films and devices are described in the Experimental Section chapter 3.

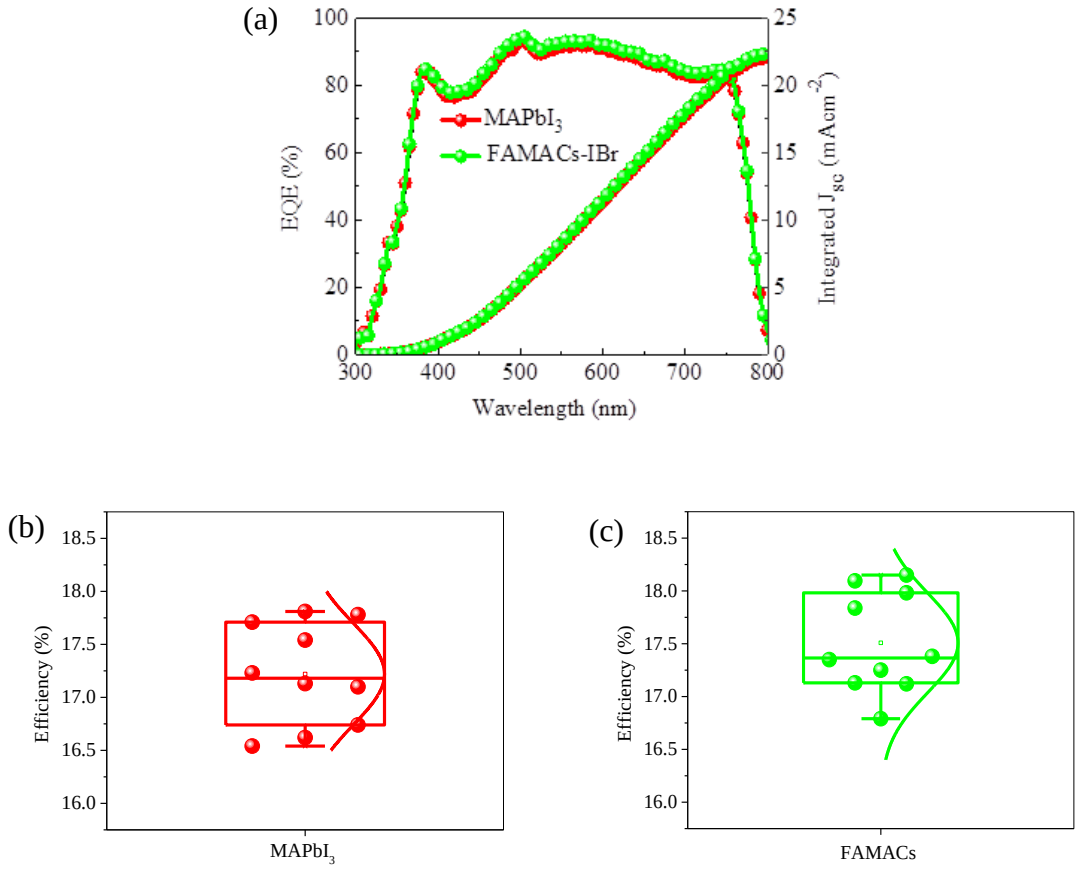


Figure 4.20 (a) EQE of the $MAPbI_3$ and FAMACs perovskite solar cells with best performing devices. (b) Statistics of efficiency for perovskite solar cell (b) $MAPbI_3$ and (c) FAMACs perovskite solar cells (10 devices).

Table 4.2 Photovoltaic parameters for $MAPbI_3$ and FAMACs perovskite solar cells

| Device | $J_{sc}$ (mAcm$^{-2}$) | | $V_{oc}$ (V) | | FF | | η (%) | |
|---|---|---|---|---|---|---|---|---|
| | Forward | Reverse | Forward | Reverse | Forward | Reverse | Forward | Reverse |
| $MAPbI_3$ | 23.90 | 23.91 | 1.01 | 1.08 | 0.63 | 0.69 | 15.21 | 17.81 |
| **FAMACs** | **24.41** | **24.44** | **1.06** | **1.09** | **0.64** | **0.68** | **16.68** | **18.15** |

Photovoltaic parameters under forward and reverse scan J-V curves are listed in Table 4.2 which shows FAMACs shows improved performance compared to $MAPbI_3$.

FAMACs shows improved photovoltaic parameters (listed in the Table 4.3) compared to its counterpart $MAPbI_3$. The efficiency is less in our case due to the selection of the Ag electrode. Generally Au or Carbon electrodes have been used for HTM free perovskite solar cells that provide good performance [6, 124]. We believe reaction Ag with the perovskite cause to degradation which results in poor efficiency [125, 126].

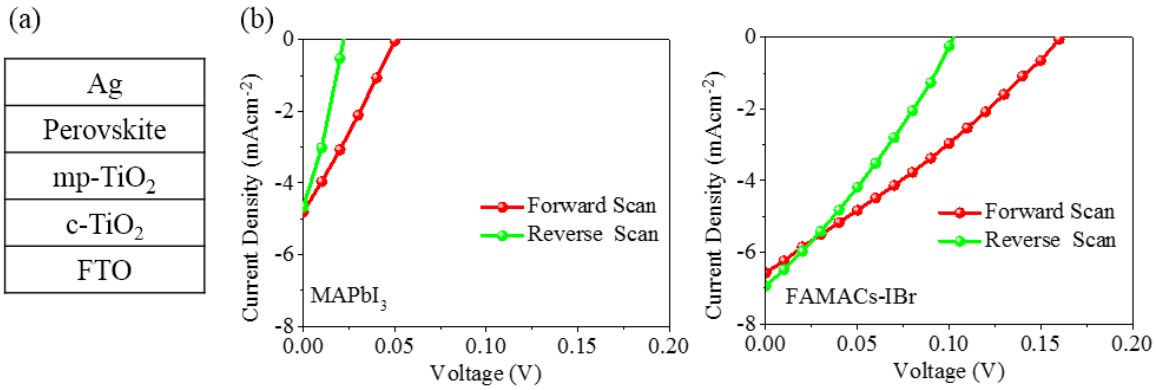


Figure 4.21 (a) Device structure, (b) Light current-voltage (J-V) characteristics of $MAPbI_3$ and FAMACs perovskite solar cells without HTM.

Table 4.3 Photovoltaic parameters for $MAPbI_3$ and FAMACs perovskite solar cells without HTM.

| Device | $J_{sc}$ ($mAcm^{-2}$) | | $V_{oc}$ (V) | | FF | | η (%) | |
|---|---|---|---|---|---|---|---|---|
| | Forward | Reverse | Forward | Reverse | Forward | Reverse | Forward | Reverse |
| $MAPbI_3$ | 4.81 | 4.66 | 0.05 | 0.03 | 0.26 | 0.22 | 0.06 | 0.03 |
| FAMACs | 6.57 | 6.94 | 0.16 | 0.11 | 0.29 | 0.28 | 0.30 | 0.21 |

Without HTM, FAMACs shows better performance than $MAPbI_3$ which proves our assumption of less defect ion migration at GB. Thus, FAMACs shows improved performance compared to $MAPbI_3$.

Table 4.4 shows the t-test metric and p-value calculation between $MAPbI_3$ and FAMACs perovskite solar cells for PCE of 10 devices. The test metrices were t-test metric<1.65 and p-value<0.05 and any values less than that will create satisfactory null hypothesis. t-test metric and p-value between $MAPbI_3$ and FAMACs perovskite solar cells are ~1.36 and ~ .096, respectively.

Table 4.4 t-test metric and p-value calculation between $MAPbI_3$ and FAMACs perovskite solar cell samples for PCE of 10 devices.

| t-test metric and p-value between | t-test metric | p-value | Significance t-test metric<1.65 p-value<0.05 |
|---|---|---|---|
| $MAPbI_3$ and FAMACs | 1.3542 | 0.096215 | Not significant difference |

4.4 Device Performance of Perovskite Solar Cell with Different Concentration of PHI

Different PHI concentrations were used to fabricate a thin passivation layer on the top of FAMACs (control) perovskite to study the GB passivation. The studied concentrations of PHI are 1mg/mL PHI (PHI-1), 2mg/mL PHI (PHI-2) and 3mg/mL PHI (PHI-3). PSCs using a standard cell architecture (ITO/$SnO_2$/PCBM/Perovskite/PHI/spiro-OMeTAD/Ag) shown in Fig. 4.19a were fabricated with different concentration of PHI solution. The dependence of the device performance on the PHI concentration (Figure 4.19b) for 10 devices shows that the PCE increases for PHI-1, reaches maximum for PHI-2 and reduces for PHI-3. The average of 10 control devices show a PCE of 16.31 ± 0.43 % whereas it increases to 19.65 ± 0.27 % for treated PSC with PHI-2 (Figure 4.19b). For PHI -1 and PHI-3, the average PCE for 10 devices are17.52 ± 0.33 % and 17.02 ± 0.26 %, respectively.

The PSC with PHI-2 gives a champion efficiency of 20.09% in forward scan (Figure 4.19c), while PSC without PHI obtained a power conversion efficiency of 16.86% in forward scan (Figure 4.19c). External quantum efficiency (EQE) spectra for both PSCs are shown in Figure 4.19d. Integrated $J_{sc}$ (Figure 4.19d) from the EQE spectrum was consistent with the $J_{sc}$ values obtained from the J-V curves (Figure 4.19c). Integrated current density from the EQE spectrum was found to be rational with the current density values obtained from the J-V measurements (Figure 4.19c). The difference between current density obtained from EQE and J-V measurements are in good agreement with other report on thin film solar cells [127-131]. Thus, this rationality of current density values from EQE and J-V minimizes the overestimation of device efficiency.

The dependence of the device performance on the PHI concentration (Figure 4.20a) for 10 devices shows that the PCE increases for PHI-1, reaches maximum for PHI-2 and reduces for PHI-3. Figure 4.20b shows the *J–V* curve of the best performing control, PHI-1, PHI-2, and PHI-3 perovskite devices under one-sun (100 mW $cm^{-2}$) conditions. The control resulted in a least power conversion efficiency. After adding a different concentration of PHI as surface passivating layer, the power conversion efficiency results were improved. For PHI-2, the power conversion efficiency was significantly improved. Following same experimental conditions, perovskite films were fabricated without hole transport layer and electrodes for nanoscale mapping where AFM tip serve as the electrode. PHI contains amines rich with lone pair electrons which can be donated to the under-coordinated $Pb^{2+}$ to form a coordination bond. Furthermore, iodide ions from the PHI coating can fill the iodide vacancies at GB. PHI-1 and PHI-3 yielded improved PCE compared to control; however, PHI-2 resulted in the best performance in terms of PCE.

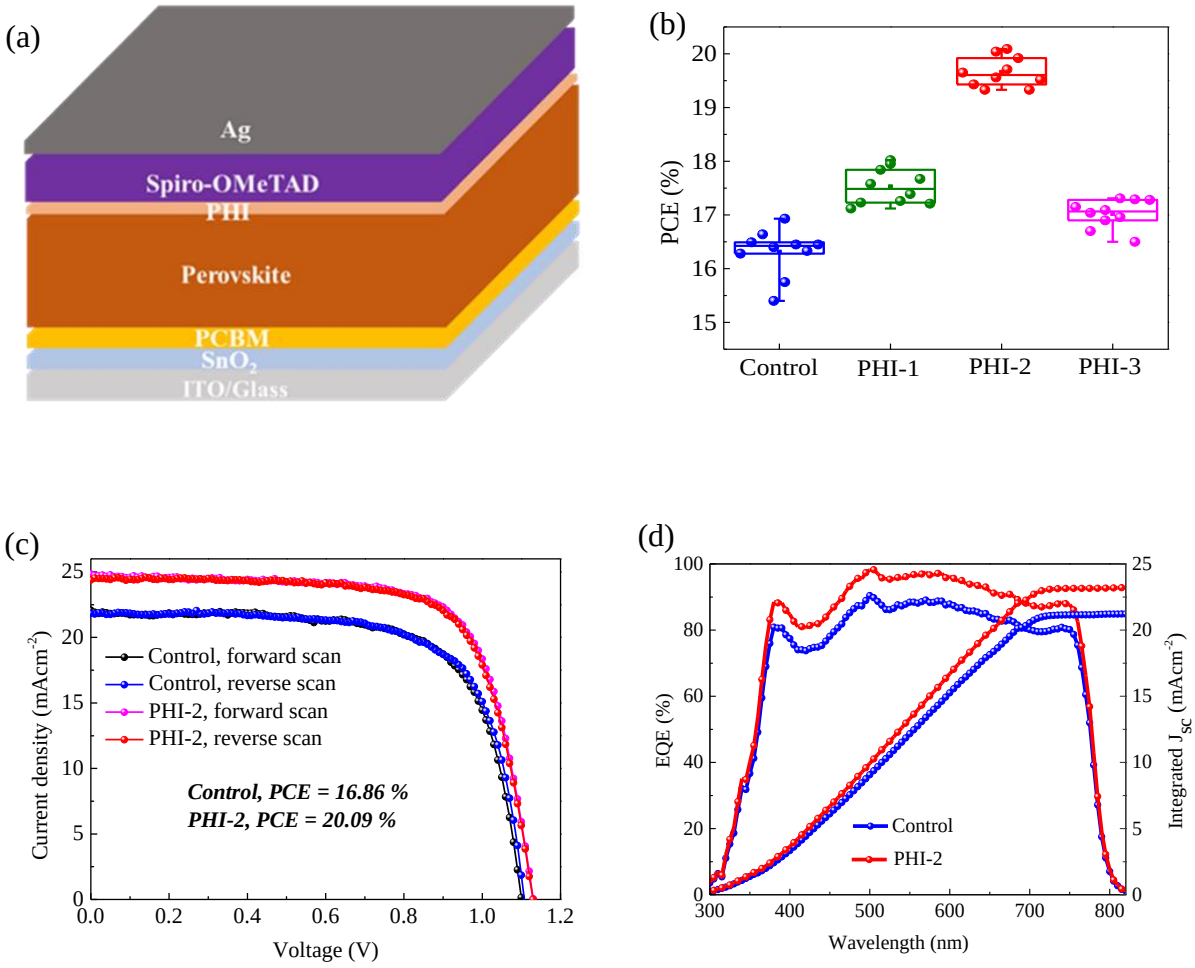


Figure 4.22 (a) Device structure adopted in this study. (b) The dependence of device performance on concentration of PHI solution. (c) The typical *J*–*V* curve of the best performing control and PHI-2 perovskite device under one-sun (100 mW $cm^{-2}$) conditions and respective (d) EQE curves.

Thus, the PHI can effectively passivate two major point defects (under-coordinated $Pb^{2+}$ defects and iodide vacancies) of perovskites and improve the device performance. PHI-1 and PHI-3 yielded improved PCE compared to control; however, PHI-2 resulted in the best performance in terms of PCE.

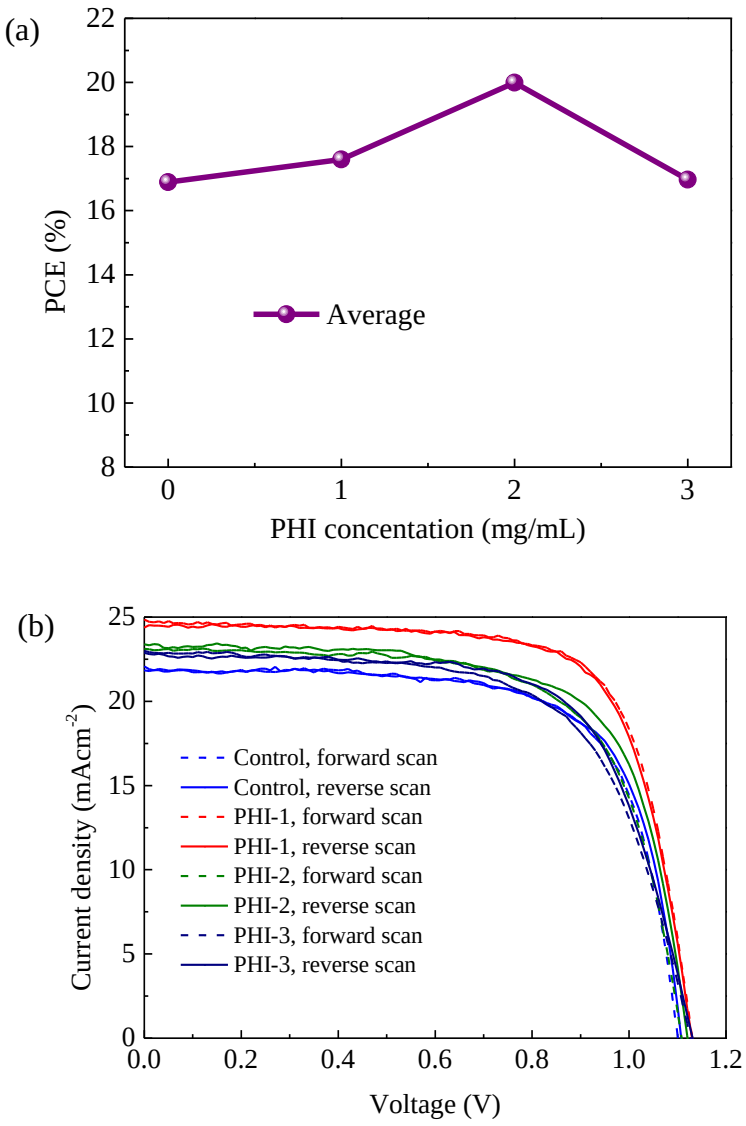


Figure 4.23 (a) The dependence of device performance on concentration of PHI solution. (b)The typical *J–V* curve for control, PHI-1, PHI-2, and PHI-3 devices.

Thus, in conclusion, the most optimal performance was recorded for PHI-2 perovskites compared to PHI-1 and PHI-3.Table 4.5 shows the photovoltaic parameters (short circuit current density, open circuit voltage, fill factor and power conversion efficiency) for FAMACs perovskite solar cells with and without different concentration of PHI solution. It also lists the average PCE of 10 devices for FAMACs perovskite solar cells.

Table 4.5 Photovoltaic parameters for FAMACs perovskite solar cells with and without different concentration of PHI solution.

| Device | $J_{sc}$ ($mAcm^{-2}$) | | $V_{oc}$ (V) | | FF | | PCE (%) | | Average PCE of 10 devices (%) |
|---|---|---|---|---|---|---|---|---|---|
| | Forward | Reverse | Forward | Reverse | Forward | Reverse | Forward | Reverse | |
| Control | 22.07 | 21.83 | 1.10 | 1.11 | 0.69 | 0.70 | 16.86 | 16.93 | 16.31 ± 0.43 % |
| PHI-1 | 23.11 | 23.38 | 1.11 | 1.13 | 0.67 | 0.68 | 17.19 | 18.02 | 17.52 ± 0.33 % |
| **PHI-2** | **24.85** | **24.38** | **1.13** | **1.13** | **0.72** | **0.72** | **20.09** | **19.88** | **19.65 ± 0.27 %** |
| PHI-3 | 23 | 22.88 | 1.13 | 1.14 | 0.64 | 0.66 | 16.63 | 17.31 | 17.02 ± 0.26 % |

Table 4.6 shows the t-test metric and p-value calculation between control and different concentration PHI samples for PCE of 10 devices. The test metrices were t-test metric<1.65 and p-value<0.05 and any values less than that will create satisfactory null hypothesis. t-test metric and p-value between control and PHI-2 are ~6.57 and < .00001, respectively. This t-test metric and p-value shows the significant difference of PCE between control and PHI-2 samples. t-test metric and p-value between control and PHI-1 are ~2.28 and 0.035015, respectively. This t-test metric and p-value shows the moderate difference of PCE between control and PHI-1 samples. t-test metric and p-value between control and PHI-3 are ~1.41 and 0.176168, respectively. This t-test metric and p-value shows no difference of PCE between control and PHI-3 samples. It clearly means that PHI-2 samples show the highest improvement in terms of PCE of the devices with respect to control devices whereas the PCE improvement for PHI-1 and PHI-3 devices are less or similar. Therefore, in PHI-1 and PHI-3 samples, the increases are not statistically significant at the 5% level compared to PHI-2 samples.

Table 4.6 t-test metric and p-value calculation between control and different concentration PHI samples for PCE of 10 devices.

| t-test metric and p-value between | t-test metric | p-value | Significance<br>t-test metric<1.65<br>p-value<0.05 |
|---|---|---|---|
| Control and PHI-1 | 2.28 | 0.035015 | difference |
| **Control and PHI-2** | **6.57** | **< .00001** | **Significant difference** |
| Control and PHI-3 | 1.41 | 0.176168 | No difference |

During the annealing process, $A^+$([FAMACs]$^+$) cations and $X^-$($I^-$, $Br^-$) anions from perovskite molecule can be lost and thus resulting under-coordinated $Pb^{2+}$ defects. PHI contains amines rich with lone pair electrons which can be donated to the under-coordinated $Pb^{2+}$ to form a coordination bond. Furthermore, iodide ions from the PHI coating can fill the iodide vacancies at GB. Thus, the PHI can effectively passivate two major point defects (under-coordinated $Pb^{2+}$ defects and iodide vacancies) of perovskites. Thus, PHI can effectively passivate the under-coordinated $Pb^{2+}$ defects and iodide vacancies at the grain boundary which results in champion PCE of ~20% for PHI passivated perovskite solar cells. PHI-1 and PHI-3 yielded improved PCE compared to control; however, PHI-2 resulted in the best performance in terms of PCE. Thus, in conclusion, the most optimal performance was recorded for PHI-2 perovskites compared to PHI-1 and PHI-3. From the device point of view, $MAPbI_3$ shows ~17% compared to ~ 18% of FAMACs while passivated FAMACs shows ~20%. This clearly indicates that GB passivation in FAMACs reduces the positively charged defects and gives champion PCE. While the negatively charged defects barely affect the device performance.

# Chapter 5 Conclusions and Future Directions

## 5.1 Conclusions

The study adapted here discusses the nanoscale spatial realization of grain boundary defects and its passivation in perovskite solar cells. Firstly, conventional $MAPbI_3$ and state-of-the-art FAMACs perovskite GBs were studied in detail using KPFM. The density of trap states shows that FAMACs perovskites have lower defects compared with $MAPbI_3$ perovskites ($6.30\times10^{10}/cm^2$ for FAMACs versus $16.4\times10^{10}/cm^2$ for $MAPbI_3$). This improvement is caused by the less activation energy of the point defects in FAMACs due to mixing of cations and anions in perovskite structure compared with $MAPbI_3$ perovskites. The conclusions are well supported by the average $\Delta\varphi_{GB}$ (13.33meV for FAMACs versus 28.33meV for $MAPbI_3$), $P_{net}$ ($3.96\times10^{15}/cm^3$ for FAMACs versus $9.03\times10^{15}/cm^3$ for $MAPbI_3$), $P_{GB\text{-}trap}$ ($6.30\times10^{10}/cm^2$ for FAMACs versus $16.4\times10^{10}/cm^2$ for $MAPbI_3$). FAMACs perovskite GBs are less dominated by the defect ion migration evident from the negligible local dark-current hysteresis at GBs. However, $MAPbI_3$ perovskite GBs are more susceptible to defect ion migration evident from the significant local dark-current hysteresis at GBs.

Secondly, passivation of grain boundaries has been shown by post treating FAMACs perovskites with an organic salt PHI through a detailed study of the nanoscale mapping of charge carrier dynamics, surface potential and AFM current images. Defects analysis and passivation at GB of FAMACs perovskite through charge carrier dynamics nanoscale mapping, KPFM and CAFM demonstrate that optimized concentration of PHI can passivates the positively charged defects and significantly improves charge carrier dynamics at GB compared to control sample. This improvement in apparent recombination

lifetime, transport time and diffusion length indicate less positively charged defects at GB which results in enhanced PCE in optimal PHI containing FAMACs devices. GB passivation imaging via helps to distinguish the physical areas on the perovskite films which has better apparent recombination lifetime, transport time and diffusion length from that which do not. From the device point of view, $MAPbI_3$ shows ~17% compared to ~ 18% of FAMACs while passivated FAMACs shows ~20%. This clearly indicates that GB passivation in FAMACs reduces the positively charged defects and gives champion PCE.

## 5.2 Future Directions

The presented nanoscale spatial realization of grain boundary defects and its passivation in perovskite solar cells are expected to serve as a blueprint for the studies of grain boundaries in any other polycrystalline materials. GB passivate material investigation holds the promise for highly efficient perovskite solar cells near to thermodynamic limit of power conversion efficiency. The nanoscale defects analysis and imaging of GB passivation in this study are expected to pave the ways toward better understanding of charge carrier behaviors and help find the appropriate passivate materials for perovskite GB to achieve high performance next generation solar cells.

# LITERATURE CITED


1. Now, R. *Renewables produce 85% of global power, nearly 50% of energy in 2050*. 2017; Available from: https://renewablesnow.com/news/renewables-produce-85-of-global-power-nearly-50-of-energy-in-2050-582235/.
2. Blakers, A., et al., *High efficiency silicon solar cells.* Energy Procedia, 2013. **33**: p. 1-10.
3. *National Center for Photovoltaics (NCPV) at the National Renewable Energy Laboratory (NREL); https://www.nrel.gov/pv/cell-efficiency.html.*
4. Chowdhury, M.S., et al., *An overview of solar photovoltaic panels' end-of-life material recycling.* Energy Strategy Reviews, 2020. **27**: p. 100431.
5. Kojima, A., et al., *Organometal Halide Perovskites as Visible-Light Sensitizers for Photovoltaic Cells.* Journal of the American Chemical Society, 2009. **131**(17): p. 6050-6051.
6. Jiang, Q., et al., *Surface passivation of perovskite film for efficient solar cells.* Nature Photonics, 2019. **13**(7): p. 460-466.
7. Green, M.A., et al., *Solar cell efficiency tables (Version 55).* Progress in Photovoltaics: Research and Applications, 2020. **28**(1): p. 3-15.
8. Werner, J., et al., *Perovskite/Perovskite/Silicon Monolithic Triple-Junction Solar Cells with a Fully Textured Design.* ACS Energy Letters, 2018. **3**(9): p. 2052-2058.
9. Saliba, M., et al., *Incorporation of rubidium cations into perovskite solar cells improves photovoltaic performance.* Science, 2016.
10. Solar, S. *Solar cell efficiency records over time for leading PV technologies—crystalline silicon, copper indium gallium diselenide (CIGS), cadmium telluride (CdTe), and perovskites. Tandem cells can reach a much higher efficiency than single-junction cells.* 2019; Available from: https://www.swiftsolar.com/2019/04/11/introducing-swift-solar/.
11. Wetzelaer, G.-J.A.H., et al., *Trap-Assisted Non-Radiative Recombination in Organic–Inorganic Perovskite Solar Cells.* Advanced Materials, 2015. **27**(11): p. 1837-1841.
12. Zhou, Y., et al., *Crystal Morphologies of Organolead Trihalide in Mesoscopic/Planar Perovskite Solar Cells.* The Journal of Physical Chemistry Letters, 2015. **6**(12): p. 2292-2297.
13. Huang, J., Y. Shao, and Q. Dong, *Organometal Trihalide Perovskite Single Crystals: A Next Wave of Materials for 25% Efficiency Photovoltaics and Applications Beyond?* The Journal of Physical Chemistry Letters, 2015. **6**(16): p. 3218-3227.
14. Lin, C., et al., *Effect of Bromine Substitution on the Ion Migration and Optical Absorption in MAPbI3 Perovskite Solar Cells: The First-Principles Study.* ACS Applied Energy Materials, 2018. **1**(3): p. 1374-1380.
15. Wei, D., et al., *Ion-Migration Inhibition by the Cation–π Interaction in Perovskite Materials for Efficient and Stable Perovskite Solar Cells.* Advanced Materials, 2018. **30**(31): p. 1707583.

16. Sherkar, T.S., et al., *Recombination in Perovskite Solar Cells: Significance of Grain Boundaries, Interface Traps, and Defect Ions.* ACS Energy Letters, 2017. **2**(5): p. 1214-1222.
17. Chu, Z., et al., *Impact of grain boundaries on efficiency and stability of organic-inorganic trihalide perovskites.* Nature Communications, 2017. **8**(1): p. 2230.
18. Noel, N.K., et al., *Enhanced photoluminescence and solar cell performance via Lewis base passivation of organic–inorganic lead halide perovskites.* ACS nano, 2014. **8**(10): p. 9815-9821.
19. Liang, P.-W., et al., *Additive Enhanced Crystallization of Solution-Processed Perovskite for Highly Efficient Planar-Heterojunction Solar Cells.* Advanced Materials, 2014. **26**(22): p. 3748-3754.
20. de Quilettes, D.W., et al., *Impact of microstructure on local carrier lifetime in perovskite solar cells.* Science, 2015. **348**(6235): p. 683.
21. Yang, M., et al., *Do grain boundaries dominate non-radiative recombination in CH3NH3PbI3 perovskite thin films?* Physical Chemistry Chemical Physics, 2017. **19**(7): p. 5043-5050.
22. Vrućinić, M., et al., *Local Versus Long-Range Diffusion Effects of Photoexcited States on Radiative Recombination in Organic–Inorganic Lead Halide Perovskites.* Advanced Science, 2015. **2**(9): p. 1500136-n/a.
23. Simpson, M.J., et al., *Imaging Electronic Trap States in Perovskite Thin Films with Combined Fluorescence and Femtosecond Transient Absorption Microscopy.* The Journal of Physical Chemistry Letters, 2016. **7**(9): p. 1725-1731.
24. Abdi-Jalebi, M., et al., *Impact of Monovalent Cation Halide Additives on the Structural and Optoelectronic Properties of CH3NH3PbI3 Perovskite.* Advanced Energy Materials, 2016. **6**(10): p. 1502472-n/a.
25. Eperon, G.E., et al., *Morphological Control for High Performance, Solution-Processed Planar Heterojunction Perovskite Solar Cells.* Advanced Functional Materials, 2014. **24**(1): p. 151-157.
26. Kutes, Y., et al., *Mapping the Photoresponse of CH3NH3PbI3 Hybrid Perovskite Thin Films at the Nanoscale.* Nano Letters, 2016. **16**(6): p. 3434-3441.
27. Oh, S.J., et al., *Mapping the Competition between Exciton Dissociation and Charge Transport in Organic Solar Cells.* ACS Applied Materials & Interfaces, 2016. **8**(42): p. 28743-28749.
28. Douhéret, O., et al., *High resolution electrical characterisation of organic photovoltaic blends.* Microelectronic Engineering, 2007. **84**(3): p. 431-436.
29. Goh, C., et al., *Molecular-weight-dependent mobilities in regioregular poly(3-hexyl-thiophene) diodes.* Applied Physics Letters, 2005. **86**(12): p. 122110.
30. Reid, O.G., K. Munechika, and D.S. Ginger, *Space Charge Limited Current Measurements on Conjugated Polymer Films using Conductive Atomic Force Microscopy.* Nano Letters, 2008. **8**(6): p. 1602-1609.
31. Wood, D., et al., *Quantitative Nanoscale Mapping with Temperature Dependence of the Mechanical and Electrical Properties of Poly(3-hexylthiophene) by Conductive Atomic Force Microscopy.* The Journal of Physical Chemistry C, 2015. **119**(21): p. 11459-11467.

32. Butt, H.-J., B. Cappella, and M. Kappl, *Force measurements with the atomic force microscope: Technique, interpretation and applications.* Surface Science Reports, 2005. **59**(1): p. 1-152.
33. Button, S.W. and J.M. Mativetsky, *High-resolution charge carrier mobility mapping of heterogeneous organic semiconductors.* Applied Physics Letters, 2017. **111**(8): p. 083302.
34. Zhong, H., et al., *Measuring the local mobility of graphene on semiconductors.* Physical Review Materials, 2018. **2**(4): p. 043801.
35. Peng, J., et al., *Insights into charge carrier dynamics in organo-metal halide perovskites: from neat films to solar cells.* Chemical Society Reviews, 2017. **46**(19): p. 5714-5729.
36. Guo, P., et al., *Surface & grain boundary co-passivation by fluorocarbon based bifunctional molecules for perovskite solar cells with efficiency over 21%.* Journal of Materials Chemistry A, 2019. **7**(6): p. 2497-2506.
37. Jiang, Q., et al., *Planar-Structure Perovskite Solar Cells with Efficiency beyond 21%.* Advanced Materials, 2017. **29**(46): p. 1703852.
38. Jodlowski, A.D., et al., *Large guanidinium cation mixed with methylammonium in lead iodide perovskites for 19% efficient solar cells.* Nature Energy, 2017. **2**(12): p. 972-979.
39. Abdi-Jalebi, M., et al., *Maximizing and stabilizing luminescence from halide perovskites with potassium passivation.* Nature, 2018. **555**: p. 497.
40. Lee, D.S., et al., *Passivation of Grain Boundaries by Phenethylammonium in Formamidinium-Methylammonium Lead Halide Perovskite Solar Cells.* ACS Energy Letters, 2018. **3**(3): p. 647-654.
41. Hoque, M.N.F., et al., *Effects of Moisture-Based Grain Boundary Passivation on Cell Performance and Ionic Migration in Organic–Inorganic Halide Perovskite Solar Cells.* ACS Applied Materials & Interfaces, 2018. **10**(36): p. 30322-30329.
42. Eperon, G.E., D. Moerman, and D.S. Ginger, *Anticorrelation between Local Photoluminescence and Photocurrent Suggests Variability in Contact to Active Layer in Perovskite Solar Cells.* ACS Nano, 2016. **10**(11): p. 10258-10266.
43. Draguta, S., et al., *A quantitative and spatially resolved analysis of the performance-bottleneck in high efficiency, planar hybrid perovskite solar cells.* Energy & Environmental Science, 2018. **11**(4): p. 960-969.
44. Draguta, S., et al., *Spatially Non-uniform Trap State Densities in Solution-Processed Hybrid Perovskite Thin Films.* The Journal of Physical Chemistry Letters, 2016. **7**(4): p. 715-721.
45. Lee, B., et al., *Evaluating the optoelectronic quality of hybrid perovskites by conductive atomic force microscopy with noise spectroscopy.* ACS applied materials & interfaces, 2016. **8**(45): p. 30985-30991.
46. Shao, Y., et al., *Grain boundary dominated ion migration in polycrystalline organic–inorganic halide perovskite films.* Energy & Environmental Science, 2016. **9**(5): p. 1752-1759.
47. Zhao, Z., et al., *Probing the Photovoltage and Photocurrent in Perovskite Solar Cells with Nanoscale Resolution.* Advanced Functional Materials, 2016. **26**(18): p. 3048-3058.

48. Szostak, R., et al., *Nanoscale mapping of chemical composition in organic-inorganic hybrid perovskite films.* Science Advances, 2019. **5**(10): p. eaaw6619.
49. Li, J.-J., et al., *Microscopic Investigation of Grain Boundaries in Organolead Halide Perovskite Solar Cells.* ACS Applied Materials & Interfaces, 2015. **7**(51): p. 28518-28523.
50. Yun, J.S., et al., *Benefit of Grain Boundaries in Organic–Inorganic Halide Planar Perovskite Solar Cells.* The Journal of Physical Chemistry Letters, 2015. **6**(5): p. 875-880.
51. Yi, Z., et al., *Will organic–inorganic hybrid halide lead perovskites be eliminated from optoelectronic applications?* Nanoscale Advances, 2019. **1**(4): p. 1276-1289.
52. Bahrami, B., *A Kinetic Monte Carlo Study of Mesoscopic Perovskite Solar Cell Performance Behavior*. 2019.
53. Yin, W.-J., T. Shi, and Y. Yan, *Unusual defect physics in CH3NH3PbI3 perovskite solar cell absorber.* Applied Physics Letters, 2014. **104**(6): p. 063903.
54. Lee, J.-W., et al., *The role of grain boundaries in perovskite solar cells.* Materials Today Energy, 2018. **7**: p. 149-160.
55. Zhu, Y., et al., *Recent Progress on Interface Engineering for High-Performance, Stable Perovskites Solar Cells.* Advanced Materials Interfaces, 2020. **7**(11): p. 2000118.
56. Bahrami, B., et al., *Nanoscale spatial mapping of charge carrier dynamics in perovskite solar cells.* Nano Today, 2020. **33**: p. 100874.
57. Huang, H., et al., *Lead halide perovskite nanocrystals in the research spotlight: stability and defect tolerance.* ACS energy letters, 2017. **2**(9): p. 2071-2083.
58. Dymshits, A., et al., *The electronic structure of metal oxide/organo metal halide perovskite junctions in perovskite based solar cells.* Scientific Reports, 2015. **5**: p. 8704.
59. Eames, C., et al., *Ionic transport in hybrid lead iodide perovskite solar cells.* Nature Communications, 2015. **6**: p. 7497.
60. Liu, N. and C. Yam, *First-principles study of intrinsic defects in formamidinium lead triiodide perovskite solar cell absorbers.* Physical Chemistry Chemical Physics, 2018. **20**(10): p. 6800-6804.
61. Shi, J., et al., *Opto-electro-modulated transient photovoltage and photocurrent system for investigation of charge transport and recombination in solar cells.* Review of Scientific Instruments, 2016. **87**(12): p. 123107.
62. Zhang, D., et al., *On the modeling of dispersive transient photocurrent response of organic solar cells.* Organic Electronics, 2019. **70**: p. 42-47.
63. Stranks, S.D., et al., *Recombination Kinetics in Organic-Inorganic Perovskites: Excitons, Free Charge, and Subgap States.* Physical Review Applied, 2014. **2**(3): p. 034007.
64. Yang, W.S., et al., *Iodide management in formamidinium-lead-halide–based perovskite layers for efficient solar cells.* Science, 2017. **356**(6345): p. 1376.
65. Long, R., J. Liu, and O.V. Prezhdo, *Unravelling the effects of grain boundary and chemical doping on electron–hole recombination in CH3NH3PbI3 perovskite by time-domain atomistic simulation.* Journal of the American Chemical Society, 2016. **138**(11): p. 3884-3890.

66. Lee, J.H., et al., *A Solution-Processed Spinel CuCo2O4 as an Effective Hole Transport Layer for Efficient Perovskite Solar Cells with Negligible Hysteresis.* ACS Sustainable Chemistry & Engineering, 2019. **7**(21): p. 17661-17670.
67. Prochowicz, D., et al., *Charge Accumulation, Recombination, and Their Associated Time Scale in Efficient (GUA) x (MA) 1–x PbI3-Based Perovskite Solar Cells.* ACS omega, 2019. **4**(16): p. 16840-16846.
68. Zhao, X., et al., *20% efficient perovskite solar cells with 2D electron transporting layer.* Advanced Functional Materials, 2019. **29**(4): p. 1805168.
69. Snaith, H.J. and M. Grätzel, *Electron and hole transport through mesoporous TiO2 infiltrated with Spiro-MeOTAD.* Advanced materials, 2007. **19**(21): p. 3643-3647.
70. Heo, J.H., et al., *Hysteresis-less inverted CH 3 NH 3 PbI 3 planar perovskite hybrid solar cells with 18.1% power conversion efficiency.* Energy & Environmental Science, 2015. **8**(5): p. 1602-1608.
71. Zheng, Y.-Z., et al., *Iodine-doped ZnO nanopillar arrays for perovskite solar cells with high efficiency up to 18.24%*. Journal of Materials Chemistry A, 2017. **5**(24): p. 12416-12425.
72. Shuttle, C.G., et al., *Experimental determination of the rate law for charge carrier decay in a polythiophene: Fullerene solar cell.* Applied Physics Letters, 2008. **92**(9): p. 093311.
73. Sandberg, O.J., et al., *Theoretical perspective on transient photovoltage and charge extraction techniques.* The Journal of Physical Chemistry C, 2019. **123**(23): p. 14261-14271.
74. Chen, Y., et al., *Impacts of alkaline on the defects property and crystallization kinetics in perovskite solar cells.* Nature communications, 2019. **10**(1): p. 1-10.
75. Zhu, C., et al., *Strain engineering in perovskite solar cells and its impacts on carrier dynamics.* Nature communications, 2019. **10**(1): p. 815.
76. Shi, J., et al., *From Ultrafast to Ultraslow: Charge-Carrier Dynamics of Perovskite Solar Cells.* Joule, 2018. **2**(5): p. 879-901.
77. Singh, S., G. Banappanavar, and D. Kabra, *Correlation between Charge Transport Length Scales and Dielectric Relaxation Time Constant in Hybrid Halide Perovskite Semiconductors.* ACS Energy Letters, 2020: p. 728-735.
78. software, G. *Tip Convolution Artefacts*. [cited 2019; Available from: http://gwyddion.net/documentation/user-guide-en/tip-convolution-artefacts.html.
79. Villarrubia, J.S., *Algorithms for scanned probe microscope image simulation, surface reconstruction, and tip estimation.* Journal of research of the National Institute of Standards and Technology, 1997. **102**(4): p. 425.
80. Gan, Y., *Atomic and subnanometer resolution in ambient conditions by atomic force microscopy.* Surface Science Reports, 2009. **64**(3): p. 99-121.
81. Instruments, S. *Effect of the tip curvature radius and cone angle*. [cited 2019; Available from: https://www.ntmdt-si.com/resources/spm-theory/theoretical-background-of-spm/2-scanning-force-microscopy-(sfm)/25-ultimate-resolution-in-contact-mode/252-effect-of-the-tip-curvature-radius-and-cone-angle.
82. Wehrenfennig, C., et al., *High Charge Carrier Mobilities and Lifetimes in Organolead Trihalide Perovskites.* Advanced Materials (Deerfield Beach, Fla.), 2014. **26**(10): p. 1584-1589.

83. Stranks, S.D., et al., *Electron-Hole Diffusion Lengths Exceeding 1 Micrometer in an Organometal Trihalide Perovskite Absorber.* Science, 2013. **342**(6156): p. 341.
84. Sadewasser, S., et al., *Kelvin probe force microscopy for the nano scale characterization of chalcopyrite solar cell materials and devices.* Thin Solid Films, 2003. **431**: p. 257-261.
85. Kronik, L. and Y. Shapira, *Surface photovoltage phenomena: theory, experiment, and applications.* Surface Science Reports, 1999. **37**(1): p. 1-206.
86. Seto, J.Y., *The electrical properties of polycrystalline silicon films.* Journal of Applied Physics, 1975. **46**(12): p. 5247-5254.
87. Saliba, M., et al., *Cesium-containing triple cation perovskite solar cells: improved stability, reproducibility and high efficiency.* Energy & Environmental Science, 2016. **9**(6): p. 1989-1997.
88. Adhikari, N., *Nanoscale Study of Perovskite Solar Cells for Efficient Charge Transport.* 2016.
89. Kang, Z., et al., *Kelvin probe force microscopy for perovskite solar cells.* Science China Materials, 2019. **62**(6): p. 776-789.
90. Wu, F., et al., *Bias-Dependent Normal and Inverted J–V Hysteresis in Perovskite Solar Cells.* ACS applied materials & interfaces, 2018. **10**(30): p. 25604-25613.
91. Guo, Q., et al., *Passivation of the grain boundaries of CH 3 NH 3 PbI 3 using carbon quantum dots for highly efficient perovskite solar cells with excellent environmental stability.* Nanoscale, 2019. **11**(1): p. 115-124.
92. Dong, Q., et al., *Electron-hole diffusion lengths> 175 μm in solution-grown CH3NH3PbI3 single crystals.* Science, 2015. **347**(6225): p. 967-970.
93. Bahrami, B., et al., *Nanoscale control of grain boundary potential barrier, dopant density and filled trap state density for higher efficiency perovskite solar cells.* InfoMat. **n/a**(n/a).
94. Bu, T., et al., *A novel quadruple-cation absorber for universal hysteresis elimination for high efficiency and stable perovskite solar cells.* Energy & Environmental Science, 2017. **10**(12): p. 2509-2515.
95. Landi, G., et al., *Correlation between electronic defect states distribution and device performance of perovskite solar cells.* Advanced Science, 2017. **4**(10): p. 1700183.
96. Shi, D., et al., *Low trap-state density and long carrier diffusion in organolead trihalide perovskite single crystals.* Science, 2015. **347**(6221): p. 519.
97. Hutter, E.M., et al., *Charge Carriers in Planar and Meso-Structured Organic–Inorganic Perovskites: Mobilities, Lifetimes, and Concentrations of Trap States.* The Journal of Physical Chemistry Letters, 2015. **6**(15): p. 3082-3090.
98. Lu, C., et al., *From Macroscopic to Nanoscopic Current Hysteresis Suppressed by Fullerene in Perovskite Solar Cells.* Solar RRL, 2019. **3**(10): p. 1900235.
99. Luchkin, S.Y., et al., *Spatially-resolved nanoscale measurements of grain boundary enhanced photocurrent in inorganic CsPbBr3 perovskite films.* Solar Energy Materials and Solar Cells, 2017. **171**: p. 205-212.
100. Sadewasser, S., *Surface potential of chalcopyrite films measured by KPFM.* physica status solidi (a), 2006. **203**(11): p. 2571-2580.

101. Beerbom, M., et al., *Direct comparison of photoemission spectroscopy and in situ Kelvin probe work function measurements on indium tin oxide films.* Journal of electron spectroscopy and related phenomena, 2006. **152**(1-2): p. 12-17.
102. Chang, J., et al., *Enhancing the planar heterojunction perovskite solar cell performance through tuning the precursor ratio.* Journal of Materials Chemistry A, 2016. **4**(20): p. 7943-7949.
103. Ono, L.K. and Y. Qi, *Surface and Interface Aspects of Organometal Halide Perovskite Materials and Solar Cells.* The Journal of Physical Chemistry Letters, 2016. **7**(22): p. 4764-4794.
104. Zhang, M., et al., *Reconfiguration of interfacial energy band structure for high-performance inverted structure perovskite solar cells.* Nature communications, 2019. **10**(1): p. 1-9.
105. Zheng, X., et al., *Defect passivation in hybrid perovskite solar cells using quaternary ammonium halide anions and cations.* Nature Energy, 2017. **2**(7): p. 1-9.
106. Li, C., et al., *Unravelling the role of vacancies in lead halide perovskite through electrical switching of photoluminescence.* Nature Communications, 2018. **9**(1): p. 5113.
107. Xi, J., et al., *Chemical sintering reduced grain boundary defects for stable planar perovskite solar cells.* Nano Energy, 2019. **56**: p. 741-750.
108. Shan, W. and W.A. Saidi, *Segregation of Native Defects to the Grain Boundaries in Methylammonium Lead Iodide Perovskite.* The Journal of Physical Chemistry Letters, 2017. **8**(23): p. 5935-5942.
109. Wen, X., et al., *Interfacial engineering with amino-functionalized graphene for efficient perovskite solar cells.* Journal of Materials Chemistry A, 2016. **4**(35): p. 13482-13487.
110. Kerner, R.A., et al., *Amine additive reactions induced by the soft Lewis acidity of Pb2+ in halide perovskites. Part I: evidence for Pb–alkylamide formation.* Journal of Materials Chemistry C, 2019. **7**(18): p. 5251-5259.
111. Liu, G., et al., *Dependence of power conversion properties of perovskite solar cells on operating temperature.* Applied Physics Letters, 2018. **113**(11): p. 113501.
112. Yan, J., et al., *Accelerated hole-extraction in carbon-electrode based planar perovskite solar cells by moisture-assisted post-annealing.* Applied Physics Letters, 2019. **114**(10): p. 103503.
113. Chen, H., et al., *Dependence of power conversion properties of hole-conductor-free mesoscopic perovskite solar cells on the loading of perovskite crystallites.* Organic Electronics, 2018. **61**: p. 119-124.
114. deQuilettes, D.W., et al., *Photoluminescence Lifetimes Exceeding 8 μs and Quantum Yields Exceeding 30% in Hybrid Perovskite Thin Films by Ligand Passivation.* ACS Energy Letters, 2016. **1**(2): p. 438-444.
115. Adhyaksa, G.W., et al., *Carrier diffusion lengths in hybrid perovskites: processing, composition, aging, and surface passivation effects.* Chemistry of Materials, 2016. **28**(15): p. 5259-5263.
116. Levine, I., et al., *Mobility–Lifetime Products in MAPbI3 Films.* The Journal of Physical Chemistry Letters, 2016. **7**(24): p. 5219-5226.

117. Hsu, H.-Y., et al., *Optimization of PbI2/MAPbI3 Perovskite Composites by Scanning Electrochemical Microscopy.* The Journal of Physical Chemistry C, 2016. **120**(35): p. 19890-19895.
118. Xing, G., et al., *Long-Range Balanced Electron- and Hole-Transport Lengths in Organic-Inorganic CH<sub>3</sub>NH<sub>3</sub>PbI<sub>3</sub>*. Science, 2013. **342**(6156): p. 344-347.
119. Xie, F.X., et al., *Vacuum-Assisted Thermal Annealing of CH3NH3PbI3 for Highly Stable and Efficient Perovskite Solar Cells.* ACS Nano, 2015. **9**(1): p. 639-646.
120. Webber, D., et al., *Carrier diffusion in thin-film CH3NH3PbI3 perovskite measured using four-wave mixing.* Applied Physics Letters, 2017. **111**(12): p. 121905.
121. Li, Y., et al., *Direct Observation of Long Electron-Hole Diffusion Distance in CH3NH3PbI3 Perovskite Thin Film.* Scientific Reports, 2015. **5**: p. 14485.
122. Nicoara, N., et al., *Direct evidence for grain boundary passivation in Cu(In,Ga)Se2 solar cells through alkali-fluoride post-deposition treatments.* Nature Communications, 2019. **10**(1): p. 3980.
123. Kim, W., et al., *Enhanced long-term stability of perovskite solar cells by passivating grain boundary with polydimethylsiloxane (PDMS).* Journal of Materials Chemistry A, 2019. **7**(36): p. 20832-20839.
124. Liu, Y., et al., *Study on hole-transport-material-free planar TiO2/CH3NH3PbI3 heterojunction solar cells: the simplest configuration of a working perovskite solar cell.* Journal of Materials Chemistry A, 2015. **3**(28): p. 14902-14909.
125. Li, J., et al., *Direct Evidence of Ion Diffusion for the Silver-Electrode-Induced Thermal Degradation of Inverted Perovskite Solar Cells.* Advanced Energy Materials, 2017. **7**(14): p. 1602922.
126. Kim, A., et al., *Fully solution-processed transparent electrodes based on silver nanowire composites for perovskite solar cells.* Nanoscale, 2016. **8**(12): p. 6308-6316.
127. Huang, L., et al., *Synergistic Interface Energy Band Alignment Optimization and Defect Passivation toward Efficient and Simple-Structured Perovskite Solar Cell.* Advanced Science, 2020. **7**(6): p. 1902656.
128. Liu, Y., et al., *Perovskite Solar Cells Employing Dopant-Free Organic Hole Transport Materials with Tunable Energy Levels.* Advanced Materials, 2016. **28**(3): p. 440-446.
129. Nouri, E., M.R. Mohammadi, and P. Lianos, *Improving the stability of inverted perovskite solar cells under ambient conditions with graphene-based inorganic charge transporting layers.* Carbon, 2018. **126**: p. 208-214.
130. Zimmermann, E., et al., *Erroneous efficiency reports harm organic solar cell research.* Nature Photonics, 2014. **8**(9): p. 669-672.
131. Al-Dainy, G.A., et al., *Optimizing Lignosulfonic Acid-Grafted Polyaniline as a Hole-Transport Layer for Inverted CH3NH3PbI3 Perovskite Solar Cells.* ACS omega, 2020. **5**(4): p. 1887-1901.